GEORGIA DOT RESEARCH PROJECT 19-04

Final Report

PHASE II - INVESTIGATION AND GUIDELINES FOR BEST PRACTICES OF MASS CONCRETE CONSTRUCTION MANAGEMENT

Georgia Department of Transportation

Office of Performance-based Management and Research
600 West Peachtree Street NW | Atlanta, GA 30308

April 2022

TECHNICAL REPORT DOCUMENTATION PAGE

1. Report No.: FHWA-GA-22-1904	2. Government Accession No.: N/A	3. Recipient's Catalog No.: N/A
4. Title and Subtitle: Phase II - Investigation and Guidelines for Best Practices of Mass Concrete Construction Management		5. Report Date: July 2022 6. Performing Organization Code: N/A
7. Author(s): Yong Kwon Cho (PI), Ph.D. Russell Gentry (coPI), Ph.D. Kimberly Kurtis (coPI), Ph.D. Jason Brown, Ph.D. Jisoo Park, Ph.D. Luna Al Hasani		8. Performing Organ. Report No.: 19-04
9. Performing Organization Name and Address: Georgia Institute of Technology 225 North Ave NW Atlanta, GA 30332 Phone: (404) 385-2038 Email: yong.cho@ce.gatech.edu		10. Work Unit No.: N/A 11. Contract or Grant No.: PI# 0016832
12. Sponsoring Agency Name and Address: Georgia Department of Transportation (SPR) Office of Performance-based Management and Research 600 West Peachtree Street NW St. Atlanta, GA, 30308		13. Type of Report and Period Covered: Final; July 2019 – July 2022 14. Sponsoring Agency Code: N/A
15. Supplementary Notes: Prepared in cooperation with the U.S. Department of Transportation, Federal Highway Administration.		

16. Abstract:

The objective of this research is to improve and validate the mass concrete thermal management methods (e.g., passive or active cooling) and decision-making tools developed from the Phase I research (Investigation and Guidelines for Mass Concrete Construction Management) against the Georgia Department of Transportation's (GDOT's) real-world mass concrete construction projects. A case study was conducted on the actual bridge construction site to identify the thermal behavior of mass concrete structure. The team developed a simplified nomogram to support the appropriate thermal control plan selection, as well as investigated the real-world cost implication of thermal management methods. Through the Phase II research, the research findings are: 1) active cooling is three times more expensive than passive cooling, but passive cooling requires a very long curing time, 2) when paired with an uncertainty assessment, nomograms can provide useful estimates of maximum temperatures in hydrating mass concrete with or without postcooling, 3) using alternative cementitious systems than OPC (fly ash, coarser cement) leads to satisfying temperature limits without using stringent thermal control plans, 4) statistical methods can be successfully used as an alternative modeling approach to optimize mixture design selection, and 5) the cost nomogram can simply estimate the total cost for pre-cooling and post- cooling methods roughly. These efforts led to development of practical tools for the specification of standardized thermal management methods.

17. Key Words: Mass Concrete, Construction, Thermal Control, Nomograph, Cost Analysis		18. Distribution Statement: No restrictions.	
19. Security Classification (of this report): Unclassified	20. Security Classification (of this page): Unclassified	21. No. of Pages: 155	22. Price: Free

Form DOT F 1700.7(8-72) Reproduction of completed page authorized.

GDOT Research Project 19-04

Final Report

PHASE II - INVESTIGATION AND GUIDELINES FOR BEST PRACTICES OF MASS CONCRETE CONSTRUCTION MANAGEMENT

By
Yong Kwon Cho, Ph.D.
Professor, School of Civil and Environmental Engineering

Russell Gentry, Ph.D.
Associate Professor, School of Architecture

Kimberly Kurtis, Ph.D.
Professor, School of Civil and Environmental Engineering

Jason Brown, Ph.D.
Senior Personnel, Raven Research

Jisoo Park, Ph.D.
Postdoctoral Fellow, School of Civil and Environmental Engineering

Luna Al Hasani
Graduate Research Assistant, School of Civil and Environmental Engineering

Georgia Tech Research
Corporation

Contract with
Georgia Department of Transportation

In cooperation with
U.S. Department of Transportation
Federal Highway Administration

June 2022

SI* (MODERN METRIC) CONVERSION FACTORS

APPROXIMATE CONVERSIONS TO SI UNITS

Symbol	When You Know	Multiply By	To Find	Symbol
		LENGTH		
in	inches	25.4	millimeters	mm
ft	feet	0.305	meters	m
yd	yards	0.914	meters	m
mi	miles	1.61	kilometers	km
		AREA		
in^2	square inches	645.2	square millimeters	mm^2
ft^2	square feet	0.093	square meters	m^2
yd^2	square yard	0.836	square meters	m^2
ac	acres	0.405	hectares	ha
mi^2	square miles	2.59	square kilometers	km^2
		VOLUME		
fl oz	fluid ounces	29.57	milliliters	mL
gal	gallons	3.785	liters	L
ft^3	cubic feet	0.028	cubic meters	m^3
yd^3	cubic yards	0.765	cubic meters	m^3
	NOTE: volumes greater than 1000 L shall be shown in m^3			
		MASS		
oz	ounces	28.35	grams	g
lb	pounds	0.454	kilograms	kg
T	short tons (2000 lb)	0.907	megagrams (or "metric ton")	Mg (or "t")
		TEMPERATURE (exact degrees)		
°F	Fahrenheit	5 (F-32)/9 or (F-32)/1.8	Celsius	°C
		ILLUMINATIO N		
fc				lx
fl	foot-candles	10.76	lux	cd/m^2
	foot-Lamberts	3.426	candela/m^2	
		FORCE and PRESSURE or STRESS		
lbf	poundforce	4.45	newtons	N
lbf/in^2	poundforce per square inch	6.89	kilopascals	kPa

APPROXIMATE CONVERSIONS FROM SI UNITS

Symbol	When You Know	Multiply By	To Find	Symbol
		LENGTH		
mm	millimeters	0.039	inches	in
m	meters	3.28	feet	ft
m	meters	1.09	yards	yd
km	kilometers	0.621	miles	mi
		AREA		
mm^2	square millimeters	0.0016	square inches	in^2
m^2	square meters	10.764	square feet	ft^2
m^2	square meters	1.195	square yards	yd^2
ha	hectares	2.47	acres	ac
km^2	square kilometers	0.386	square miles	mi^2
		VOLUME		
mL	milliliters	0.034	fluid ounces	fl oz
L	liters	0.264	gallons	gal
m^3	cubic meters	35.314	cubic feet	ft^3
m^3	cubic meters	1.307	cubic yards	yd^3
		MASS		
g	grams	0.035	ounces	oz
kg	kilograms	2.202	pounds	lb
Mg (or "t")	megagrams (or "metric ton")	1.103	short tons (2000 lb)	T
		TEMPERATURE (exact degrees)		
°C	Celsius	1.8C+32	Fahrenheit	°F
		ILLUMINATIO N		
lx				fc
cd/m^2	lux	0.0929	foot-candles	fl
	candela/m^2	0.2919	foot-Lamberts	
		FORCE and PRESSURE or STRESS		
N	newtons	0.225	poundforce	lbf
kPa	kilopascals	0.145	poundforce per square inch	lbf/in^2

* SI is the symbol for the International System of Units. Appropriate rounding should be made to comply with Section 4 of ASTM E380. (Revised March 2003)

TABLE OF CONTENTS

LIST OF FIGURES

LIST OF TABLES

EXECUTIVE SUMMARY

The objective of this research is to improve and validate the mass concrete thermal management methods (e.g., passive or active cooling) and decision-making tools developed from the Phase I research, titled as Investigation and Guidelines for Mass Concrete Construction Management, against GDOT's real-world mass concrete construction projects. The findings from this research will be translated into practical tools that permit the rapid, standardized, and robust specification of thermal management methods for typical mass concrete installations in Georgia. In addition, the real-world cost implication of thermal management methods was investigated as well. The specific scope of the work completed within this research project includes:

- **Task 1. Implementation of sensors and a remote network system through case studies:** In Task 1, the research team conducted a real-world case study to identify the thermal behavior of the non-mass concrete structure and the mass concrete structure at Norfolk Southern Railway Project over State Route 92 (SR 92) in Douglas County, Georgia. The research team installed the temperature and concrete strain sensors to the structures to measure maximum temperature and differential temperature during concrete placement and initial curing for bridge foundation and abutment. The temperature data collected from the case study were used as a reference for the temperature nomogram development and validation. In addition, the research team obtained cost information for the thermal control methods, and the cost data were used to generate the cost nomogram.

- **Task 2. Development of thermal management methods:** In Task 2, the research team developed simple temperature-prediction tools using nomograms to improve and support appropriate thermal control method selection. A series of nomograms to aid in planning mass concrete projects have been developed based on first principles and on a suite of simulations. The major objective of these nomograms is to help users identify and eliminate doubtful parameter space and aid in rapidly finding candidate thermal management plans to be verified with more detailed—but fewer—analyses.

- **Task 3. Mass concrete mix designs:** In Task 3, isothermal calorimetry tests were conducted at different temperatures to obtain the rate of heat release of cement. Isothermal calorimetry can be used to find the adiabatic temperature rise and corresponding rate of heat release for concrete with any material characteristics and initial placement temperatures. The methodology intrinsically considers the chemical and physical characteristics of the mix design, necessarily considers the effect of placement and curing temperatures on the rate of heat release and does not require information on the thermal properties of the calorimeter. The proposed methodology was validated through two mid-scale concrete experiments previously performed in Phase 1 research, and findings demonstrate that it was successful in predicting internal temperatures for both the uncooled and actively cooled mid-scale experiments.

- **Task 4. Development of alternative modeling approaches:** In Task 4, the research team proposed an alternative modeling approach for the heat of hydration of mass concrete structures using machine learning. The Gaussian process

regression model was used to predict the heat of hydration histories up to 72 hours at different isothermal temperatures. The ability of the GPR model to predict thermal behavior with reasonable accuracy was validated with 92 percent of the average R2. The model was then used to predict the heat of hydration curves for a cement belonging to two mid-scale mass concrete experiments. The ability to use the predictions of the machine learning model and upscale them for application in real-life engineering and decision-making systems has been proven. The model can be expanded to include more features related to other types of supplementary cementitious materials and possibly admixtures.

- **Task 5. Economic analysis of cooling methods:** In Task 5, the research team conducted a comprehensive economic analysis of thermal control methods based on the cost information collected from a case study and literature review. A cost nomogram was developed to estimate the cost for thermal control methods, including precooling and postcooling methods. The cost nomograms simply generated the total cost to cool the concrete with several methods. The economic analyses of the cooling methods were performed based on real-world case studies, and the results were compared to alternative designs and thermal management methods. Although the cost nomogram may not estimate the exact cost because it varies depending on the location and manufacturer, we expect the cost nomogram can be used for resources to select a cost-effective thermal control plan.

- **Task 6. Development of the best practice guideline and tool:** In Task 6, the research team included and integrated outcomes from Tasks 1 to 5 to provide the best practices or tools for: (1) mix design selection, and (2) active thermal control

plan selection. The best practices and tools for mix-design selection were developed with isothermal calorimetry demonstrated in Task 3. The ways of using nomograms with thermal parameters are described. The research team also presented ways of managing mass concrete construction with nomograms in this task.

In summary, the research team presented a simple decision-making guideline for thermal control methods using nomograms in mass concrete construction. The nomograms include temperature nomograms and cost nomograms for both precooling and postcooling scenarios. The temperature nomograms were created based on isothermal calorimetry tests and regression models using numerous simulation data, and the cost nomograms used closed-form equations to calculate the total cost. To validate the proposed methods, this study conducted a case study with an actual bridge construction project.

Although the developed decision-making guideline can provide cost-effective alternatives for mass concrete thermal control in given conditions, several limitations are also found in the proposed nomograms. First, the temperature nomograms developed in this study work well under ordinary Portland cement concrete. Since the hydration heat differs depending on the amount of cementitious material, the temperature prediction model must be modified if the SCM is added. Furthermore, the current version of nomograms cannot predict the temperature difference, which is also a significant factor to be managed in mass concrete construction. Therefore, in a future study, we will develop an extended nomogram that can calculate both maximum temperature and temperature difference, and consider different mix designs.

CHAPTER 1. INTRODUCTION

American Concrete Institute (ACI) defines mass concrete as any volume of concrete placements with sufficient mass. The heat evolved from the curing concrete can lead to undesirable thermal stresses, cracking, deleterious chemical reactions, or reduction in the long-term strength. [1] If mass concrete overheats due to the exotherm, the concrete may self-destruct due to delayed ettringite formation (DEF) in the worst case or may experience early-age cracking due to thermal differentials; this is not a fatal problem, but such cracking could lead to long-term durability problems.[2] Thus, an inappropriate choice of cooling methods utilized by contractors would decrease the quality of the concrete or structure, which could prove costly for owners who must maintain the resulting defects. A practical guideline for cost-effective thermal control method selection is needed to avoid wrong choices that can cause rising costs and degradation of quality.

The current Georgia Department of Transportation (GDOT) specification requires contractors to develop and implement thermal management techniques (e.g., active cooling during curing, precooling prior to placement, etc.) to mitigate risks arising from high temperatures and thermal gradients in mass concrete. The custom nature of these measures leads to a risk of added expenses arising from developing and enacting cooling measures anew on each project. Standardized, validated cooling systems are seen as a way to mitigate this cost risk as the engineering expenses are spread over many projects. To mitigate such risks, specifications regarding mass concrete are being re-evaluated nationally, with some updates and changes in practice occurring in recent years. For example, the California Transportation Division of Research and Innovation investigated the effects of the heat of

hydration of mass concrete for cast-in-place piles.[3] Florida DOT regulates using a concrete mixture for mass concrete application with slag or fly ash, which allows a maximum internal temperature of 180°F.[4] Other states are also actively reviewing and updating their specifications and guidance.

The current research team has developed thermal management methods and decision-making tools for mass concrete construction from Phase I of this research project. During Phase I, we developed various thermal models of concrete during hydration and active cooling. These models show that metal pipes cool much more than plastic ones, but they may cause higher thermal stress due to larger internal thermal gradients. Also, the increasing pipe diameter is found to be more effective than increasing cooling water flow. Model outputs compared reasonably well to mid-scale experiments (4 ft × 4 ft × 6 ft specimens) with and without active cooling. However, these tests and analyses were conducted under controlled laboratory environments and simulated situations. Additionally, existing models of concrete hydration were found to require improvements; they are complex, require knowledge of many parameters, and result in predictions that can be nonconservative. Thus, it is necessary to validate and improve the research findings through real-world case studies. Ultimately, these models, their output, and experimental data need to be translated into practical tools that permit the rapid, standardized, and robust specification of thermal management methods for typical mass concrete installations in Georgia.

To this end, the research team conducted the second phase of research for mass concrete thermal control with the following individual tasks:

- Task 1. Implementation of sensors and a remote network system through case studies.
- Task 2. Development of thermal management methods.
- Task 3. Mass concrete mix designs.
- Task 4. Development of alternative modeling approaches.
- Task 5. Economic analysis of cooling methods.
- Task 6. Development of the best practice guideline and tool.

Through these research processes, the research team presents best practice guidelines and tools to select appropriate thermal control plans for mass concrete construction projects. The research findings and temperature prediction models are tested and validated through real-world case studies.

CHAPTER 2. IMPLEMENTATION OF SENSORS AND A REMOTE NETWORK SYSTEM THROUGH CASE STUDIES (TASK 1)

INTRODUCTION

In Task 1, the research team implemented a sensing system to identify actual thermal properties and behavior through case studies at Norfolk Southern Railway Project over State Route 92 (SR-92) in Douglas County, Georgia (see Figure 1). The research team installed the temperature and concrete strain sensors to the structures to measure maximum temperature and differential temperature during concrete placement and initial curing for two types of structures: (1) bridge foundation, and (2) abutment. As shown in figure 2, the depth of the abutment is greater than 5 ft, which was designed as *mass concrete*, and the depth of the foundation is less than 5 ft, which was considered a *general concrete* structure under GDOT Special Provision, Section 500, Concrete Structures. The observed heat of hydration curves was compared with those predicted from the developed thermal prediction model (e.g., temperature nomograms). Semi-adiabatic tests were conducted to obtain the thermal behavior of the concrete mixture used in the SR-92 bridge construction project.

Figure 1. Photos. SR-92 Norfolk Southern Railway bridge construction project.

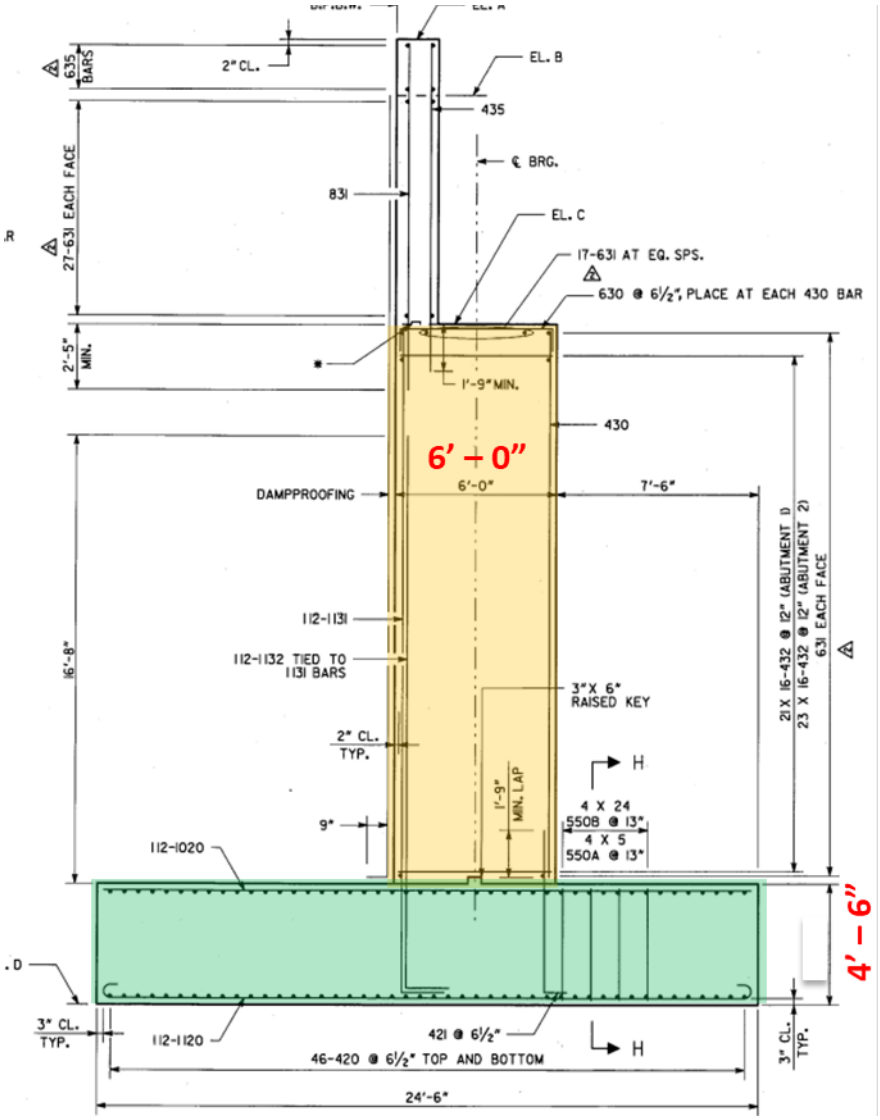

Figure 2. Illustration. Cross-section view of abutment and foundation of SR-92 bridge.

FOUNDATION

As aforementioned, the foundation was designed as a general concrete structure because the depth is 4.5 ft, which is less than the 5 ft to be considered mass concrete. For this reason, the postcooling system was not applied to the foundation. The dimensions of the concrete foundation were 24.5 ft wide, 37 ft long, and 4.5 ft in depth. Class AA concrete was used for the foundation, and it was insulated by ¾-inch plywood formwork for 4 days. An

insulation blanket was not employed for the foundation. The concrete placement was conducted on August 3, 2021, and the ambient temperature was 80°F. The detailed field conditions are demonstrated in Table 1 and photos of the foundation preparation are provided in Figure 3.

Table 1. The conditions of the concrete placement of the foundation.

Initial Conditions		**Cooling System**	
Placing temperature Ambient temperature	69.3°F 81°F	N/A	
Material		**Shields**	
Cement	670 lb/yd^3	Plywood thickness	¾ in.
SCMs[1]	N/A	Blanket thickness	N/A
w/c ratio	0.461	Time of removal	During day 4

[1] Supplementary cementitious materials.

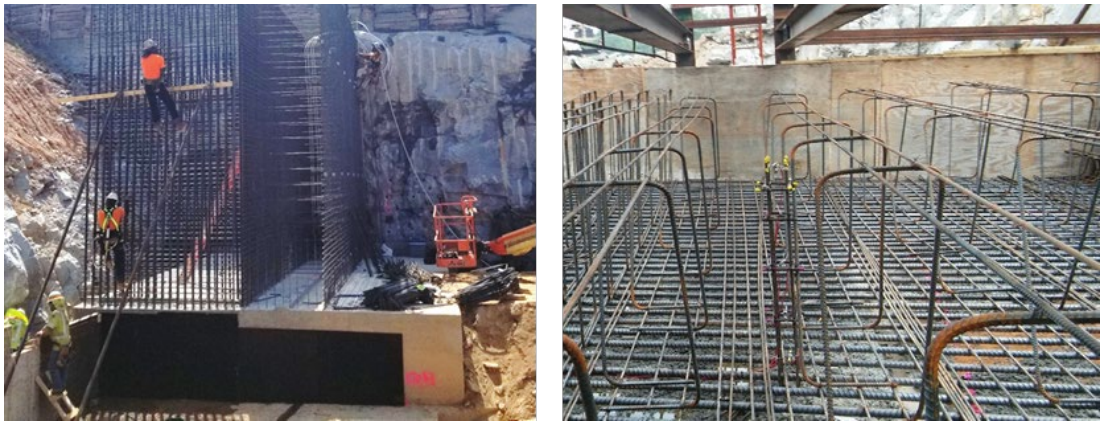

Figure 3. Photos. Concrete foundation of the SR-92 bridge.

Temperature Monitoring for Concrete Foundation

To measure the hydration temperature of the foundation, we installed two thermometers and three strain gauges in two locations, as shown in Figure 4. Sensors were vertically placed at five locations at the same interval from 8 inches away from the surface, as shown in Figure 5. The data were collected for 56 days from the date of the concrete placement.

Since the concrete foundation of the SR-92 bridge is not classified as a mass concrete structure (i.e., less than 5 ft), no thermal control method was applied to the structure.

A. Locations of the sensor frames.

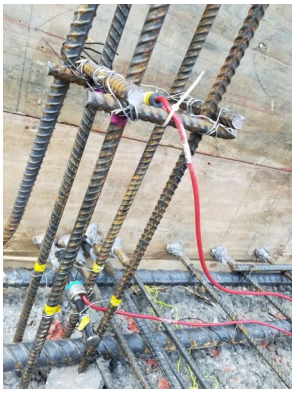

B. Sensor frame installed at the side.

C. Sensor frame installed at the center.

Figure 4. Photos. Sensor installation at the SR-92 concrete foundation.

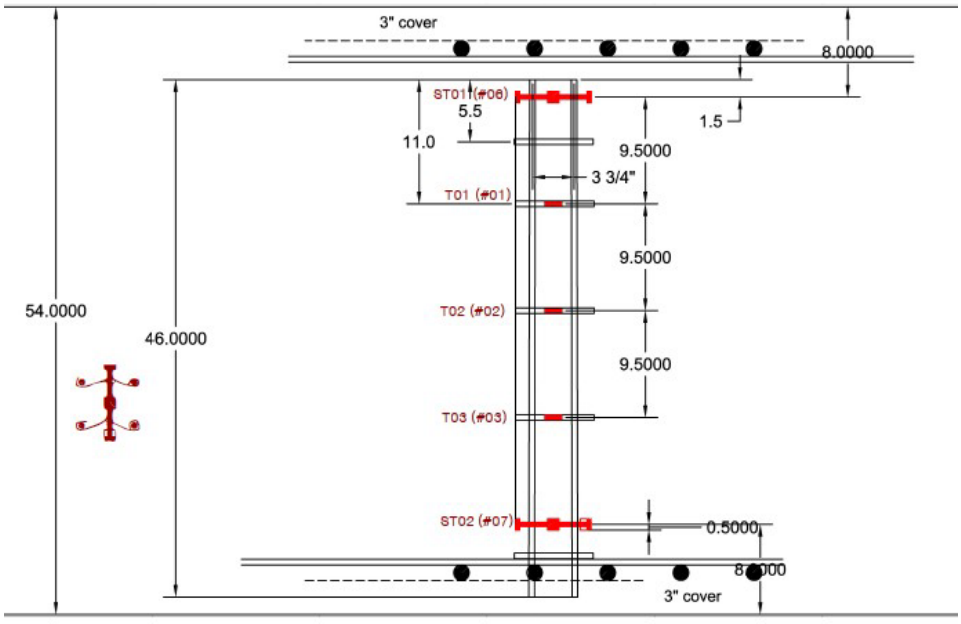

Figure 5. Illustration. Schematic of the SR-92 sensor frame.

Figure 6 shows the temperature during the measuring period. The observed highest temperature was 152°F (66.8°C) at the bottom of the foundation's center, which was lower

than the maximum temperature limit (158°C) specified by GDOT. The measured maximum temperature difference was about 20°F, which is also within the tolerance of 35°F.

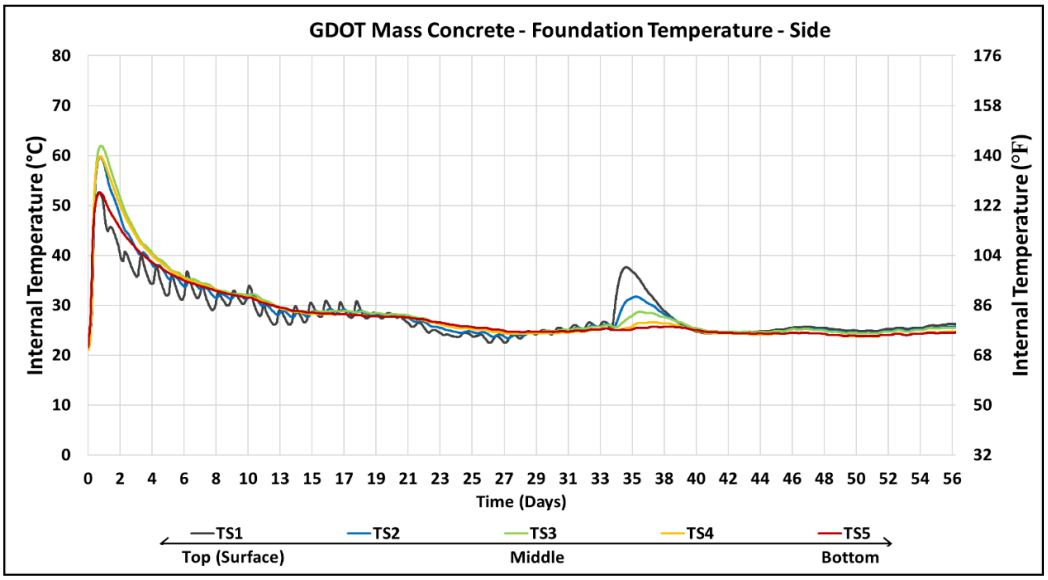

A. Hydration temperature at the side of the foundation.

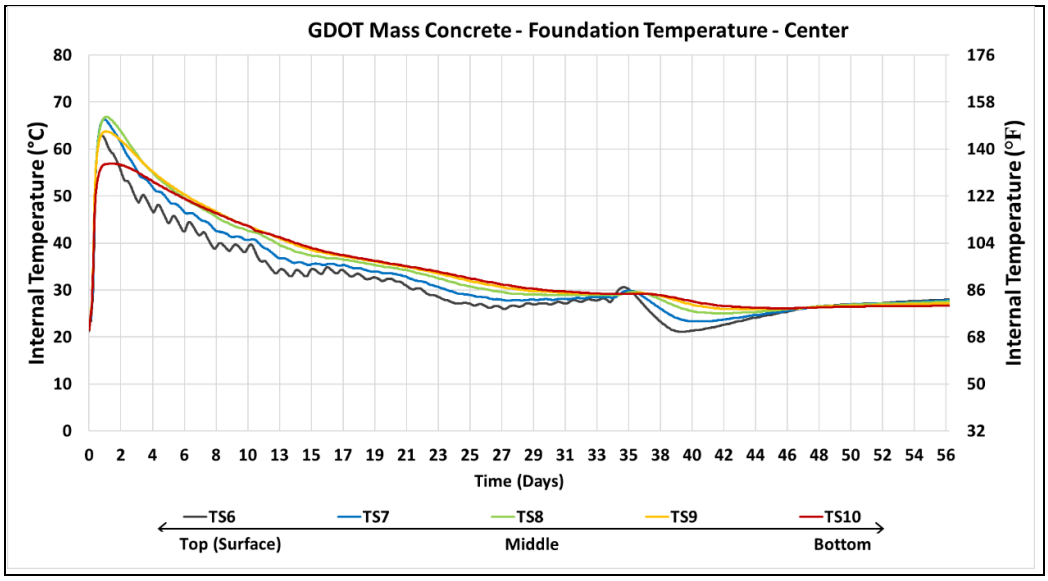

B. Hydration temperature at the center of the foundation.

Figure 6. Graphs. Time-series hydration temperature at the SR-92 foundation.

ABUTMENT

The abutment of the SR-92 bridge was designed as mass concrete because all its dimensions are greater than 5 ft. The dimensions of the concrete abutment were 6 ft thick, 20.5 ft high, and 37 ft long. Type I/II Portland cement was used in this placement. The concrete pouring for the abutment took place on September 6, 2021. Table 2 shows the details of the conditions of the concrete placement and thermal control plans. The contractors employed active thermal control plans, including precooling and pipe postcooling methods. The cooling system was turned on just a few minutes before the start of the concrete placement and ran until the difference between internal temperature and ambient temperature was within 35°F. Liquid nitrogen (LN) and ice were used for precooling to lower the placement temperature to 70°F. The formwork was made up of an external steel frame with ¾-inch plywood, and insulation blankets were installed on the outside of the formwork. The insulation blanket was attached to the forms using heavy-duty magnets, and the exposed top was covered with sand and blankets. Figure 7 shows the equipment and material for the chilled-water cooling system implemented. Figure 8 depicts the cooling system applied to the abutment of the SR-92 bridge. The tubing was spaced 1–2 ft, as shown in Figure 9, and the diameter was ¾ inch.

Table 2. The conditions of the concrete placement of the abutment.

Initial Conditions		**Cooling System**	
Placing temperature	69.3°F	Pipe spacing	1×2 ft
Ambient temperature	81°F	Water temperature	45°F
		PEX tube diameter	¾ in.
Material		**Shields**	
Cement	670 lb/yd^3	Plywood thickness	¾ in.
SCMs	N/A	Blanket thickness	N/A
w/c ratio	0.461	Time of removal	During day 4

A. Fabricated manifolds. B. Installed PEX tubes. C. Chiller and water tank.

Figure 7. Photos. Post cooling system used in the SR-92 concrete abutment.

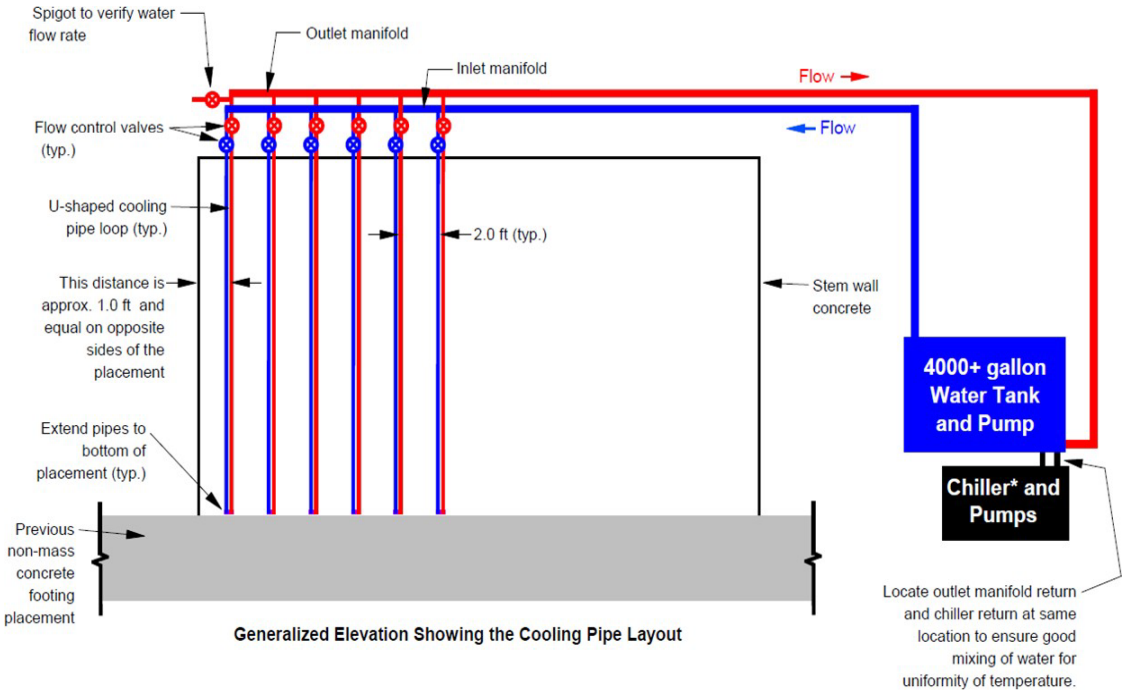

Figure 8. Illustration. SR-92 cooling system layout.

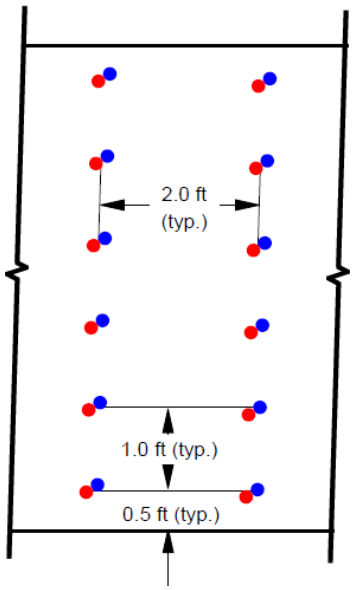

Figure 9. Illustration. SR-92 cooling pipe layout.

Temperature Monitoring for Concrete Abutment

A total of twelve strain gauges and three thermometers were installed at three different locations, as shown in Figure 10. The sensors were horizontally placed at five locations at the same interval 8 inches away from the surface.

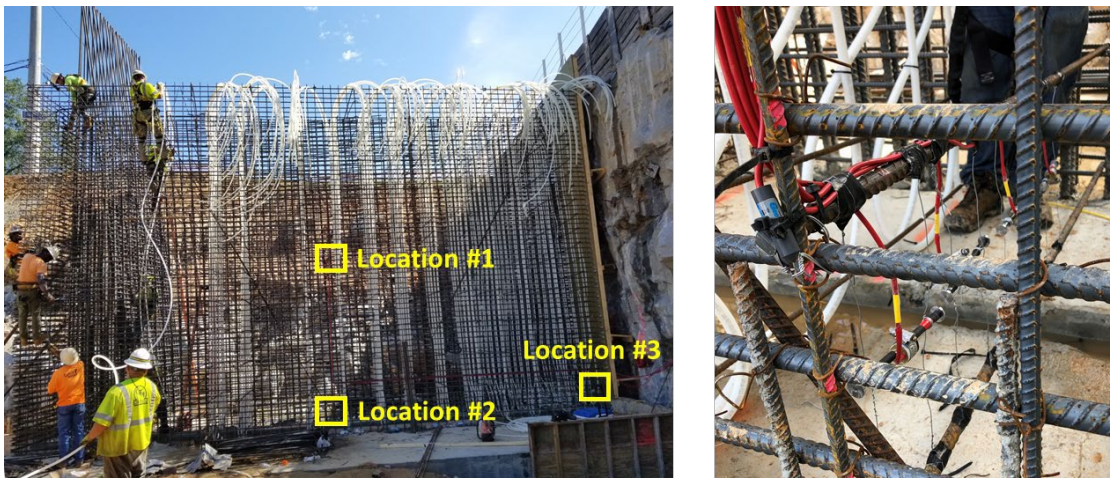

Figure 10. Photos. Sensor locations at the SR-92 abutment.

Figure 11 shows the hydration temperature at the abutment during the measuring period. The observed highest temperature was 133.7°F (56.5°C) at the bottom of the abutment side, which was lower than the maximum temperature limit (158°C) specified by GDOT. The measured maximum temperature difference was about 18°F, which is also within the tolerance of 35°F.

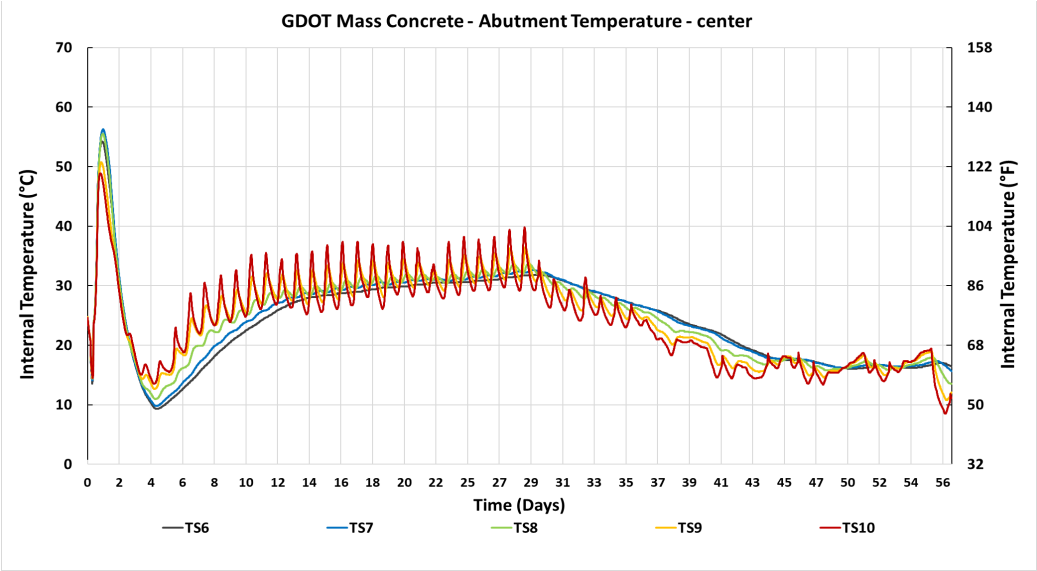

A. Location 1

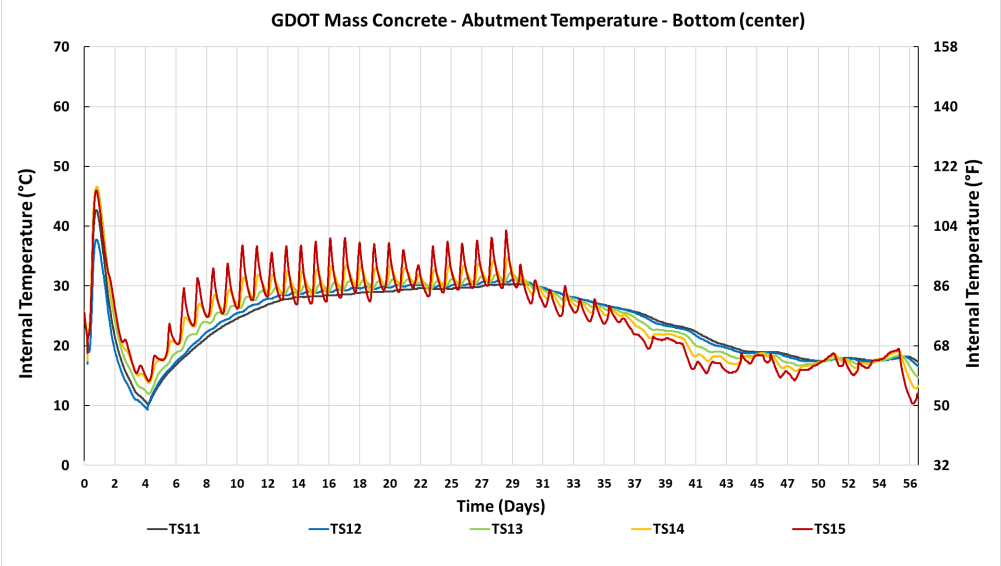

B. Location 2

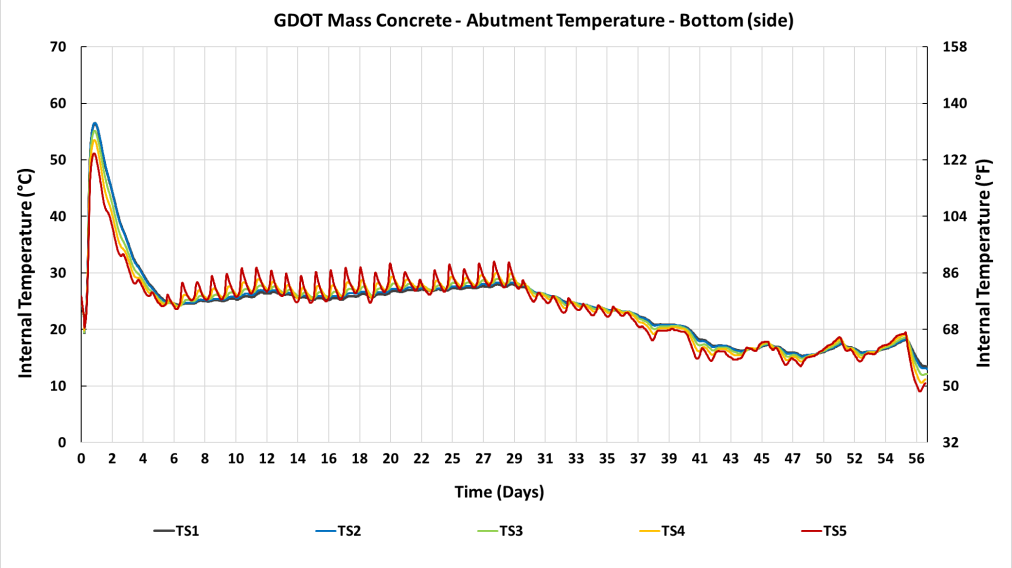

C. Location 3

Figure 11. Graphs. Time-series hydration temperature at the SR-92 abutment.

CONCLUSION

Through a real-world case study, the hydration temperature data of a nonmass concrete structure (24.5 ft × 37 ft × 4.5 ft foundation) and a mass concrete structure (6 ft × 20.5 ft × 37 ft abutment) were collected from on-site sensing systems. Since the abutment was designed as a mass concrete structure, precooling methods using LN and ice and postcooling methods using pipe-cooling were implemented. As a result, the observed highest temperatures were 152°F (66.8°C) at the foundation and 133.7°F (56.5°C) at the abutment; both temperatures were lower than the maximum temperature limit of 70°C (158°C) specified by GDOT. The temperature data collected from the case study were used as a reference for the temperature nomogram development and validation, as described in Chapter 3. In addition, the research team obtained cost information for the thermal control methods applied to the SR-92 bridge construction projects. The cost data were used to generate the cost nomogram described in Chapter 6.

CHAPTER 3. DEVELOPMENT OF THERMAL MANAGEMENT METHODS (TASK 2)

INTRODUCTION

The objective of this task is to improve and validate the mass concrete thermal management methods (e.g., passive or active cooling) and decision-making tools developed from the Phase I research in this project against GDOT's real-world mass concrete construction projects. Measures to mitigate temperatures in mass concrete include precooling, in which the concrete is cooled prior to emplacement, and postcooling, in which the concrete is actively cooled after emplacement by the circulation of fluid through pipes embedded in the concrete. Measures to mitigate thermal gradients can be directly addressed using insulation.[5] Both precooling and postcooling can indirectly mitigate thermal gradients, the former via lowering the rate of the hydration reaction, which allows time for heat transfer within the concrete to weaken temperature differences, and the latter via judicious placement of pipes and choice of piping material to lower overall temperatures in core regions.

The technique, or techniques, chosen to control temperatures in mass concrete can have significant project cost and schedule implications. The many parameters on thermal management decision-making—precooling and/or postcooling, how, and how much to precool, choice of postcooling pipe material, cooling water temperatures, pipe spacing, cost factors—leads to a large trade-off space. Traversing this space to find acceptable solutions can itself be time-consuming and repetitive. The purpose of this task is to produce tools, specifically nomograms, to expedite this process.

Nomograms are expedient, visual, purpose-built computers embodying closed-form mathematical equations. They have a long history in civil engineering, for example, as aids in the design and construction of the French railway network.[6,7,8] Nomograms are not as widespread today due to the availability of electronic computation, although they still find use in clinical medical settings as well as engineering.[9] Nomograms represent all solutions simultaneously and visually depict the nature of the relations between variables. In conjunction with the human visual system, this allows rapid initial trade-offs and exploration of the parameter space so that promising options, as well as unpromising options, can be identified. Furthermore, nomograms are resistant to obsolescence since they are not tied to a programming language or any particular computing technology.

The ACI *Report on Thermal and Volume Change Effects on Cracking of Mass Concrete* contains many charts that can be considered basic nomograms, as well as three sophisticated, bona fide nomograms depicting quantitative relationships between variables in postcooling.[10] The 13th edition of the Portland Cement Association's (PCA's) *Design and Control of Concrete Mixtures* also contains basic nomograms for a temperature of freshly mixed concrete and surface moisture evaporation rate, among others.[11] Silva and Smilauer presented a nomogram for the maximum temperature of concrete as a function of binder content, percentage of supplementary cementitious materials (SCMs), concrete thickness, and initial and ambient temperatures.[12] Their method was to run many one-dimensional finite element analysis (FEA) simulations and regress linear models on the resulting data, thereby creating a closed-form surrogate model of their simulations that can be represented in nomographic form. Nguyen et al. also use this surrogate model approach

to create a nomogram for maximum temperatures in cubes as a function of two variables: cement content and initial temperature.[13]

Here, we present a set of nomograms for the concrete temperature to aid in the development of mass concrete thermal management plans. The particular cases cover:

1. Temperature of fresh concrete given temperatures of cement, water, and aggregate, together with a worst-case scenario of concrete temperature during hydration assuming adiabatic conditions.
2. Maximum temperature of concrete without postcooling during hydration for nonadiabatic conditions, given initial temperature, size of the emplacement as parameterized by volume and surface area, and ambient conditions.
3. Maximum temperature of postcooled concrete during hydration, given initial temperature, cooling water temperature, and pipe size.

Case 1 aids in deciding if and how to precool. By providing a simple worst-case maximum temperature, this case also allows thermal management planning to cease with this nomogram if temperatures are below a critical threshold. While the nomograms in this first case are based directly on first principles, the second and third cases use numerical simulations and regression to derive closed-form surrogate models representable as nomograms. However, the simulations here are all three-dimensional (3D) and are not limited to cubes but are limited in this work to a particular concrete mix. These two cases also inform decisions about precooling in addition to aiding in the decision regarding whether or not to postcool; if the decision is made to postcool, the nomograms help choose pipe size, piping layout, and cooling water temperature. For the third case, each nomogram

is limited to pipes of one material (i.e., PEX) in addition to being limited to one concrete mix, although the method presented can easily be applied to other mixes and pipes.

Use of the nomograms presented here is not a substitute for in-depth analysis and detailed simulations of specific thermal management designs. The intent is for these nomograms to help users identify and eliminate unpromising areas of the parameter space and aid in rapidly finding candidate thermal management plans to be verified with more detailed—but fewer—analyses. The nomograms are general tools made under specific scenarios that statistically embody a range of cases. Thus, they have a measure of noise or error unavoidably written into them and should be used with this in mind.

METHODS AND RESULTS

General Considerations

Two concrete mixes were used in this work, as shown in Table 3.

Table 3. Characteristics of concrete mixes used.

	AA+ Baseline: Cases 1 and 2	SR-92 Concrete: Case 3
Cement, $\frac{kg}{m^3}$	413	397
All aggregate, $\frac{kg}{m^3}$	1,744	1,706
Water, $\frac{\frac{kg}{m^3}}{kg}$	202	183
ρc, $_{m}$__3	2,359	2,286
c_c, $\frac{J}{kgK}$	1,062	1,062
κ_c, $\frac{W}{mK}$	1.7	1.7

Where, ρ_c, c_c, and κ_c are the density, specific heat, and thermal conductivity of the concrete, respectively. The AA+ baseline mix is from Phase I of this project; the SR-92 concrete is

from the Norfolk Southern Railway Project over SR-92, Douglas County, Georgia, as discussed in Chapter 2. Both mixes are quite similar, and using a nomogram from case 1 or 2 for the SR-92 concrete, for example, is assumed to lead to negligible error. The reason for the two concretes is that isothermal calorimetry was conducted for the SR-92 cement, as described in Chapter 4, in order to improve modeling of the hydration reaction. All nomograms were made using the open-source Python package PyNomo.[14]

Case 1: Mixed Concrete Temperature and Worst-case Maximum Temperature

To prepare a nomogram for the temperature of freshly mixed concrete, $T_{fresh,c}$, we first make the following simplifying assumptions:

1. Cement and both fine and coarse aggregates have identical specific heats.
2. Coarse and fine aggregates are at the same temperature upon mixing.
3. Aggregates are dry upon mixing.
4. Ice is not used.

Assumptions 1 and 2 are related: the specific heat of sand is roughly 800 J/(kgK) and that of granite is around 775–820 J/(kgK); under similar storage conditions, their temperatures are taken to be similar despite differences in size between sand grains and stone gravels or cobbles.[15,16] Assumptions 3 and 4 are choices that limit the application of the nomogram but simplify its design. Ice may still be used, but its impact on, say, the temperature of water at mixing would be assessed outside the present nomogram.

Under these assumptions and the assumption that mixing occurs much faster than any heat transfer with the surroundings, conservation of energy yields:

$$m_w c_w (T_w - T_{c,fresh}) + c_a h m_{cm} * (T_{cm} - T_{c,fresh}) + m_a (T_a - T_{c,fresh}) i = 0 \quad (1)$$

where, m_w is mass of water per unit volume of concrete; c_w is specific heat of water; T_w is temperature of water upon mixing; c_a is specific heat of aggregate and cement; m_{cm} is mass of cement per unit volume of concrete; T_{cm} is temperature of cement upon mixing; m_a is mass of aggregates, fine and coarse, per unit volume of concrete; T_a is temperature of aggregates; and $T_{c,fresh}$ is final equilibrium temperature of freshly mixed concrete.

The highest theoretical temperature for hydrating concrete is simply the temperature upon placement plus the adiabatic temperature rise:

$$T_{c,max,a} = T_{i,c} + \Delta T_a \quad (2)$$

where, $T_{c,max,a}$ is the maximum attainable concrete temperature (adiabatic conditions); $T_{i,c}$ is the initial concrete temperature upon placement; and ΔT_a is the adiabatic temperature rise.

The initial temperature $T_{i,c}$ will be a few degrees warmer than the freshly mixed temperature $T_{c,fresh}$, but this does not pose a difficulty in using the subsequent nomogram. The adiabatic temperature rise ΔT_a can be determined from calorimetry or, for example, from:

$$\Delta T_a = \frac{H_u C_c \alpha_u}{\rho_c c_c} \quad (3)$$

where, H_u is the ultimate energy released by hydration of cement(itious) materials at 100 percent hydration; C_c is the mass of cement(itious) material per unit volume of concrete; and α_u is the ultimate degree of hydration.

All of these variables may be calculated from knowledge of the cement chemistry.[17,18] Equations 1 and 2 are closed-form equations expressible as nomograms; Figure 12 shows the result. In this nomogram, the axis labeled "Maximum Adiabatic Concrete Temperature" is colored red for temperatures 165°F and above, in line with GDOT's threshold.

The dashed line is an isopleth that depicts a sample solution. As with most nomograms, there is no need to consider any part of an input or an output, as it depicts a self-consistent relation among variables. We can, therefore, read the nomogram starting with an arbitrary variable and ending with another variable. In Figure 12, we may, for example, start with the temperature of fresh concrete at 70°F and ask what would be the maximum temperature possible with this concrete with this as the temperature upon emplacement; to find this we simply draw a line from 70°F on the "Fresh Concrete" axis, through the adiabatic temperature rise value on the "Adiabatic Temperature Rise" axis (about 115°F for this concrete), and to this line's intersection with the "Maximum Adiabatic Concrete Temperature" axis, which is about 185°F in this example. To the left of the "Fresh Concrete" axis, a user can determine temperatures of the concrete components that are consistent with a fresh concrete temperature; in this example, if the aggregates are at 63°F and the cement is at 100°F, then 70°F water is required.

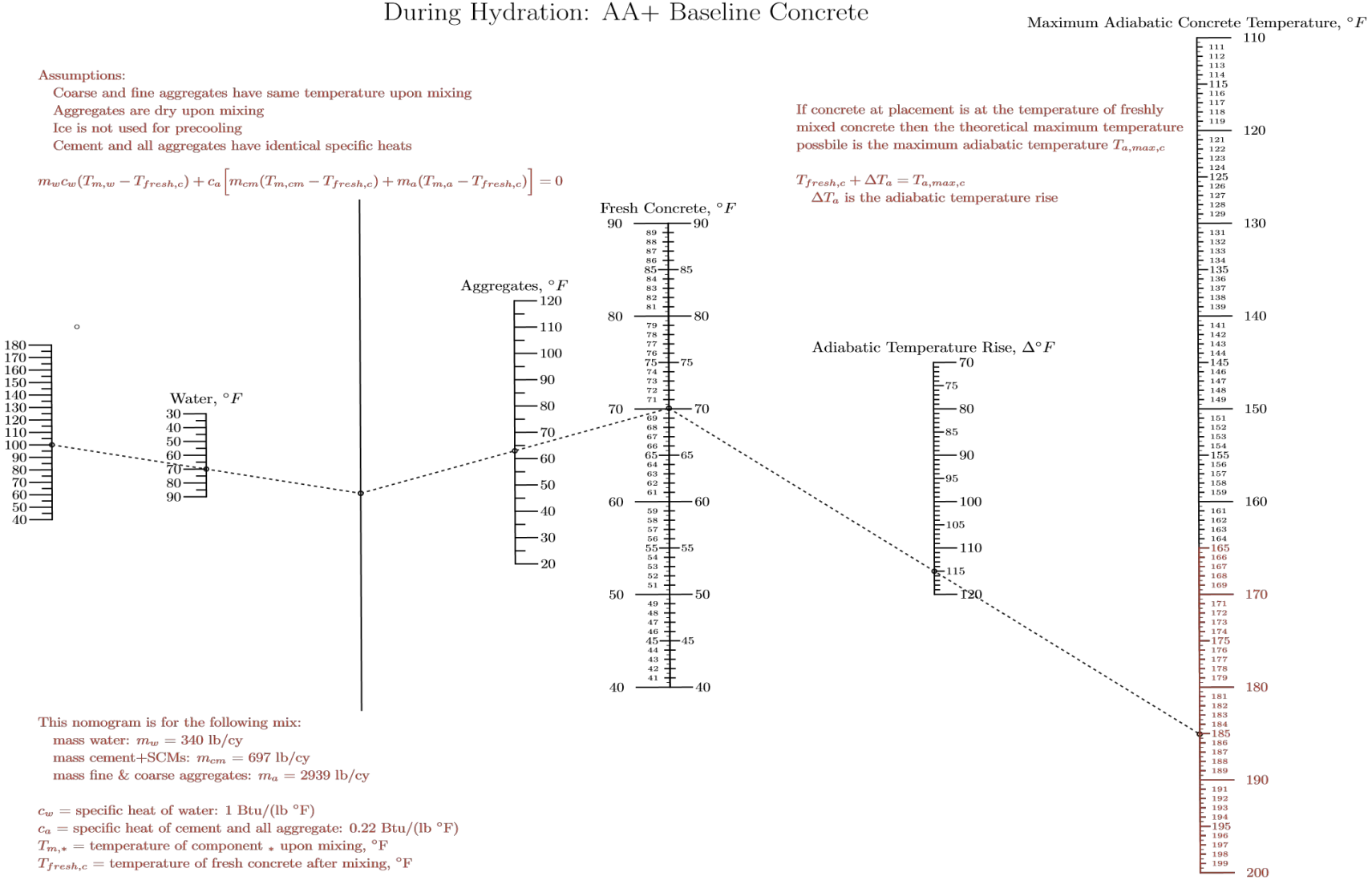

Figure 12. Illustration. Mixed concrete temperature and worst-case maximum temperature.

As an exercise (not depicted with an isopleth in Figure 12), if we wish the maximum temperature to be below the GDOT threshold, say 160°F, then connecting this point with the adiabatic temperature rise of 115°F shows the required temperature upon emplacement to be 45°F. If the fresh concrete is 70°F, then 25°F of precooling is required. Or, one could read the nomogram to find that for a fresh concrete temperature of 45°F, given water chilled of 40°F and cement at 80°F, the aggregates would need to be 40°F. Note that the fresh concrete temperature may not be the same as the placement (a.k.a. initial) temperature due to the time for mixing and pouring being enough that the concrete can be warmed by the surroundings. However, this should not impact the results given by this nomogram.

It should be acknowledged that mass concrete approaches, but may not reach, the adiabatic conditions that lead to concrete temperatures being the sum of initial temperature and adiabatic temperature rise; most projects will experience lower temperature rises. Therefore, results from the nomogram in Figure 12 give the maximum theoretically possible concrete temperatures during hydration. If an achievable, economical solution on this nomogram indicates temperatures below the threshold (perhaps by a few degrees as a safety factor), then one can be reasonably confident that the actual, non-postcooled emplacement will not exceed this threshold.

If the use of this nomogram suggests that adiabatic temperatures cannot be kept below the threshold, then the nomograms for cases 2 and 3 may be consulted as follows:

- To check if the actual size of the emplacement—and the attendant nonadiabatic conditions—may lead to sufficiently low temperatures that postcooling is not needed, and failing this (case 2).
- To choose an initial postcooling plan, i.e. the spacing of pipes, cooling water temperature, pipe size (case 3).

Most mass concrete emplacements do not exhibit adiabatic behavior for sufficiently long that the maximum temperature closely approaches the maximum adiabatic temperature. Nevertheless, we suggest that this nomogram be consulted at the outset as it can provide an upperbound check on the results from the case 2 nomogram: being based on a regression of simulation results, it may be the case that some regions of the nomogram extrapolate beyond the validity of the model. If temperatures from a case 2 nomogram are greater than those for the case 1 nomogram for a given initial temperature and concrete, then the case 2 nomogram result is incorrect and alternate analyses should be pursued.

Cases 2 and 3: General Considerations

Cases 2 and 3 involve transient, multidimensional heat transfer with a nonlinear term modeling hydration. As such, closed-form exact solutions of the governing (partial differential) equations do not exist. Here, as with references 12 and 13, we use a surrogate modeling approach in which results from many numerical simulations are regressed to define a closed-form equation that encapsulates those simulation results. This regressed equation is then converted into nomogram form.

The governing equation for the temperature of the concrete is given by the heat diffusion equation with a source term for cement hydration:

$$\rho_c c_c \frac{\partial T_c}{\partial t} = \kappa_c \nabla^2 T_c + \dot{e}_{gen} \tag{4}$$

Here, T_c is concrete temperature as a function of space and time t, and $\dot{e}_{gen}$ is a source term accounting for the thermal energy generated by hydration; $\dot{e}_{gen}$ is often termed "heat of hydration." For the AA+ baseline concrete, we model $\dot{e}_{gen}$ using the Arrhenius-based three-parameter maturity model:

$$\dot{e}_{gen} = H_u C_c \left\{ \left(\frac{\tau}{t_e} \right)^{\beta} \left(\frac{\beta}{t_e} \right) \alpha_u exp\left(- \left[\frac{\tau}{t_e} \right]^{\beta} \right) \right\} \left\{ exp\left(\frac{E_a}{R} \left[\frac{1}{T_r} - \frac{1}{T_c} \right] \right) \right\} \tag{5}$$

where, all temperatures are absolute thermodynamic temperatures; H_u is the ultimate energy released by hydration of cement(itious) materials at 100 percent hydration; C_c is the mass of cement(itious) material per unit volume of concrete; α is the time-varying degree of hydration; E_a is the apparent activation energy; R is the universal gas constant; T_r is a reference temperature (here taken to be 294.25 K = 21.1°C); τ is a time parameter encoding a delay in onset of hydration after mixing; β is a shape parameter encoding rate of hydration; and t_e is the equivalent age given by:

$$t_e = \int_{t=0}^{t} exp\left(\frac{E_a}{R}\left[\frac{1}{T_r} - \frac{1}{T_c}\right]\right) dt \approx \sum_{t=0}^{t} exp\left(\frac{E_a}{R}\left[\frac{1}{T_r} - \frac{1}{T_c}\right]\right) \Delta t \tag{6}$$

where, Δt is the simulation timestep; and empirical relations for the parameters H_u, E_a, α_u, τ, and β can be found in references 17 and 18.

For the SR-92 concrete, we model $\dot{e}_{gen}$ from calorimetry and the adiabatic temperature history conducted for Task 3. This adiabatic temperature history is then used to find the parameters of the $\dot{e}_{gen}$ model of Cervera et al.[19] Note that in doing this, we do not consider this model to be a true representation of the underlying physics and chemistry but employ it as a curve fit to data that yields a computationally convenient calculation recipe.

The Cervera model begins similar to other models, relating rate of energy generation to rate of change of the degree of hydration:

$$\dot{e}_{gen} = H_u C_c \frac{d\alpha}{dt} \tag{7}$$

but rather than use a maturity concept to model $\alpha(t)$, an Arrhenius-type relation models rate of change of α directly:

$$\frac{\partial \alpha}{\partial t} = A(\alpha) \cdot exp\left(- \frac{E_a}{RT_c} \right) \tag{8}$$

where, $A(\alpha)$ is a normalized affinity that can be expressed in terms of the adiabatic concrete temperature history $T_{c,a}$ as:

$$A(\alpha) = \frac{\alpha_u}{\Delta T_{c,a}} \frac{\partial T_{c,a}}{\partial t} \cdot exp\left(\frac{E_a}{RT_{c,a}} \right) \tag{9}$$

$A(\alpha)$ can also be modeled with polynomials of varying degrees.[19,20,21] Here, we use the polynomial used by Cervera et al.[19]:

$$A(\alpha) = \psi_1 \left(\psi_2 + \alpha \right) \left(\alpha_u - \alpha \right) \cdot exp\left(- \psi_3 \frac{\alpha}{\alpha_u} \right) \tag{10}$$

where, ψ_* are material properties experimentally determinable by regressing equations 9 and 10 together on adiabatic temperature histories and initial concrete temperatures $T_{i,c}$. Here, we take ψ_* of the form:

$$\begin{aligned} \psi_1 &= \gamma_{1,0} T_{i,c}^2 + \gamma_{1,1} T_{i,c} + \gamma_{1,2} \\ \psi_2 &= \gamma_{2,0} cos\left[\gamma_{2,1} \cdot \left(\frac{T_{i,c} - T_{i,c,min}}{T_{i,c,max} - T_{i,c,min}} \right) + \gamma_{2,2} \right] + \gamma_{2,3} \\ \psi_3 &= \gamma_{3,0} T_{i,c}^2 + \gamma_{3,1} T_{i,c} + \gamma_{3,2} \end{aligned} \tag{11}$$

where, $T_{i,c,min}$ and $T_{i,c,max}$ are the minimum and maximum initial temperatures used in the set of "virtual" adiabatic temperature increase experiments for regression. The ultimate product of these regressions is the values for the parameters γ_*. Equations 7, 8, 10, and 11

thus constitute a complete experimentally derived model for $\dot{e}_{gen}$ as a function of initial concrete temperature.

Figure 13 depicts a sample comparison of adiabatic temperatures for the SR-92 concrete derived from isothermal cement calorimetry and simulated adiabatic temperatures using the three-parameter model and the Cervera model fitted to isothermal cement calorimetry.

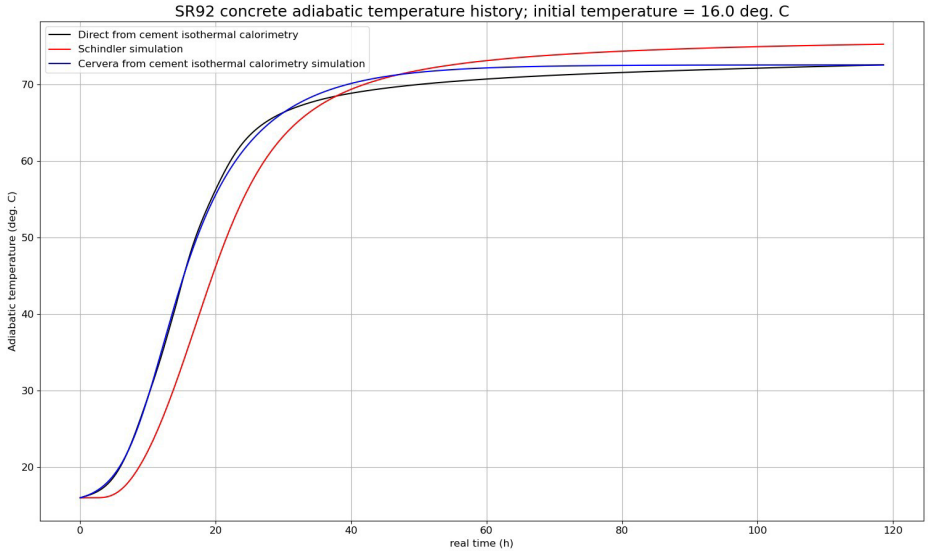

Figure 13. Graphs. Initial concrete temperature: 16°C.

Case 2: No Postcooling

For emplacements that are not postcooled, a series of three-dimensional finite element simulations were run on cuboids of varying sizes and shapes, initial temperatures, and ambient temperatures. The governing equation is equation 12 in Cartesian coordinates:

$$\rho_c c_c \frac{\partial T_c}{\partial t} = \kappa_c \left(\frac{\partial^2 T_c}{\partial x^2} + \frac{\partial^2 T_c}{\partial y^2} + \frac{\partial^2 T_c}{\partial z^2} \right) + \dot{e}_{gen} \tag{12}$$

where for this case, the hydration term $\dot{e}_{gen}$ is modeled using the three-parameter model of equations 5 and 6 with the parameters computed with the relations of references 17 and 18 for concrete A. The boundary condition on the bottom surface ($x,y,z = 0$) is conservatively taken to be adiabatic:

$$\left.\frac{\partial T_c}{\partial z}\right|_{z=0} = 0 \tag{13}$$

and a convective condition is applied on all other sides dS:

$$-\kappa_c \frac{\partial T_c}{\partial n} = h_c \left(T_c - T_\infty\right) \tag{14}$$

where, n indicates the normal to the surface is a convection coefficient (assumed constant), and T_∞ is the ambient temperature, taken here to be constant and indicative of the average temperature over early concrete age. Initial conditions are:

$$T_c(x,y,z,t = 0) = T_{i,c} \tag{15}$$

Here, solar radiation was not modeled.

Equations 13 through 15 were simulated using the open-source finite element platform FEniCS version 2019.1.0.[22,23] As a check on this implementation, a simulation was conducted and compared to the SR- 92 footing, monitored as described in Task 1; figure 14 shows a reasonable match.

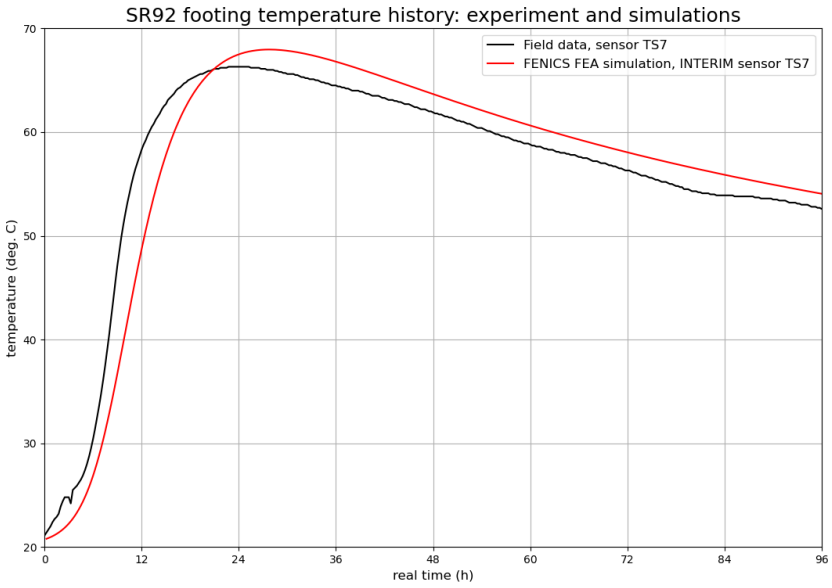

Figure 14. Illustration. FEniCS validation.

Thirty cuboids were simulated, as shown in Figure 15, in which V is the cuboid volume and qA is the area of the sides and top of the cuboid, from which heat transfer q may occur between concrete surfaces and the surroundings. Table 4 gives the combinations of initial and ambient temperatures (17 scenarios) for each cuboid. Each of the 30 cuboids was simulated for each of the 17 scenarios, for a total of 510 simulations, each of which was run to model 96 hours = 4 days of curing. To save computational time, symmetry used to limit the domain of each simulation was one-quarter of a cuboid with symmetry conditions applied at each subdividing plane. In all cases the convection coefficient h was taken to be 23 $W/(m^2K)$.

Figure 15. Illustration. Case 2 cuboids.

Table 4. Case 2 scenarios.

$TT_{\emptyset}$, °F	$TT_{ii,cc}$, °F
40	40
40	50
50	50
50	60
50	70
60	50
60	60
60	70
70	50
70	60
70	70
70	80
80	50
80	60
80	70
80	80
80	90

For each simulation, the maximum concrete temperature at any time and any location $T_{max,c}$ in the simulated domain was found. To relate this maximum temperature to the parameters and ensure dimensional consistency, scaling arguments were used to postulate a dimensionally consistent relation that was then regressed on simulation data using the Python package statsmodels to determine the constants of the relation.[24,25,26] In dimensional form, this relation can be written:

$$T_{max,c} = C_1 \cdot T_{i,c}^{g} \cdot qA^{h} \cdot V^{j} \cdot T_{\infty}^{k} \tag{16}$$

where, $C_1 = ac_c^m \cdot \kappa_c^n \cdot \rho_c^p \cdot \Delta T_a^q$ is a constant for a given concrete and the exponents $\{g,h,j,k,m,n,p,q\}$ are found by the regression. Equation 16 is a surrogate model that

encapsulates the simulations on which it is regressed and may be converted into nomogram form.

Running several regressions, the researchers found that differences between simulations and the surrogate model are reduced if we limit the regressions and nomograms to larger geometries in which the volume to heat transfer area is ≥1 ft. Figure 16 and Figure 17 depict the differences between the simulations and the surrogate model, as it is important to be aware that the nomograms constructed from the surrogate model have errors built into them and thus should be considered as giving approximate solutions that should be confirmed with more detailed analyses.

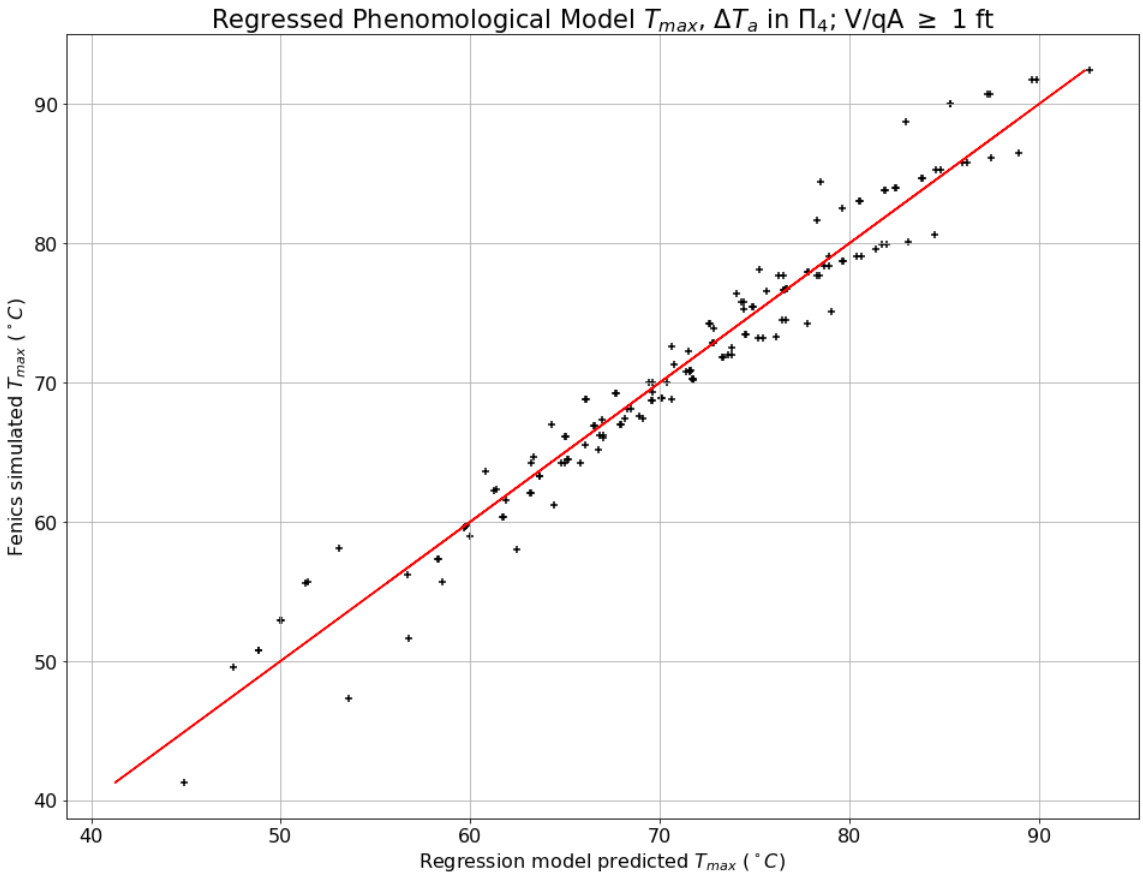

Figure 16. Graph. No-postcooling surrogate model compared to simulation results.

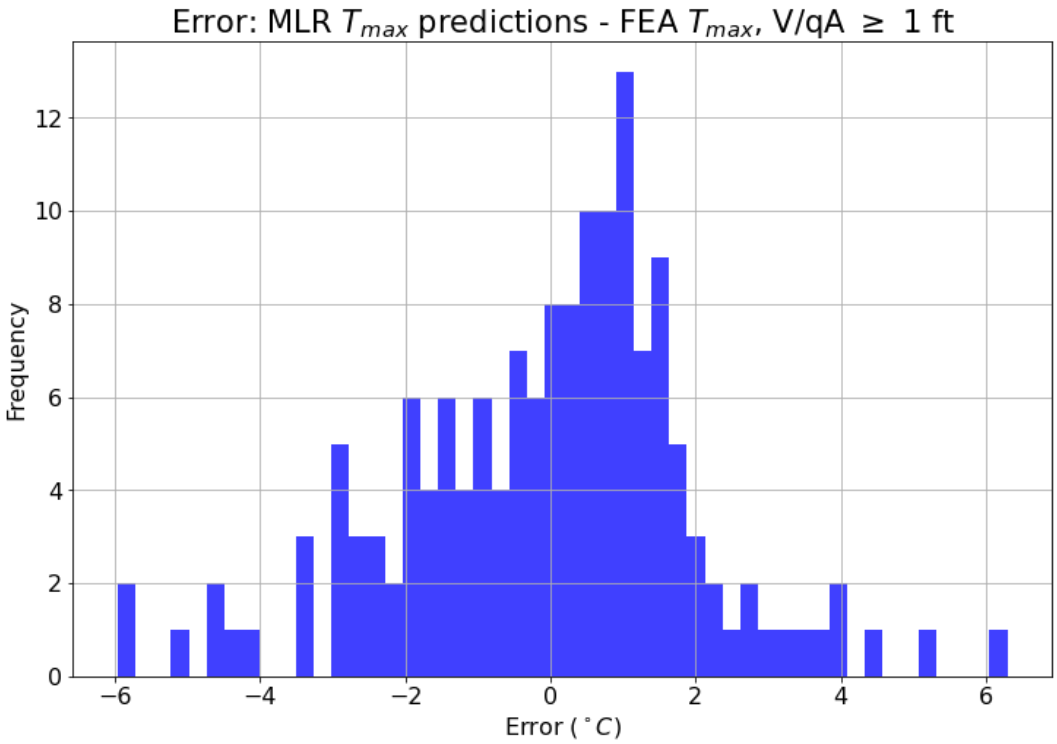

Figure 17. Graph. No-postcooling histogram of surrogate model error from simulation results.

The nomogram that comes from the surrogate model is depicted in Figure 18. The isopleth, in this case, is red for better visibility. The example it gives is for a cuboid 4 ft wide, 9 ft deep, and 15 ft high (see the bottom right cuboid in Figure 15) using as the initial temperature the fresh concrete temperature of the nomogram in Figure 12 and an average ambient temperature of 80°F. From the initial temperature axis value of 70°F, cross over to the right and find the point at which $qA \approx 426$ ft^2; drop straight down to where the volume $V \approx 540$ ft^3 = 20 yd^3; then move to the left where the ambient temperature line T_∞ = 80°F; then go up to the intersection with the maximum temperature axis, showing the estimated maximum temperature to be 168°F.

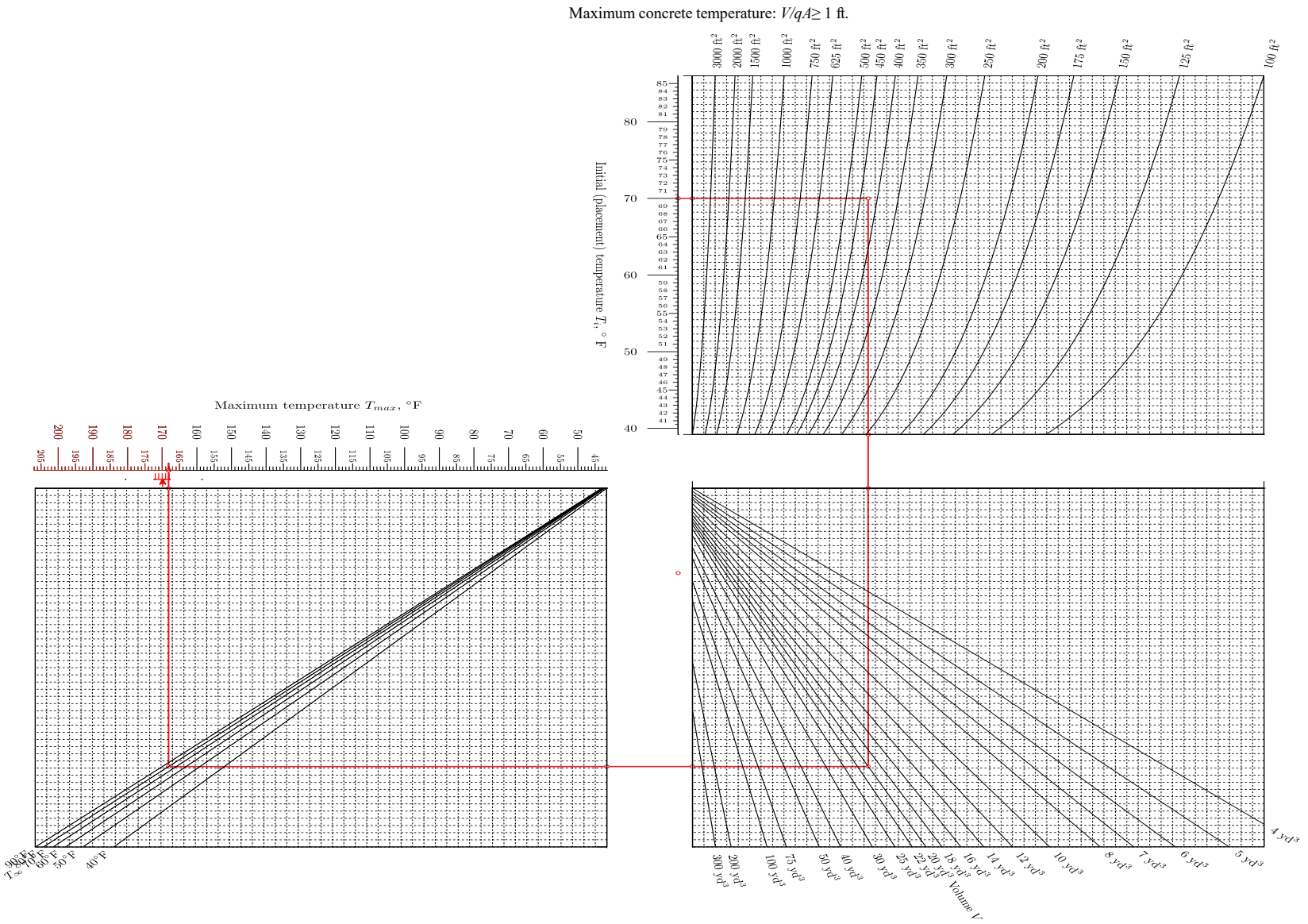

Figure 18. Illustration. No-postcooling nomogram.

Note that the nomogram of Figure 12 gives a worst-case maximum temperature of 185°F, indicating that this situation is far from being adiabatic.

Note also that the nomogram has a quartile plot under the maximum temperature axis that embeds a summary of the histogram of errors of Figure 17: the "whiskers" show the 25th to 75th percentiles, and the dots show the greatest errors. The small upward-pointing arrow shows the finite element simulation result for this case, which here is 170°F. In this case, the nomogram results in a 2°F underestimation of the temperature and is just within the 25th to 75th percentile range. In this case the error is relatively small, but it should be noted that such error is always present.

Another example, left to the reader, is to work back from a desired maximum temperature, say 160°F as before. Doing this suggests that the initial concrete temperature should be approximately 60°F, compared to the 40°F value for an adiabatic situation. Figure 19 depicts the same nomogram with an isopleth showing an out-of-sample case, that is, an example that was not in the set of finite element simulations that underpin the surrogate model. Here the out-of-sample case is the SR-92 wall as if it were not postcooled using the AA+ baseline concrete from Phase I of this project, and the initial temperature was 70°F. The nomogram gives a maximum temperature of 182°F, whereas a finite-element simulation gives 180°F, an overestimation of 2°F. Note that the case 1 nomogram gives a maximum possible temperature of 185°F for this case.

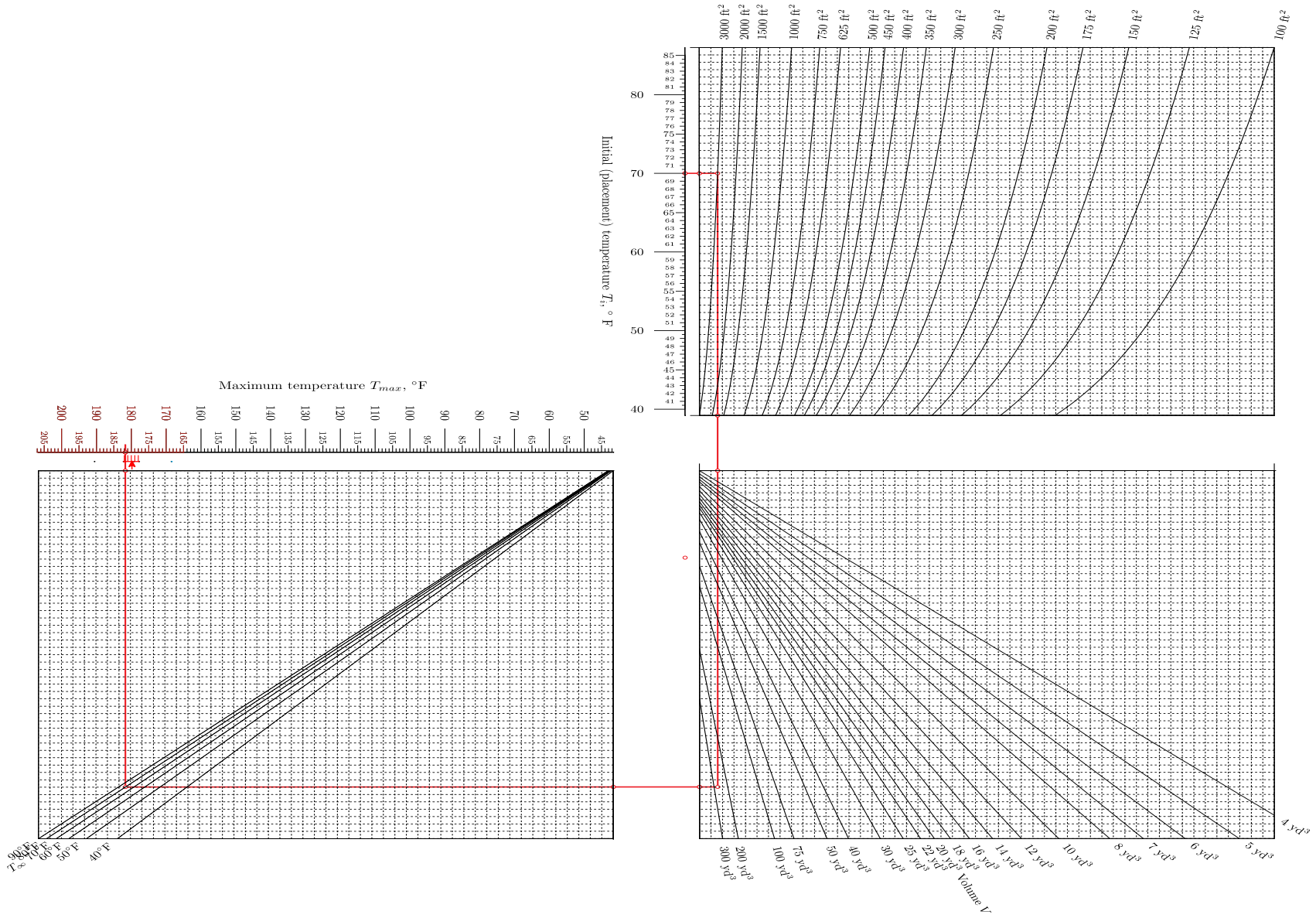

Figure 19. Illustration. No-postcooling nomogram. The isopleth is an out-of-sample calculation representing a real-world example: the SR-92 wall as if it were not postcooled using AA+ baseline concrete from Phase I.

Case 3: Postcooling

Two different postcooling situations were modeled: (1) a single cylinder of concrete with a cooling pipe along its axis, and (2) a three-dimensional array of pipes of varying arrangements. In both situations, the hydration term $\dot{e}_{gen}$ is modeled following Cervera et al. via equations 7, 8, 10, and 11 for the SR-92 concrete.[19] Flow rates were all taken to be such that flows are fully turbulent.

The single-cylinder simulations used a dimensional form of the model of Myers et al.[27] that describes concrete temperatures in the radial direction and water temperatures along the axial pipe. In this model, the heat transfer in the axial direction of the concrete is shown to be negligible; thus, the governing equation in cylindrical coordinates simplifies to:

$$\rho_c c_c \frac{\partial T_c}{\partial t} = \kappa_c \frac{1}{r} \frac{\partial}{\partial r}\left(r \frac{\partial T_c}{\partial r} \right) + \dot{e}_{gen} \tag{17}$$

where, r is the coordinate. Initial conditions are expressed, as before, as $T_c(r,z,t = 0) = T_{i,c}$. The outer surfaces of the concrete, i.e., the cylindrical surface at maximum radius $r = r_c$ and the capping doughnut surfaces at $z = 0$ and $z = L$, are adiabatic.

The pipe wall is not modeled explicitly (i.e., temperatures within the pipe wall are not simulated) and the impact of pipe geometry and material is incorporated into the boundary condition for the concrete at $r = r_p$, the outer radius of the pipe/inner radius of the (hollow) concrete cylinder:

$$\kappa_c \left. \frac{\partial T_c}{\partial r} \right|_{r=r_p} = H\left(T_c|_{r=r_p} - T_w \right) \tag{18}$$

where, H is a heat transfer coefficient that encapsulates conduction through the pipe wall

and fully developed turbulent convection between the inner pipe surface and the flowing water:

$$H = \frac{1}{r_p}\left(\frac{ln(r_p/r_{pi})}{\kappa_p} + \frac{1}{h_p r_{pi}}\right)^{-1} \tag{19}$$

where, r_{pi} is the inner radius of the pipe, κ_p is the thermal conductivity of the pipe material, and h_p is the convection coefficient within the pipe as computed using the Darcy friction factor and the Gnielinski correlation.[15,28,29]

The temperature of the water is modeled by:

$$\frac{\dot{V}}{\pi r_p^2}\frac{\partial T_w}{\partial z} = \frac{2H}{\rho_w c_w r_p}\left(T_c|_{r=r_p} - T_w\right) \tag{20}$$

where, V is the water volume flow rate; T_w is the water temperature; and ρ_w and c_w are the density and specific heat of water, respectively. The boundary condition is $T_{e,w} = T_w(z = 0,t)$ where $T_{e,w}$ is the water temperature at the entrance of the pipe. Note that equations 17 and 20 are one-dimensional, but in different directions; we will refer to this model as being quasi-one-dimensional. This model was implemented in the open-source spectral method solution package Dedalus due to the ease with which equation 17 for the concrete can be solved with spectral methods near simultaneously with equation 20 for the water, which is solved using an explicit Euler scheme at each timestep.[30]

Despite the limitations of this model (no connection to the surrounding environment, only one pipe), its relatively simple nature and computational efficiency compared to a full 3D simulation with an array of pipes facilitates the exploration of the parameter space, which is larger for postcooling that for the case without postcooling (additional parameters include, e.g., pipe sizes and lengths, concrete cylinder radii, water flow rates, and inlet temperatures

in addition to initial concrete temperature). To enable efficient coverage of this parameter space, the Python package scikit-optimize[1] was used to to select samples by Latin hypercube sampling (LHS) given the static choice of SR-92 concrete and PEX tubing.(31,32) In total, 2,700 distinct simulations were run, and as with the no-postcooling case, the maximum concrete temperature at any place and time $T_{max,c}$ was found and stored for each simulation.

An additional caveat with this quasi-one-dimensional model is that it likely informs only situations in which pipes are tightly packed so that the adiabatic boundary condition on the outer surface of the cylinder can be approximated. We postulate that hexagonal packing (see Figure 20 for an example) may be informed by this model, something that will be discussed in the following sections.

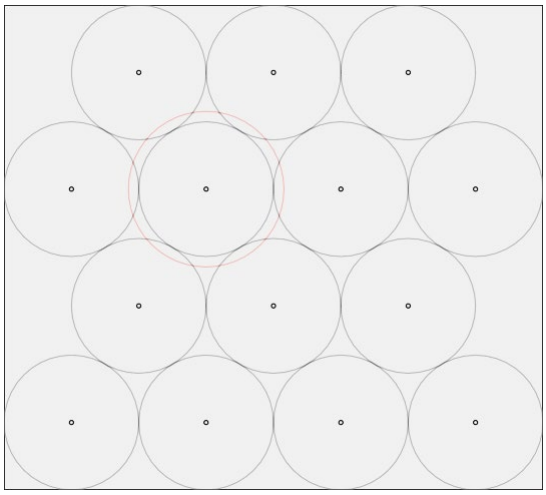

Figure 20. Illustration. Hexagonal packing. The small solid circles represent pipes. The gray circles centered on the pipes are a representation of the physical spacing, whereas the red circle is a postulated "effective thermal spacing."

To test the applicability of the quasi-one-dimensional model to hexagonal packing as well as square or rectangular packing as in Figure 21 and Figure 22, full 3D simulations for the

[1] https://scikit-optimize.github.io/stable/.

latter two pipe array types were run with FEniCS[2] using the concrete model of equation 12 combined with the water model in equation 20.

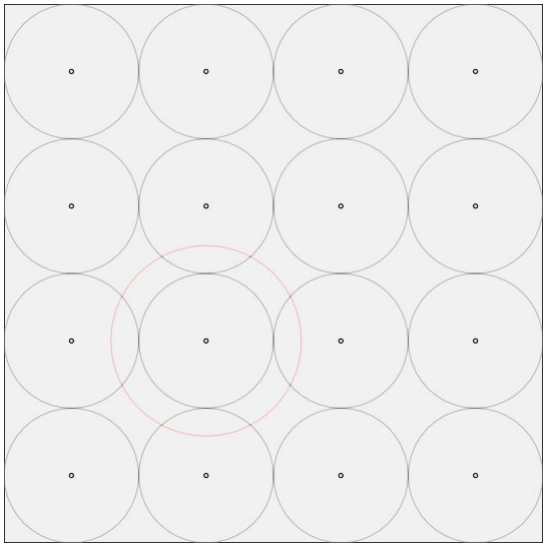

Figure 21. Illustration. Square packing. The small solid circles represent pipes. The gray circles centered on the pipes are a representation of the physical spacing, whereas the red circle is a postulated "effective thermal spacing."

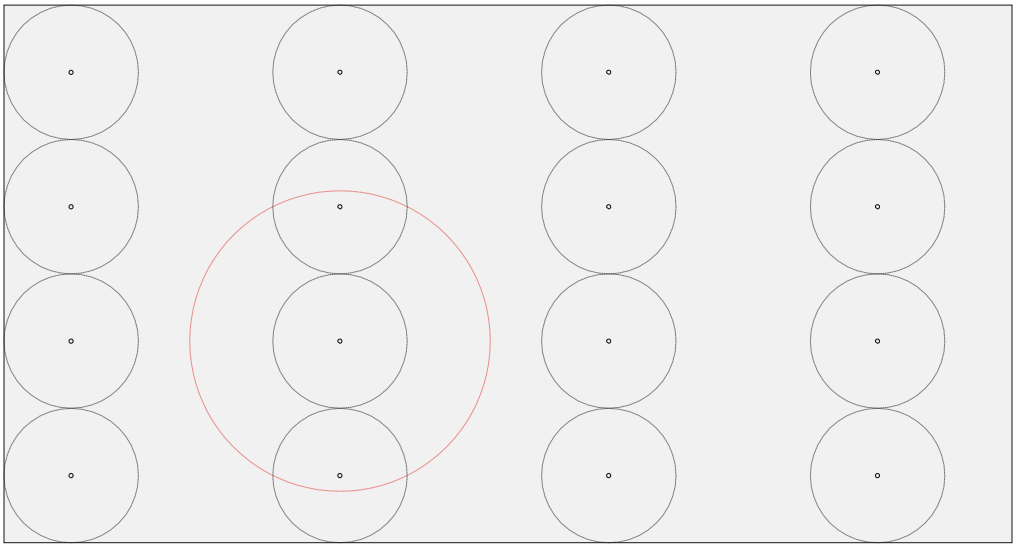

Figure 22. Illustration. Rectangular packing. The small solid circles represent pipes. The gray circles centered on the pipes are a representation of the minimum physical spacing, whereas the red circle is a postulated "effective thermal spacing."

[2] Meshes were created here with Gmsh.[(33)]

To validate the implementation of the models described above, the quasi-one-dimensional model and the full 3D models were tested against an exact analytical solution for the temperature field of a two-layer hollow cylinder with constant $\dot{e}_{gen}$ in one or both layers.

Specifically, this exact solution is one-dimensional so that the "cylinder" it models is, in fact, a disk with convective boundary conditions; using the notation of Cole,[34] the situation is labeled R3C13B00TOOG11, and details of the solution can be found in the Exact Analytical Conduction Toolbox (EXACT).[35] In this case, the exact solution was configured to mimic PEX tubing encased in a concrete cylinder with the adiabatic condition at the outer cylinder and convection derived from water flow rates in the inner hollow of the disk. A constant $\dot{e}_{gen}$ = 974 W/m^3, equal to the total energy of hydration of SR-92 concrete released at a constant rate over 36 hours, was applied to the concrete, with $\dot{e}_{gen} = 0$ for the pipe layer. Initial and water entrance temperatures were taken to be 0°C, a choice that makes for convenient computation of the exact solution. Further details are given in Table 5. Results from the quasi-one-dimensional and 3D simulations were taken at the entrance plane of the respective cylinders.

Table 5. Parameters used in comparisons to exact solution R3C13B00TOOG11.

Test #	PEX Pipe Size	r_c, m	V^*, L/m
1	½ in.	0.20	9.5
2	¾ in.	0.52	21

Figure 23 and Figure 24 show that both simulations match well to the exact solution and indicate that the treatment of heat transfer through the pipe wall is adequately handled in the model of Myers et al.[27]

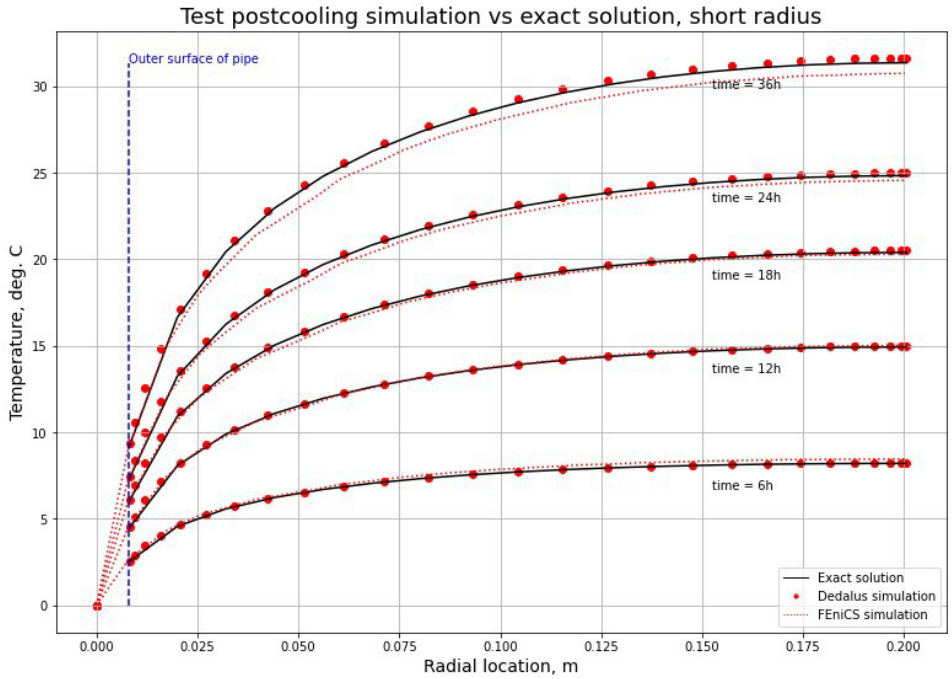

Figure 23. Graphs. Validation against exact solution, test 1.

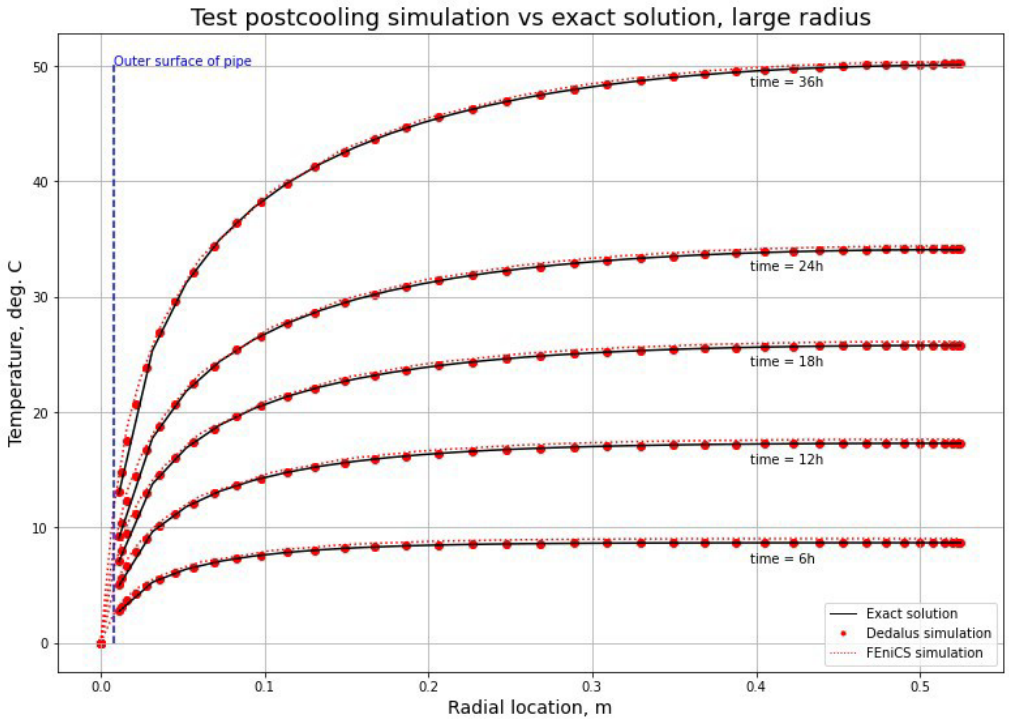

Figure 24. Graphs. Validation against exact solution, test 2.

As the 3D simulations are much more computationally intensive, we take advantage of the speed of the quasi-one-dimensional model to conduct informal and formal sensitivity analyses to inform a judicious choice of geometries and scenarios to model.

Informal inspection of the $T_{max,c}$ data from the quasi-one-dimensional simulations suggests pipe spacing, along with initial temperature, have dominating impacts on temperatures; as found by Myers et al.[27] In contrast, water flow rates—given fully turbulent flow—and lengths of the cylinder have only minor impacts with PEX tubing, although this may not be the case with metal pipes where the thermal conductivity of the pipe does not dominate the coefficient H as it does with PEX piping.[27] Regressions on $T_{max,c}$ data performed with statsmodels, similar to the no-postcooling cases, confirmed these informal observations and revealed that the top four parameters with the most impact on maximum temperatures are:

- Initial temperature.
- Pipe spacing (i.e., represented by concrete radius in the quasi-one-dimensional model).
- Water inlet temperature.
- Pipe size (that is, diameter and wall thickness, together represented by the nominal pipe size).

These parameters are all largely in line with Myers et al[27] with the exception that they found volume flow rate to be significant. We suspect this is due to their model having larger values of H, as they explored the use of metal piping which would make the convection coefficient h_p, and by extension, the volume flow rate, more influential.

As a check on this, we instead perform a more formal Sobol sensitivity analysis using the Python package SALib on full 3D simulations of square packing of ½-inch PEX tubing.[36,37] These simulations employed the same boundary conditions as with the no-postcooling 3D simulations and likewise exploited symmetry so that only one-quarter of the 1.2 m = 4 ft wide × 1.2 m = 4 ft deep domain need be solved. Tests indicated that at cuboid heights greater than 0.91 m = 3 ft, the surrounding ambient conditions do not impact $T_{max,c}$ for this width, depth, and height, so further sensitivity tests were run with a height of 1.1 m = 3.5 ft to be conservative. SALib was used to generate samples with varying initial temperatures, inlet temperatures, volume flow rates of water, and ambient temperatures. First-order sensitivities are given in Table 6, indicating that initial temperature and inlet water temperature do indeed have key impacts, whereas volume flow rate and ambient temperatures do not.

Table 6. Sobol sensitivities.

	First-order Sensitivity
$T_{i,c}$	0.552
$T_{e,w}$	−0.271
V	0.0257
T_{∞}	0.00825

Given this, the researchers ran 3D simulations for square and rectangular packing, varying nominal pipe sizes, spacing between pipes, flow rates, water inlet temperatures, and initial temperatures for cuboids of sufficient size that the surroundings do not influence maximum temperatures $T_{max,c}$. Symmetry was used to limit the computational domain to the square or rectangular volume around the pipe with symmetry boundary conditions applied. In total, 328 distinct 3D simulations were run, a smaller number than previously due to the

smaller effective parameter space as revealed by the quasi-one-dimensional simulations. The maximum concrete temperature at any place and time $T_{max,c}$, as well as the maximum temperature at the deepest point of the cuboid[3] was found and stored for each simulation.

As with the no-postcooling case, dimensional analysis was used to find dimensionless groupings of the important parameters (as revealed by the analyses above), with a proposed surrogate model of the form:

$$T_{max,c} = C_2 T_i^{\theta} r_c^{\xi} T_w^{\upsilon} r_p^{\omega} \tag{21}$$

where, $C_2 = \beta c_c^{\phi} \nu_c^{\zeta} \Delta T_a^{\delta}$ is a constant for a given concrete; $v_c = \kappa_c/(\rho_c c_c)$ is the thermal diffusivity of the concrete; and all Greek letters are determined by the regression.

Because of the similarity in the surrogate model, postcooling nomograms have the same form as the no-postcooling nomograms. For brevity we do not present figures of surrogate model errors from simulations and only give postcooling nomograms since they contain quartile plots to indicate this model spread. For hex packing, we only give nomograms whose isopleths depict out-of-sample examples, which are full 3D simulations, so that comparison can be made with the simpler one-dimensional model that underlies the nomogram.

Figure 25 shows a nomogram for hexagonal packing. The isopleth depicts an initial temperature of 68°F, pipe to pipe spacing of 2 ft, cooling water temperature of 41°F, and ½-inch PEX tubing. The nomogram calculation shows a maximum temperature of just

[3] Chosen because it was guaranteed to be far from piping, which for some cases with smaller pipes led to isolated elements of low quality; in practice, the difference between these temperatures was negligible.

Maximum postcooled concrete temperature: PEX tubing, hexagonal packing, radial spacing < 1.5 ft
(i.e. pipe to pipe spacing < 3 ft.)

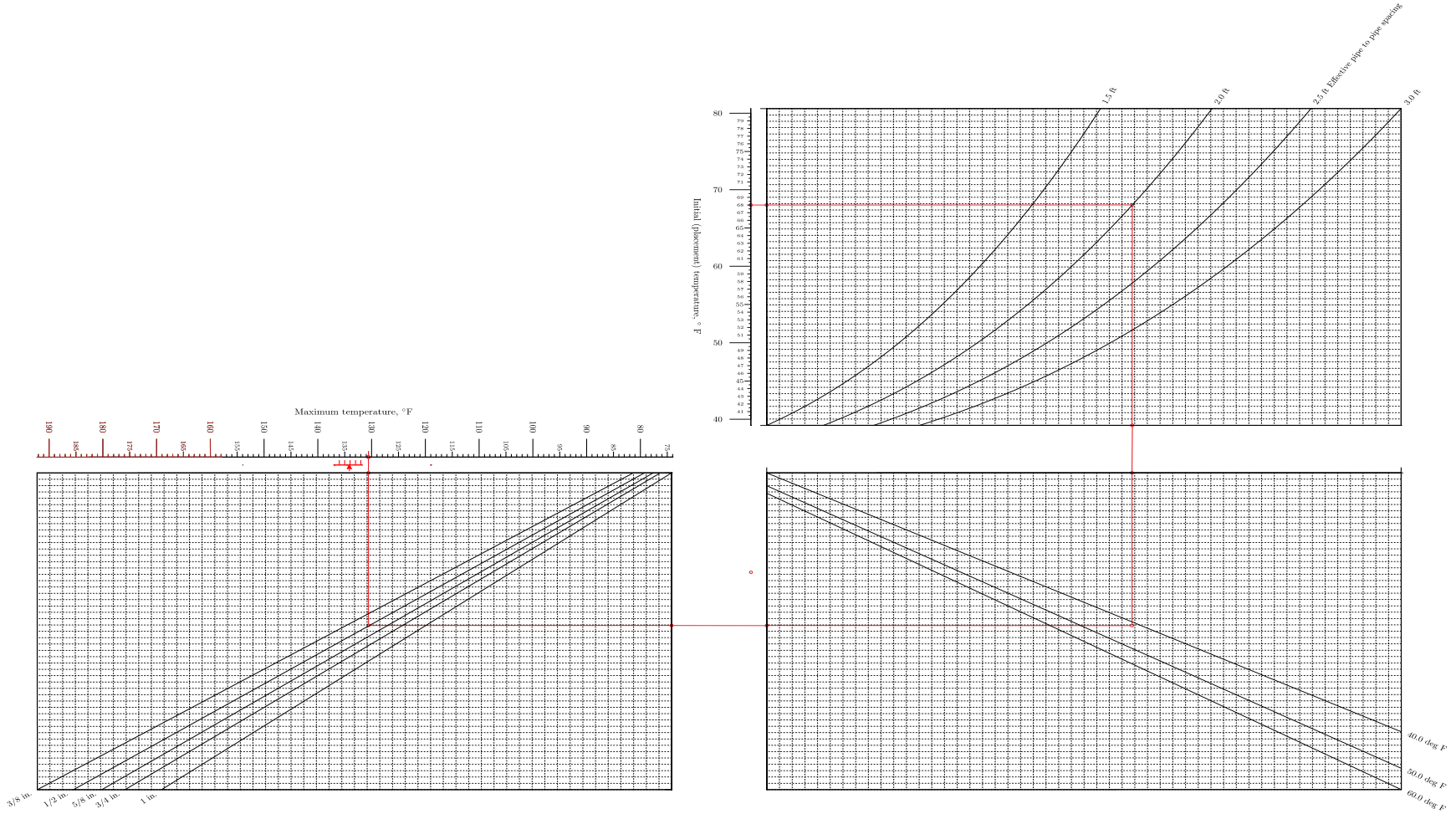

Figure 25. Illustration. Postcooling nomogram, hex packing, using physical spacing with an out-of-sample comparison.

under 131°F, whereas a full 3D simulation of this case yields a maximum temperature of 134°F and an underestimate of 3°F.

Figure 20 depicts a red circle, described in the figure caption as an "effective thermal radius." This radius is postulated to best represent the adiabatic conditions in the model used for hexagonal packing as it intersects the point equidistant from three neighboring cooling pipes. Figure 26 shows a nomogram for the case when this effective thermal radius, which gives an "effective pipe to pipe spacing" of 2.3 ft. Here the nomograms overestimate the maximum temperature by approximately 4°F.

Both these examples compare reasonably well to their out-of-sample comparisons, but this may not always be the case. Figure 27 shows that in cases of small distance between pipes,

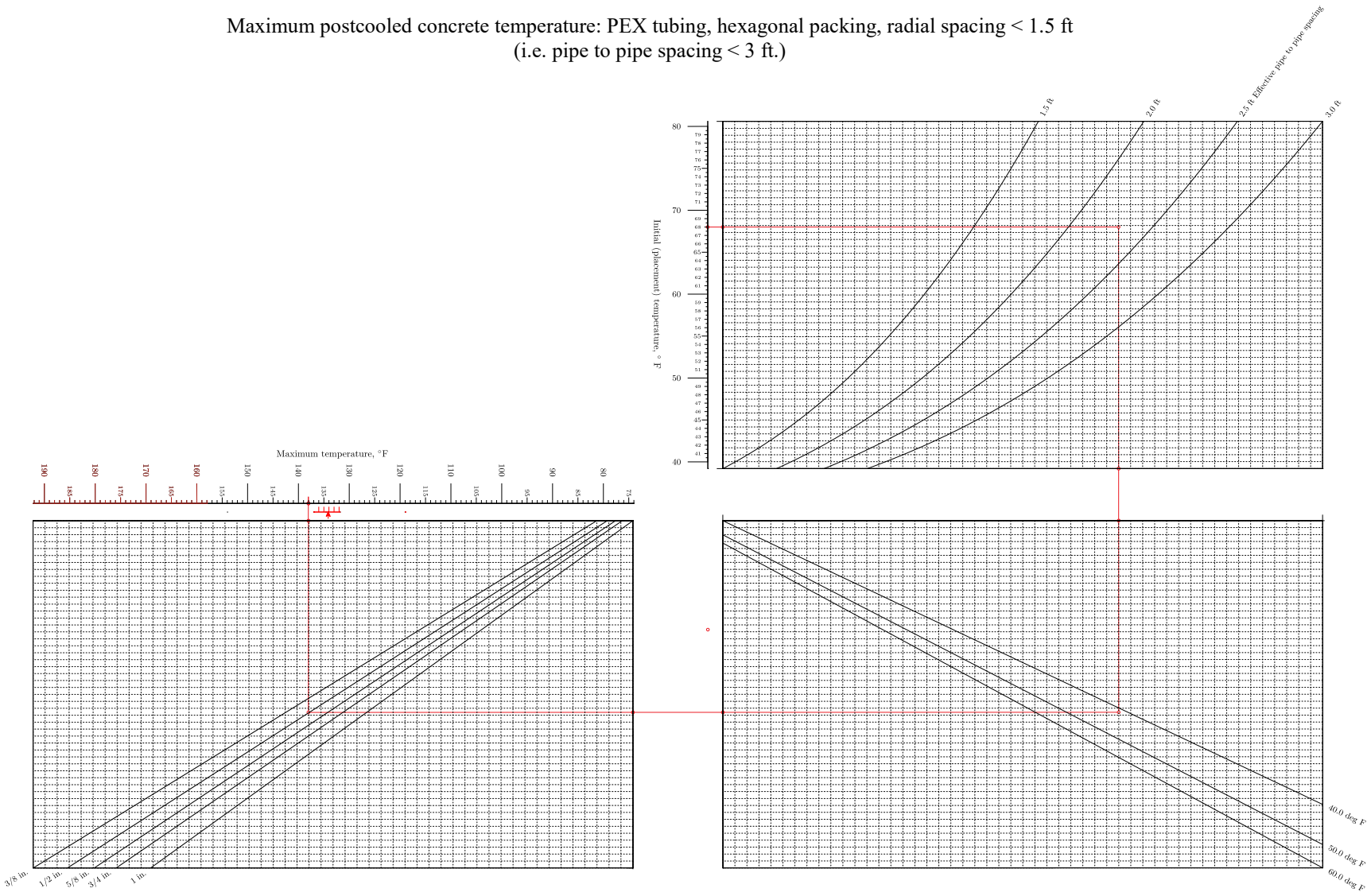

Figure 26. Illustration. Postcooling nomogram, hex packing, using an effective thermal spacing of 2.3 feet with an out-of-sample comparison.

Maximum postcooled concrete temperature: PEX tubing, hexagonal packing, radial spacing < 1.5 ft
(i.e. pipe to pipe spacing < 3 ft.)

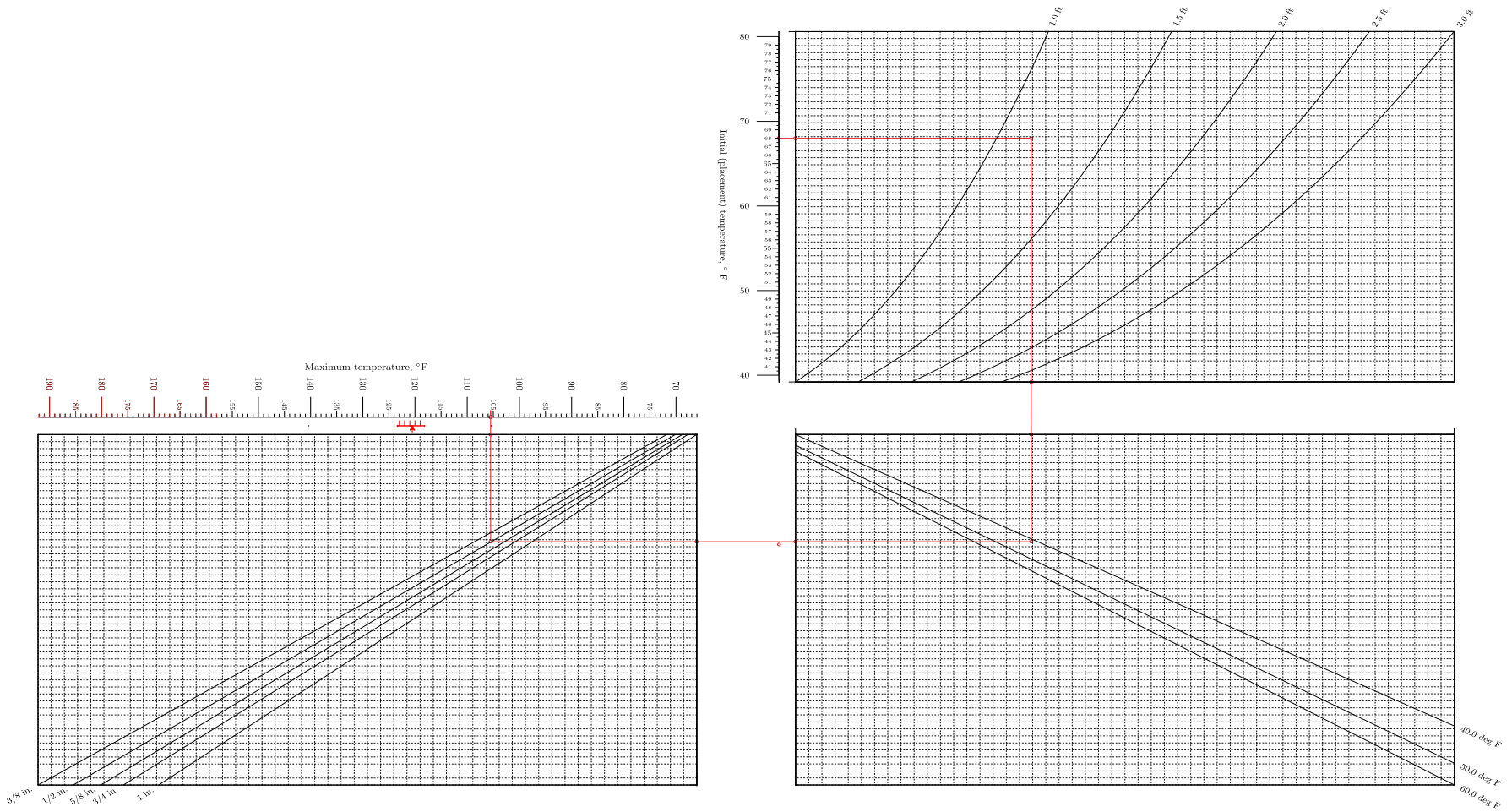

Figure 27. Illustration. Postcooling nomogram, hex packing, using an effective thermal spacing of 1.2 feet with an out-of-sample comparison.

even when using effective thermal spacing, large underestimations in the maximum temperatures may result.

As such, we recommend that pipe to pipe spacings under 1.5 ft not be used in these nomograms.

For square or rectangular packing, we postulate that only the effective thermal radius, or the effective pipe to pipe spacing, should be used. For such packing arrangements, this effective spacing is simply the diagonal distance between pipes. Use of the nomograms labeled for hexagonal packing are not recommended for square or rectangular packing arrangements: for example, 3D finite element simulations with 1 ft × 2 ft piping, 80°F initial temperature, 40°F cooling water, and ¾-inch PEX tubing gives a maximum temperature of 129°F, whereas the nomogram of Figure 27 gives a temperature of 139°F, an error of 8 percent. Figure 28 gives a nomogram based on simulations of square and rectangular packing; the isopleth is an in-sample example for a case in which the spacing between pipes is rectangular: 1-ft spacing in-depth and 2-ft spacing in width.

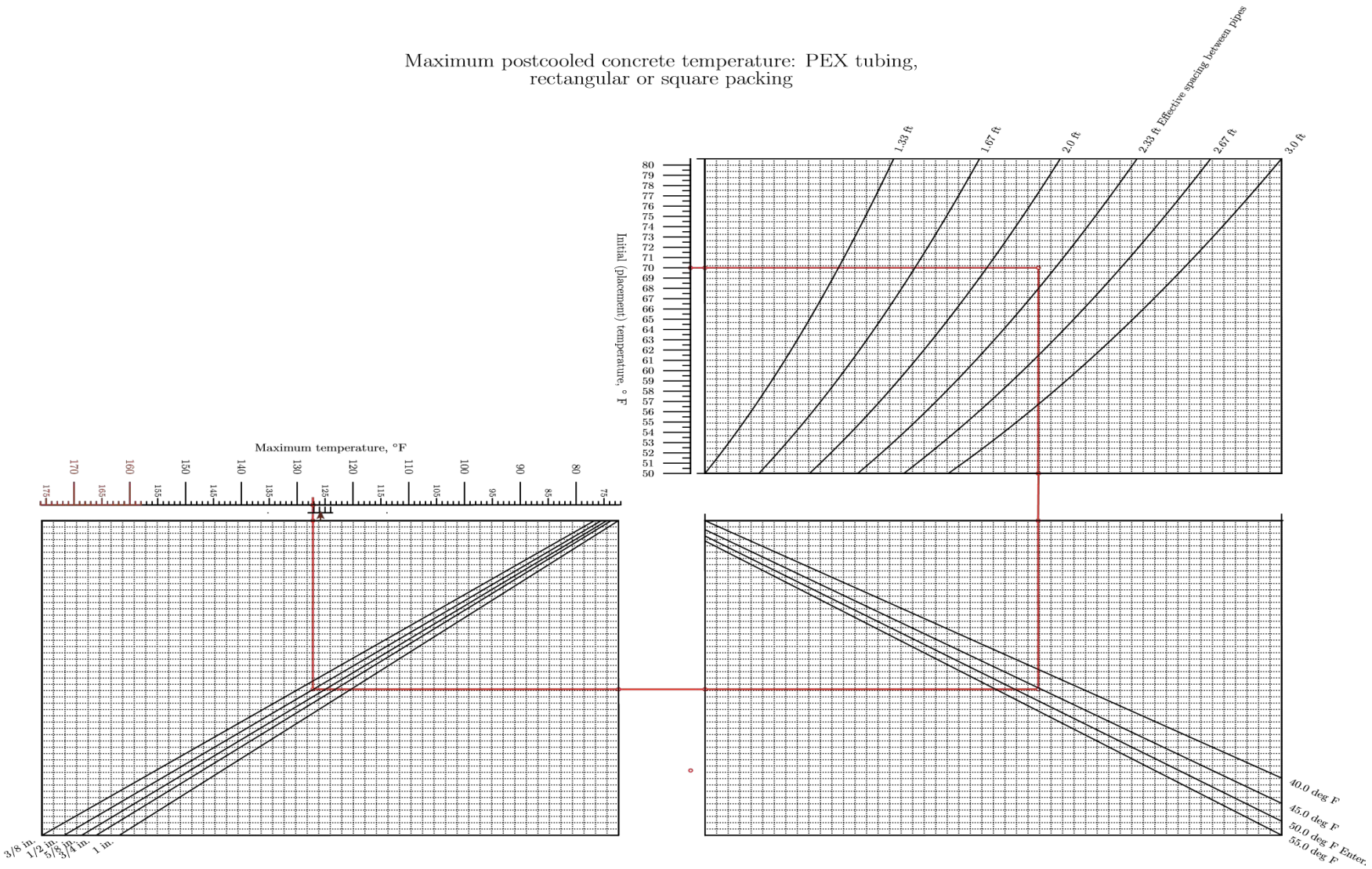

Figure 28. Illustration. Postcooling nomogram, rectangular or square packing, using effective thermal spacing with an in-sample comparison.

As a final example, we make an out-of-sample comparison between a nomogram calculation and the SR-92 abutment wall was postcooled. In this case, conditions include the following:

- Initial temperature of 70.7°F.
- Effective spacing for a 1 ft × 2 ft pipe array being 1.12 ft.
- Chilled water temperature of 45°F.
- ¾-inch PEX tubing.

The maximum monitored temperature at sensor TS6 was 129.6°F. Figure 29 depicts this comparison.

Here the nomogram gives a peak temperature of 123°F, an underestimate of 6.6°F, and an error of just over 5 percent.

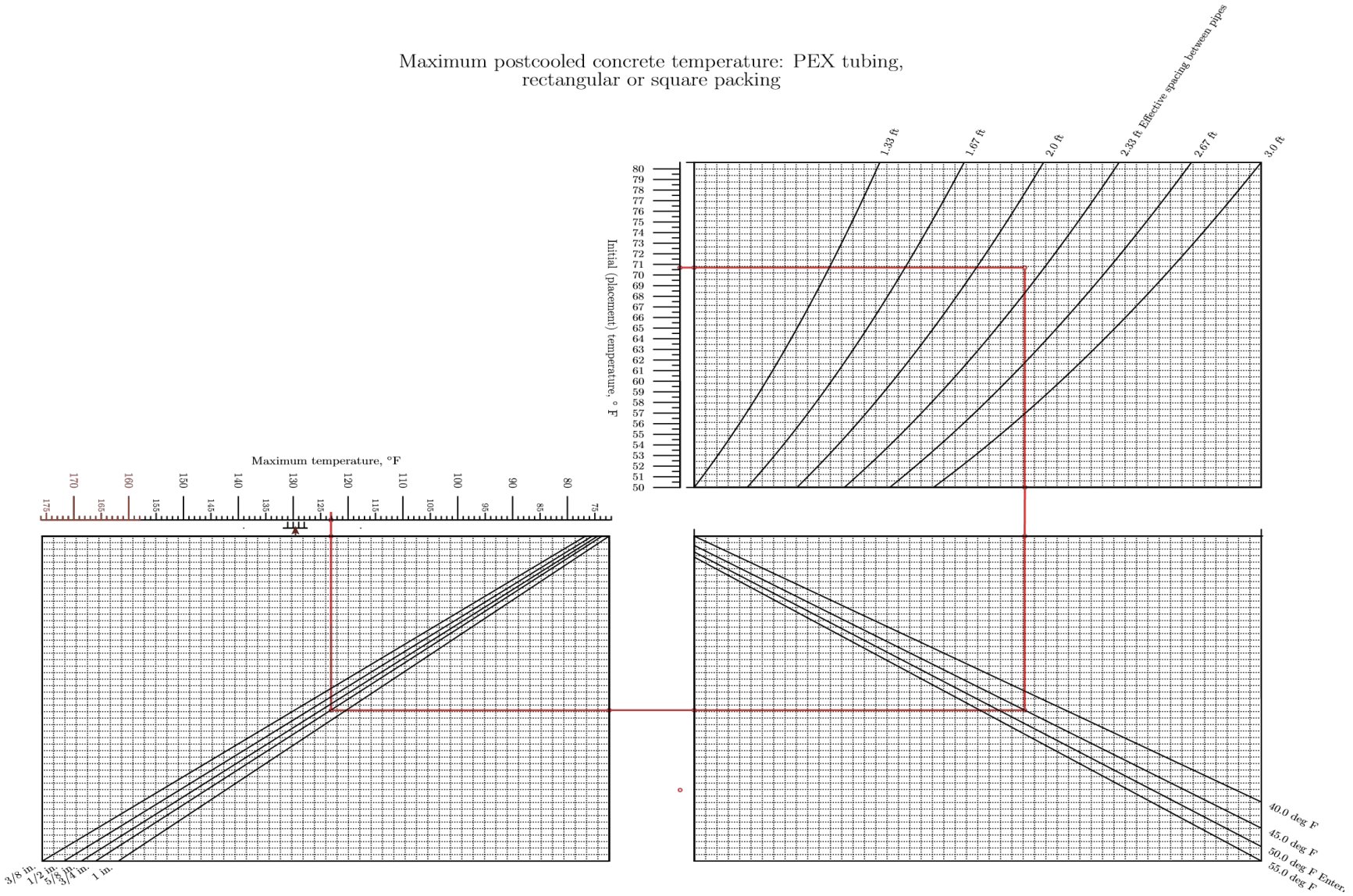

Figure 29. Illustration. Postcooling nomogram, rectangular or square packing, using effective thermal spacing with an out-of-sample comparison: SR-92 abutment.

CONCLUSION

A series of nomograms to aid in planning mass concrete projects have been developed based on first principles and on a suite of simulations. The examples shown should demonstrate not only their use but also their limitations. The creation of these nomograms necessarily requires some simplifying assumptions, and the limitations embodied by those assumptions will be embedded in the resulting nomograms. To reemphasize, one of those limitations is that no attempt was made to account for solar heat transfer, as it was assumed that for mass concrete, maximum temperatures will occur at a depth effectively isolated from solar gains.

Lastly, these nomograms do not substitute for simulations or other analyses to confirm the performance thermal management designs; however, it is our hope that they can aid in the rapid selection of candidate designs while incorporating tradeoffs.

CHAPTER 4. MASS CONCRETE MIX DESIGNS (TASK 3)

INTRODUCTION

The heat diffusion equation including a source term, given in equation 22, is used to model temperatures and heat flows over space and time in concrete structures:

$$\rho C_p \frac{\partial T}{\partial t} = k\nabla^2 T + \frac{dH_{co}}{dt} \quad (22)$$

where, ρ is the density of concrete (kg/m3), k is the thermal conductivity in (W/m-K) and C_p is the specific heat (J/kg-K). To solve for temperature histories using equation 22, it is necessary to quantify the rate of heat release term $\frac{dH_{co}}{dt}$ for a given concrete. $\frac{dH_{co}}{dt}$ is attributed to the hydration reaction of the cementitious paste and its rate of heat release $\frac{dH}{dt}$, which is influenced by the cement content, substitution with supplementary cementitious materials, water/binder (w/b) ratio, and the chemical composition and fineness of the cementitious materials used. $\frac{dH}{dt}$ also increases with increasing placement temperature of the concrete.(38) After obtaining $\frac{dH}{dt}$ of the paste, the $\frac{dH_{co}}{dt}$ term in equation 22 can be calculated by considering the weight fraction of cementitious materials in the concrete. After finding the heat of hydration source term and the necessary information on density, heat capacity, and thermal conductivity of concrete, the internal temperature rise as a function of space and time can be simulated.

Both adiabatic and semi-adiabatic calorimeters find the temperature rise and heat of hydration of concrete $\frac{dH_{co}}{dt}$ under evolving temperatures, similar to mass concrete where temperature continuously changes due to the hydration process and evolving environmental effects. In contrast, isothermal calorimetry is used to measure rate of heat

release of cementitious pastes $\frac{dH}{dt}$, and mortars, under constant temperatures. The rate of heat release can also be referred to as thermal power. Determining the rate of heat release of the cementitious paste $\frac{dH}{dt}$, and subsequently of concrete $\frac{dH_{co}}{dt}$, using isothermal calorimetry is the focus of this chapter. The use of isothermal calorimetry to predict adiabatic temperature rise has been previously reported by Wadso and Xu et al.[39,40] The validity of the approach is examined by applying it to predict internal temperatures of mass concrete elements considering the influence of different mix designs. As validation, the approach illustrated in Figure 30 is applied to two mid-scale concrete mockups and two real-life elements; the SR-92 footing and wall.

Data from isothermal calorimetry can be used to convert from isothermal to either adiabatic or semi-adiabatic values. The methodology outlined here requires performing isothermal calorimetry at different temperatures to find both the rate of heat release and corresponding cumulative heat curves. The approach is based on two main assumptions in the reference.[40] First, it is assumed that at a given time and temperature, the measured rate of heat release is the same regardless of the calorimetry testing method used, i.e., isothermal, adiabatic or semi-adiabatic. The second assumption attributes heat release to the cementitious matrix and considers the effect of other materials in the concrete mix design on cumulative heat negligible. This is important since isothermal calorimetry is most practically performed on cementitious pastes and can be adapted to test mortar samples, although it cannot be done on concrete. One implication is the difference between the rate of heat release of cement pastes tested in the laboratory and that of cements in concrete.

The mixing action in concrete can be mimicked by using a high shear mixer in the laboratory, which leads to an increased rate of heat release compared to a hand mixer.[41]

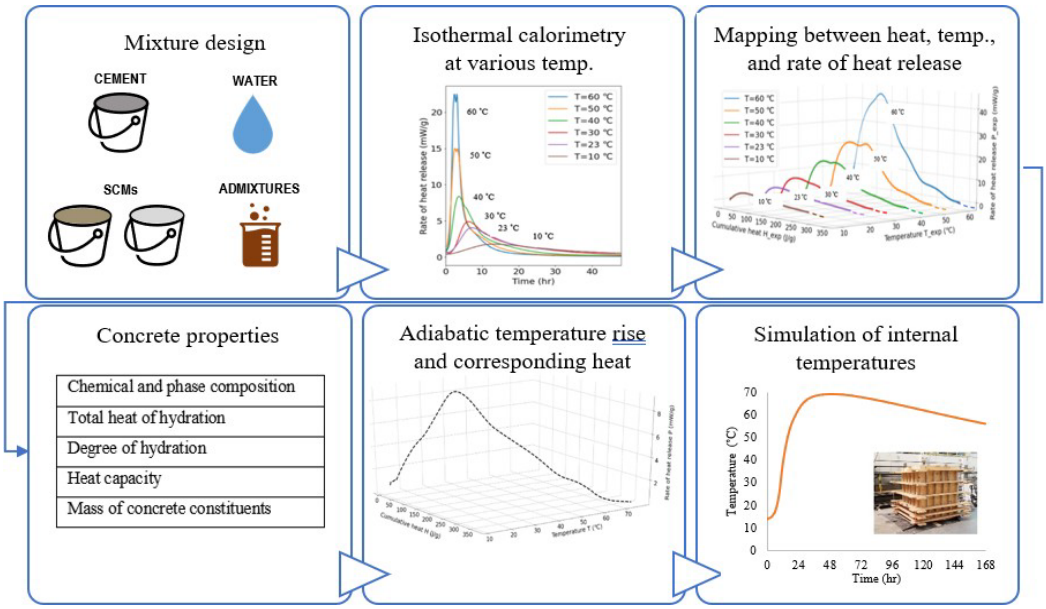

Figure 30. Illustration. Schematic showing the steps involved in using isothermal calorimetry for mass concrete modeling.

Every concrete mix has a unique adiabatic temperature rise, which is found by dividing the concrete's heat release by its heat capacity. In order to calculate how this temperature rise evolves with time, it is necessary to determine how the rate of heat release changes with the changing temperature. The utility of performing isothermal calorimetry at different temperatures is that for any combination of cumulative heat evolved and corresponding temperature, a unique rate of heat release for concrete can be computed by mapping the relationship between experimental power (P), heat (H), and temperature (T) values and interpolating between them as necessary. In other words, it would be possible to 'jump' from one calorimetry curve to the other based on the temperature and heat histories.[39] Moreover, the temperature sensitivity of the rate of heat release is intrinsically considered

by performing the tests at different temperatures. The modeling approach is practical since the isothermal calorimeter allows testing more than one cementitious paste design at the same time, which may include different w/b ratios, SCMs, fillers, and admixtures. The adiabatic temperature rise curves and other thermal histories can also be calculated for any value of the concrete's initial placement temperature without the need for additional tests.

METHODOLOGY

The methodology in this section is in SI units for consistency with the isothermal calorimetry output. Isothermal calorimetry tests are conducted at different temperatures in accordance with ASTM C1679 to obtain the rate of heat release of cement.[42] The test temperatures considered here are 10, 23, 30, 40, 50, and 60°C. The effect of mixing action on the calorimetry results can be considered by using a high-shear mixer in accordance with ASTM C1738/C1738M-19.[43] The mixing action refers to the potential influence of the concrete's higher shearing action on the heat of hydration and subsequently the temperature rise of concrete. However, the more conventional mixing can also be retained since the lower equipment requirements would facilitate this type of testing while minimizing expense.

Following Xu et al.,[40] the isothermal calorimetry data are used to create a relationship between heat, temperature, and power, referred to as $H - T - P$, to estimate adiabatic temperature rise and heat release given a known initial temperature as follows:

1. Isothermal calorimetry provides experimentally measured $H_{exp}/dt = P_{exp}$, in units of power (mW) per unit mass of binder, as a function of time at a given, constant, calorimeter temperature T_{exp}. In order to account for the effect of varying

temperature on $dH_{exp}/dt = P_{exp}$, $dH_{exp}/dt = P_{exp}$ is found, for each calorimeter temperature, as a function of cumulative heat released H_{exp}, as shown in Figure 31. This provides a common value of H to serve as the bridge by which 'jumping' from one calorimetry temperature curve to another is enabled. By definition:

$$H_{exp}(t) = \int_0^t P_{exp}(t)\, dt \tag{23}$$

which is computed numerically using the trapezoidal rule up to time t_n:

$$H_{exp}(t_n) = \int_0^{t_n} P_{exp}(t)\, dt$$

$$\approx \sum_{i=1}^{n} \Delta H_{exp,i} = \frac{1}{2}\sum_{i=1}^{n} (P_{exp,i} + P_{exp,i-1})(t_i - t_{i-1}) \tag{24}$$

where, $P_{exp,i}$ is the experimentally measured thermal power at the i^{th} time t_i. In effect, the time axis is replaced with an H-axis for each experimental run (see Figure 32).

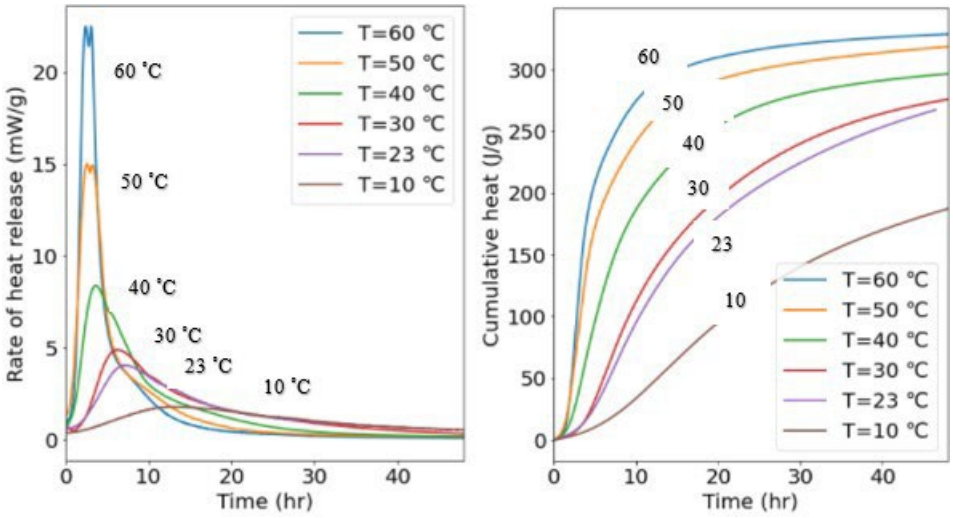

Figure 31. Graphs. Isothermal calorimetry rate of heat release and cumulative heat at different temperatures.

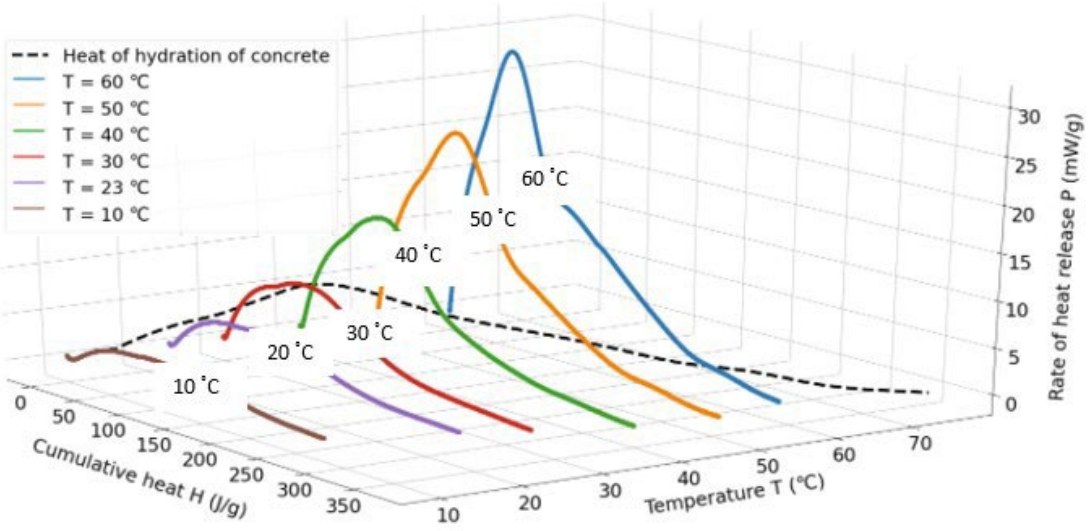

Figure 32. Graphs. Relationship between PP, HH, and TT of cement paste (solid lines) and calculated *in situ* heat of hydration of concrete (dashed line).

Now that the $H - T - P$ relation is obtained at the experimental calorimeter temperatures and discrete values of ΔH_{exp}, interpolation (or extrapolation) can be used to fill in values between these experimental data. Despite discarding an

explicit time axis, time information is still implicitly included via thermal power P. At a given value of H, P increases with increasing T. For any arbitrary increment in thermal energy released ΔH, if the temperature T is known then the corresponding power P is known and can be used to determine the increment of time Δt associated with ΔH at that T. Knowing the specific heat, the increment in adiabatic temperature ΔT_{ad} associated with that ΔH can be determined. Cumulative heat release H, (adiabatic) temperature T_{ad}, and time t can then be updated using ΔH, ΔT_{ad}, and Δt, respectively, with the procedure repeating to advance the adiabatic trajectory in time, storing P and determining the evolution of the degree of hydration α as desired. This summarizes the procedure to follow, given an initial temperature T_0 and initial heat release H_0=0

2. The ultimate heat of hydration HH_{uu} is calculated as follows:

$$H_u = H_{cem} \cdot p_{cem} + 461. p_{SLAG} + 1800. p_{FA,CaO} \tag{25}$$

$$\begin{aligned} H_{cem} = {} & 500 p_{C_3S} + 260 p_{C_2S} + 866 p_{C_3A} \\ & + 420 p_{C_4AF} + 624 p_{SO_3} \\ & + 1186 p_{FreeCaO} + 850 p_{MgO} \end{aligned} \tag{26}$$

A constant value of ΔH is selected (e.g., 1 J/g), and vectors H and α are created, such that:

$$\mathbf{H} = \langle H_0 = 0, H_1 = \Delta H, H_2 = H_1 + \Delta H, \dots, H_{ult} \rangle$$

$$\boldsymbol{\alpha} = \langle 0, \alpha_1 = H_1/H_{ult}, \alpha_2 = H_2/H_{ult}, \dots, \alpha_u \rangle \tag{27}$$

Where, H_{ult} is the ultimate heat of hydration a cementitious mix can attain, and is the product of the total heat of hydration H_u and the ultimate degree of hydration α_u.

3. The initial heat capacity of concrete is calculated using equation 28, which takes into account the contribution of different mix design constituents based on their respective heat capacities, as well as the contribution of the degree of hydration and the temperature of the cement.(44) The solution is an iterative process that starts with an initial temperature T_0 and degree of hydration:

$$c_p(\alpha_i) = \frac{1}{m}\left(m_c.\alpha_i.c_{p(cef)} + m_c(1-\alpha_i)c_{p(c)} + m_a.c_{p(a)} + m_w.c_{p(w)}\right) \quad (28)$$

where, , $c_p(\alpha_i)$ is the specific heat capacity of concrete (J/g °C) as a function of the degree of hydration, m, m_c, m_a, and m_w are the masses (kg) of concrete, cement, aggregate, and water contents, respectively; α_i is the degree of hydration at the i^{th} time; $c_{p(cef)} = 8.4T + 339$ is the fictitious heat capacity of hydrated cement (J/g·°C); T is temperature (°C); and $c_{p(c)}$, $c_{p(a)}$, and $c_{p(w)}$ are specific heat capacities (J/g·°C) of cement, aggregate, and water, respectively.

4. The isothermal calorimetry data obtained are normalized with respect to the mass of the binder. The method assumes that the heat release is wholly attributed to the hydration process of the binder and distributed over the mass of concrete. In order to calculate the adiabatic temperature rise of concrete, the heat release needs to be expressed in terms of joule per gram of concrete, such that:

$$\Delta H_{co} = \frac{\Delta H . m_b}{m_{co}} \qquad (29)$$

where, ΔH is the incremental heat release (J/g) of binder; ΔH_{c0} is the incremental heat release (J/g) of concrete; and m_b and m_{c0} refer to mass of binder and concrete in the mix in grams, respectively.

5. The vector of adiabatic concrete temperatures is computed:

$$\mathbf{T}_{\text{ad}} = \langle T_0, T_1, T_2, \dots, T_m \rangle \qquad (30)$$

where,

$$T_i = T_{i-1} + \Delta T_{ad}$$
$$T_i = T_{i-1} + \frac{\Delta H_{co}}{c_p(\alpha_i)} \qquad (31)$$

and T_0 (°C) is the initial placement temperature and $m = |\mathbf{H}|$ is the number of members of **H**.

6. At each (H_i, T_i), $0 < i \leq m$, the corresponding thermal power P_i is determined using interpolation or extrapolation as necessary, and the vector is assembled:

$$\mathbf{P} = \langle P_0 = 0, P_1, P_2, \dots, P_m \rangle \qquad (32)$$

The adiabatic H − T_{ad} − P relationship for concrete is demonstrated by the black dashed line in Figure 32.

7. The vector of time corresponding to **H**, **α**, $\mathbf{T}_{ad}$, and **P** is calculated:

$$\mathbf{t} = \langle t_0 = 0, t_1, t_2, \dots, t_m \rangle \tag{33}$$

by:

$$t_i = t_{i-1} + \Delta t_i$$
$$t_i = t_{i-1} + \frac{2\Delta H}{P_i - P_{i-1}} \tag{34}$$

for $0 < i \leq m$.

8. These data can be used in simulation software for the initial temperature $\partial\partial_0$ used.

After obtaining the heat of hydration curves for concrete, the finite difference (FD) or finite element (FE) thermal simulations can be supplemented with the heat of hydration curves to find internal temperatures in mass concrete elements. The FD or FE model can be provided with information regarding the geometry of the concrete volume (i.e., uniform and nonuniform), material properties (i.e., mechanical and thermal), thermal boundaries (e.g., insulation, formwork, ambient temperature), and cooling measures. Internal temperature development with time and any point in space is then extracted as an output of the thermal modeling. This allows determining the values for maximum temperature and temperature differential, where they occur in the structure, and the time when they occur. Here, modeling has been conducted using the software "b4cast," a finite element software that simulates temperatures and stresses in concrete structures during hardening.[45]

VALIDATION USING CASE STUDIES

Mid-scale Experiments

Two mid-scale mass concrete mockups were constructed in a laboratory setting to monitor the internal temperature histories. The experimental temperature histories were then compared with results obtained from simulations and heat of hydration curves developed using the isothermal calorimetry method. The concrete blocks have a cross-section of 4 ft × 4 ft and a height of 6 ft. The cementitious mixes of the mid-scale experiments plus nine other mixes were tested using isothermal calorimetry to find adiabatic temperature rise curves.

The first mid-scale experiment was constructed using 100 percent ASTM C150 Type I/II ordinary Portland cement (OPC), referred to as Cement A. The second mid-scale experiment involved a 25 percent replacement of Cement A with ASTM C618 Class F fly ash. The chemical and physical properties of the cementitious materials are summarized in Table 7. The w/b ratios and the quantities of the high-range water-reducing admixture (PCHRWR) and water-reducing and retarding admixture (WRRET) are summarized in Table 8. The coarse aggregates used in the concrete mix designs were #57 and #67, in accordance with ASTM C33, in the first and second mid-scale experiments, respectively, and both were granitic gneiss. Natural sand with a fineness modulus of 2.53 was used for fine aggregate.

Table 7. Chemical and physical properties of cements and SCMs.

	Cement A	Class F Fly Ash
Oxide Analysis (% by mass)		
SiO_2	19.90	48.49
Al_2O_3	4.70	20.43
Fe_2O_3	3.40	15.91
CaO	64.50	6.99
MgO	1.70	1.12
SO_3	3.30	2.21
Na_2O_{eq}	0.48	2.42
Phase Composition (% by mass)		
C_3S	59	–
C_2S	12	–
C_3A	7	–
C_4AF	10	–
Blaine Fineness (kg/m^2)		
	391	–

Table 8. Mix designs of mid-scale experiments.

Material	1st Mockup: Baseline	2nd Mockup: 25% FA	Unit
Cement A	696.6	521.3	lb/yd^3
Class F fly ash	–	173.8	lb/yd^3
Fine aggregate	1254.6	1226	lb/yd^3
Coarse aggregate	1684.8	1701	lb/yd^3
w/b	0.444	0.444	–
PCHRWR	3	3	oz/cwt
WRRET	2.5	–	oz/cwt

The two mockups, which differed in mix designs and cooling measures, have the same cuboidal dimensions. The general layout is shown in Figure 33. Wood formwork was used for both experiments on the side and bottom surfaces. The setup for every surface consisted of two ¾-inch plywood sheets placed 6 inches apart. The outer sheets were supported by additional wood components, as illustrated in Figure 33. The space between the plywood sheets on each surface was filled with expanded polystyrene foam for the purpose of insulation. The top of the cuboids was left uninsulated.

Figure 33. Photo. Mid-scale experiment mockup.

The first mockup involved the use of a baseline concrete produced with cement only (i.e., no SCMs). Further, no active cooling measures were adopted, and the configuration of the insulation promoted essentially one-dimensional heat flow such that the top surface remains cool and the zone near the bottom surface exceeds the temperature limit for delayed ettringite formation. Construction took place during the month of January in Atlanta, Georgia, and the concrete placement temperature was 56°F.

Data collection was conducted using 13 sensors, situated as shown in Figure 34. T1–T5 were Geokon Model 4200L low modulus strain sensors used to capture temperatures as well as strains caused by differential temperatures. The accuracy of the sensors is ±0.5 percent full scale. L1–L4 were Geokon Model 3800 temperature sensors with an accuracy of ±0.5°C, used to assess the efficacy of the insulation scheme. An "ambient" sensor placed outside the formwork and sensors S1–S3 were additional Geokon Model 3800 sensors used to collect ambient and surface temperatures, respectively. Data collection was conducted at a 5-minute interval during the first 14 days, followed by a 15-minute interval for the remainder of the month.

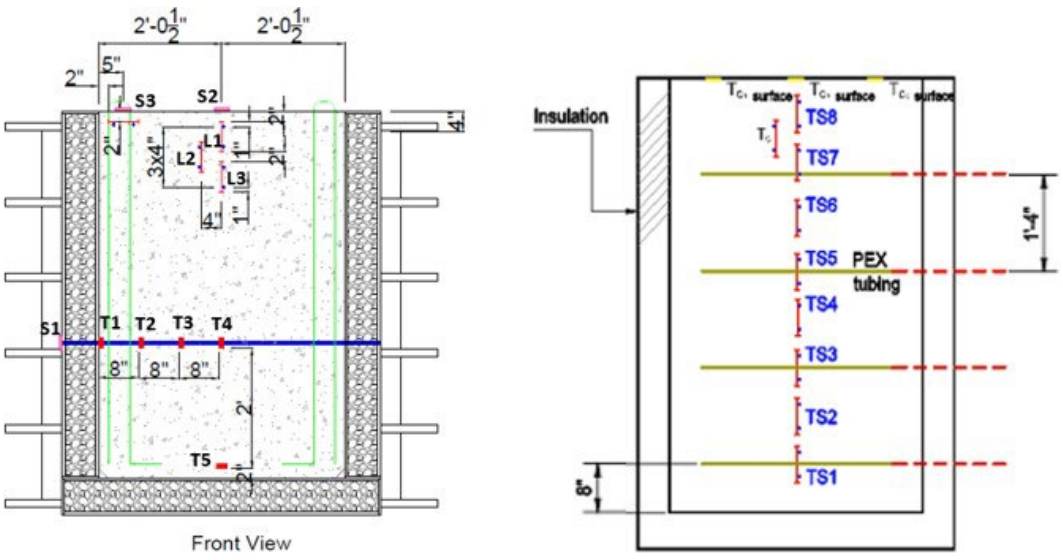

Figure 34. Illustration. Schematic showing sensor location in the middle section of the 1st (left) and 2nd (right) mid-scale experiments.

The second mockup mix design included 25 percent cement replacement by Class F fly ash. Active cooling measures were also considered in this experiment. The embedded cooling pipe system used for this purpose is illustrated in Figure 35. The cooling system involved four open-circuit cooling loops using ⅜-inch PEX cooling pipes, which have an outside diameter of 0.5 inch and an inside diameter of 0.36 inch. Cooling started 14 hours after concrete casting at a water flow of 1.7 gallons per minute (gpm), and lasted for 8 hours. The cooling water temperature inside the pipes was 56°F. Construction of the second mockup took place during the month of May, and the placement temperature was 72°F. Data collection was conducted using a total of eight Geokon Model 3800 temperature sensors and nine Geokon Model 4200L low-modulus strain sensors, situated as shown in Figure 34. Data collection was conducted at a 5-minute interval during the first 14 days, followed by a 15-minute interval for the remainder of the month.

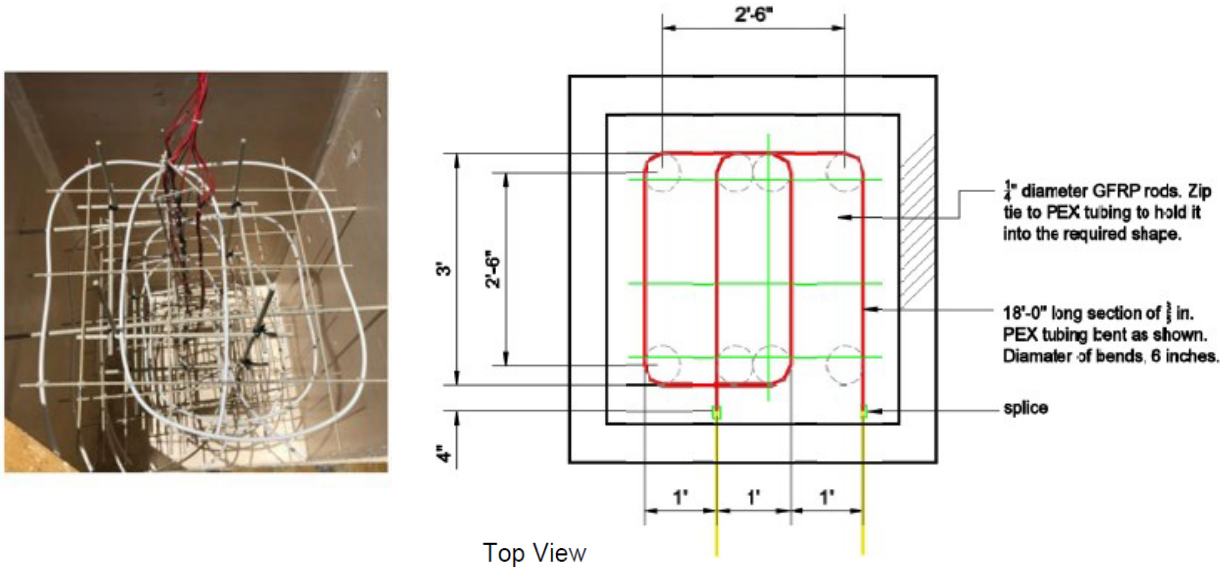

Figure 35. Photo. Illustration. Top view of cooling pipe installation and layout for the 2nd mid-scale experiment.

Comparisons between the simulated and measured maximum internal temperatures and temperature differences for the mid-scale experiments are illustrated in Figure 36 and Figure 37. Figure 36 shows that at the center of the first mockup at sensor location T4, the maximum temperature simulated using the heat of hydration from isothermal calorimetry matches well with the measured value, with an error value of 2.7 percent. The model gives a slightly conservative value with a 12.9 percent error for the maximum temperature difference measured between the point of maximum temperature and the top surface, as shown in Figure 36. Finally, the times when the maximum temperature and maximum temperature difference are reached are captured with 23.4 and 4.7 percent errors, respectively.

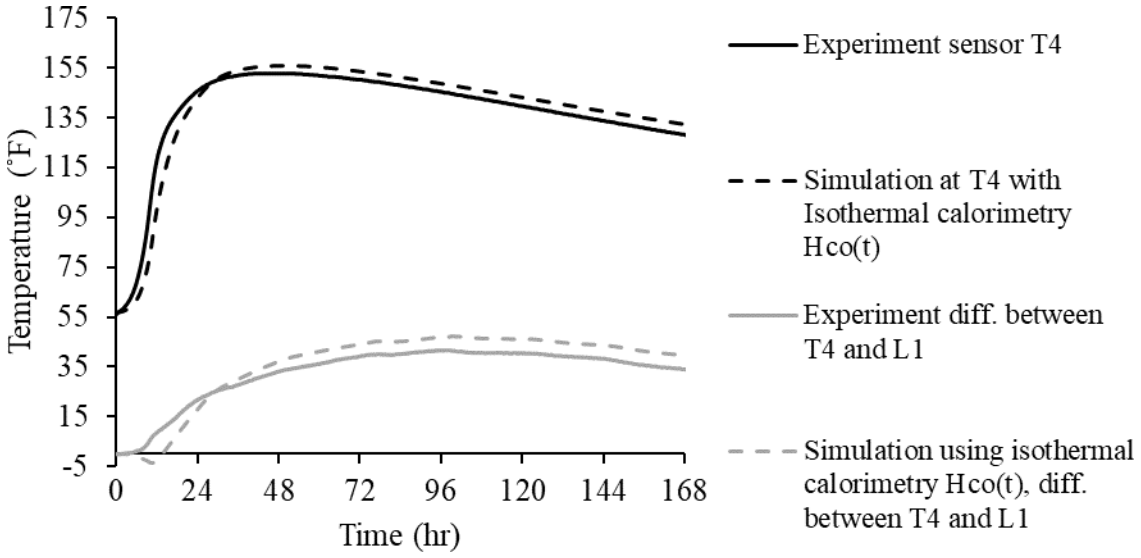

Figure 36. Graphs. Measured vs. modeled internal temperature rise and temperature difference for 1st mockup.

For the actively cooled mockup, the model is able to predict the maximum temperature that the concrete reaches at sensor location TS2 with a small error of −0.5 percent and the time when it occurs with a 4.6 percent error value, as shown in Figure 37. Results for the maximum temperature difference between the point of maximum temperature and the top surface depicted in Figure 37 are also in good agreement with the sensor data, where the maximum value is marginally underpredicted with a −1.1 percent error, and the time at which the maximum value occurs is within 5.8 percent error of the measured value. Results are summarized in Table 9 and Table 10.

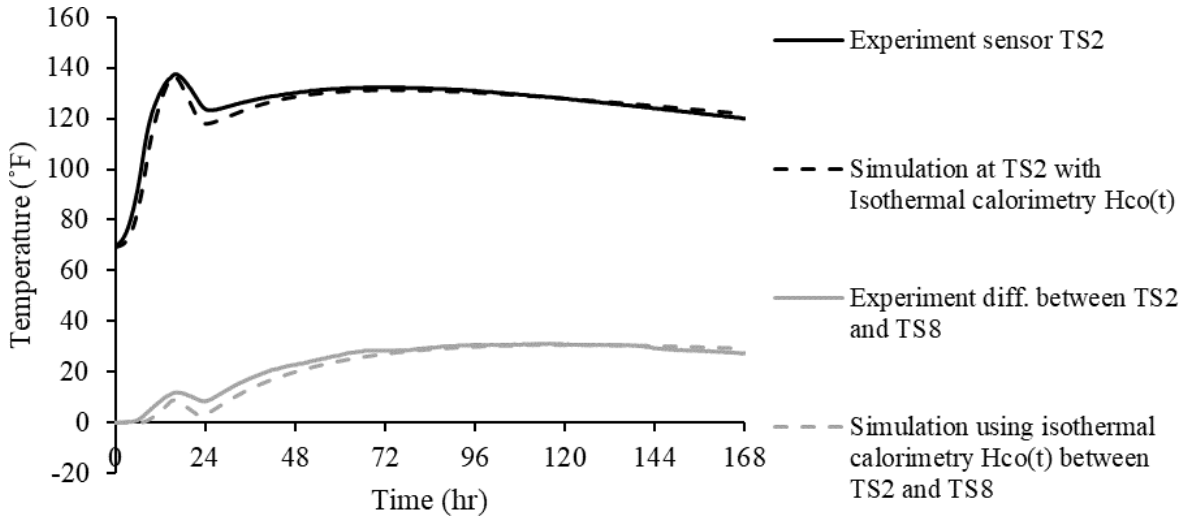

Figure 37. Graphs. Measured vs. modeled maximum internal temperature rise and temperature difference for 2nd mockup.

Table 9. Summary of results for mid-scale experiment's 1st mockup.

Criterion \ Method	Field Measurements	Isothermal Calorimetry Method	Error (%)
Maximum temperature (°C)	152.6	156	2.7
Time to maximum temperature (hr)	40.5	50.0	23.4
Maximum temperature difference (°C)	41.8	47.2	12.9
Time to maximum temperature difference (hr)	94.5	99.0	4.7

Table 10. Summary of results for mid-scale experiment's 2nd mockup.

Criterion \ Method	Field Measurements	Isothermal Calorimetry Method	Error (%)
Maximum temperature (°C)	137.6	136.9	−0.5
Time to maximum temperature (hr)	15.3	16.0	4.6
Maximum temperature difference (°C)	30.9	30.6	−1.1
Time to maximum temperature difference (hr)	114.3	121.0	5.8

CONCLUSION

Isothermal calorimetry can be used to find the adiabatic temperature rise and corresponding rate of heat release for concrete with any material characteristics and initial placement temperatures. The calorimetry needs to be performed at multiple test temperatures to facilitate extracting thermal properties under adiabatic conditions. The methodology intrinsically considers the chemical and physical characteristics of the mix design, necessarily considers the effect of placement and curing temperatures on the rate of heat release, and does not require information on the thermal properties of the calorimeter. Moreover, the calorimeter's ability to test more than one specimen at the same time enables the optimization of mixture selection for mass concrete.

The proposed methodology was validated through the application of two mid-scale concrete experiments, and findings demonstrate that it was successful in predicting internal temperatures for both the uncooled and actively cooled mid-scale experiments.

CHAPTER 5. DEVELOPMENT OF ALTERNATIVE MODELING APPROACHES (TASK 4)

INTRODUCTION

Task 3 in Chapter 4 explained how performing isothermal calorimetry at various temperatures for a cementitious system enables the calculation of the in situ heat of hydration of concrete. Oftentimes, modeling approaches are valuable in cases where experiments are not a feasible option or to narrow down possibilities of cementitious systems. The objective of Task 4 is to propose an alternative modeling approach for the heat of hydration of mass concrete structures using machine learning.

Currently, a need exists for a modeling approach that is capable of accurately predicting the heat of hydration of more complex blended cementitious systems and at various curing temperatures to be used for a mass concrete analysis. There is an increasing interest in the literature to predict the properties of cement and concrete using artificial intelligence machine learning approaches, which would overcome some of the complexities associated with more analytical models. For example, machine learning has been used to predict cement phase mechanical properties and constituent phases from microstructural maps.[46,47] Mechanical and thermal properties of concrete have also been predicted, such as compressive strength, thermal conductivity, the coefficient of thermal expansion, and the adiabatic temperature rise, among many other applications. (See references 48, 49, 50, 51, and 52.) More specific to the heat of hydration, Wang et al. have modeled early age hydration kinetics using a flexible neural tree algorithm for OPC.[53] Similarly, early age hydration (~24 hr) predictions for blended cement containing limestone and metakaolin have been performed by Cook et al. with high fidelity using random forests.[54] The

previous examples demonstrate the promise of using machine learning techniques in predicting materials performance by providing knowledge of the physical and chemical characteristics of cementitious systems.

Prior machine learning efforts to predict heat of hydration have explored OPC systems or blended systems, which are not appropriate for mass concrete, i.e., they contain high heat metakaolin.[53,54] Moreover, the existing models predict hydration kinetics at room temperature only. Here, a Gaussian process regression (GPR) model is proposed to predict cumulative heat of hydration. GPR is a nonparametric regression method, which makes it generalizable even when trained on small datasets. Moreover, GPR is a Bayesian approach and therefore provides an uncertainty estimate for its predictions, which is useful for decision-making processes.[55] Here, the predictions are performed for blended cement containing fly ash, blast furnace slag, limestone, or a combination of the above, at curing temperatures ranging between 5°C and 60°C (41°F and 140°F). A database of mixes with different cementitious physical and chemical characteristics, SCM and filler substitution, water/solids ratio (w/s), and curing temperatures is considered. The proposed model is validated against an instrumented concrete to assess the quality of prediction of maximum temperatures in two mass concrete mid-scale experiments.

EXPERIMENTAL PROGRAM

Data Collection

Isothermal Calorimetry

Isothermal calorimetry tests were conducted in accordance with ASTM C1679 on 23 different OPC and blended OPC-SCM mixes.[56] The materials included in the tests were the following:

- Two different ASTM C150 Type I/II ordinary Portland cement (PC1, PC2).
- ASTM C150 Type II (MH) cement.
- ASTM C618 Class C fly ash (FC).
- ASTM C618 Class F fly ash (FF).
- Class CF fly ash, which is a blend of Class C and Class F fly ashes (FCF).
- ASTM C989 Grade 100 blast furnace slag (BFS).

The w/s ratios ranged between 0.35 and 0.55. The tests were performed at temperatures 10, 23, 30, 40, 50 and 60°C. This results in a total of 133 isothermal calorimetry tests. Table 11 shows a summary of the mix designs of the performed tests.

The tests were performed using an eight-channel (TAM Air) microcalorimeter, which has a precision of ±2 mW and an accuracy greater than 95 percent. The temperature of the specimens was kept as close as possible to the temperature of the calorimeter to avoid condensation. Specimens were heated using an electric oven to maintain the temperature of water and cementitious materials between 30 and 60°C before mixing. An environmental chamber was used to maintain the materials at 10°C.

Table 11. Mixes used in isothermal calorimetry tests.

No.	Cement Type	SCM Type	SCM (mass %)	w/s Ratio	Test Temperature (°C)
1	PC1	–	–	0.35	10,23,30,40,50,60
2	PC1	–	–	0.45	10,23,30,40,50,60
3	PC1	–	–	0.55	10,23,30,40,50,60
4	PC1	FF	20	0.35	10,23,30,40,50,60
5	PC1	FF	40	0.35	10,23,30,40,50,60
6	PC1	FF	20	0.45	10,23,30,40,50,60
7	PC1	FF	40	0.45	10,23,30,40,50,60
8	PC1	FC	40	0.35	10,23,30,40,50*
9	PC1	FC	20	0.45	10,23,30,40,50,60
10	PC1	FC	40	0.45	10,23,30,40,50,60
11	PC1	FCF	20	0.35	10,23,30,40,50,60
12	PC1	FCF	40	0.35	10,23,30,40,50,60
13	PC1	FCF	20	0.45	10,23,30,40,50,60
14	PC1	FCF	40	0.45	10,23,30,40,50,60
15	PC1	BFS	40	0.45	10,23,30,40,50,60
16	PC1	BFS	60	0.45	10,23,30,40,50,60
17	PC2	–	–	0.45	10,23,30,40,50,60
18	PC2	FF	25	0.45	23,50,60*
19	PC2	FF	45	0.45	10,23,30,40,50,60
20	PC2	FF/BFS	25/20	0.45	10,23,30,40,50,60
21	MH	–	–	0.35	10,23,30,40,50,60
22	MH	–	–	0.45	10,23,30,40,50,60
23	MH	–	–	0.55	10,23,30,40,50*

*Test results were either not available or not valid for the full range of temperatures for this mixture design

Data Supplementation

In addition to the performed isothermal calorimetry experiments, the database was supplemented using the heat of hydration histories collected from the literature, as follows:

- 40 heat of hydration curves of OPC and limestone cement pastes with fly ash and slag substitutions at room temperature.(57)
- 29 curves of OPC pastes, limestone cement pastes, and OPC-limestone blends at room temperature.(58)
- 5 tests of an OPC paste at different temperatures.(59)

- A larger dataset of 40 different OPC mixes and blended mixes containing fly ash and blast furnace slag, conducted at 5 different temperatures (5, 15, 23, 38, and 60°C), resulting in a total of 200 observations.[60]

The total number of tests is therefore 407, where 133 are unique cementitious systems and the remaining include variations of the same systems at varying test temperatures.

Machine Learning Approach

Machine learning was utilized to create a model for the prediction of the cumulative heat of hydration. The model is applicable and generalizable to mix designs whose properties are similar to those used for training the model, i.e., those containing ASTM C150 Type I/II cements, ASTM C595 Type IL cements, and the following mineral additives: low-lime fly ash, high-lime fly ash, blast furnace slag, and limestone. Many mix designs were selected based on their common use for mass concrete construction.

The Selection of Features

The output of the machine learning model is the cumulative heat of hydration in Joules per gram of paste solids. The cumulative heat of hydration evolves with time, and therefore its values were retained every ~30 minutes up to 72 hours. This culminates in a total of 106,814 total recorded instances. The predictors, or input features, were selected based on their known effects on the heat of hydration during the first 72 hours. Since the heat of hydration is time-dependent, time (hr) is included as a feature. A change in the curing temperature (or the isothermal temperature at which the tests were conducted) greatly influences the heat of hydration, where a higher curing temperature increases both the rate

of heat release and the ultimate heat value.[61] Finding heat of hydration curves using isothermal calorimetry at different temperatures is necessary for understanding the effect of evolving internal temperatures—expected in massive elements—on the subsequent in situ rate of heat release.[62] Curing temperatures are provided in °C. The water-to-solids ratio and fineness of the cement also accelerate the rate of heat release and increase the cumulative heat of hydration with time.[61] For the cement, the Blaine fineness in m^2/kg was included. The w/s ratio is unitless.

The phase composition of the cement should also be considered. Hydration kinetics in the first few days are mainly driven by the C_3S and C_3A contents. C_3S, for instance, is known to significantly affect the rate at which heat is released.[63] Similarly, the chemical composition of cement was found to affect early age hydration. A higher equivalent alkali content accelerates early age hydration and reduces the induction period,[64] and a higher SO_3 content accelerates the C_3S reaction, which increases the rate of heat release.[65] The phases of the cement and the chemical oxides were included as features as a mass percent of the cement content.

Additional features include the contents and characteristics of the SCMs and the fillers used. Because it is used as a diluent for cement, fly ash retards hydration in both the induction and acceleration periods,[66] and the impact was found to be affected by the fly ash substitution ratio and its lime (CaO) content.[67] The slag content, similarly, retards the rate of heat release and reduces the cumulative heat of hydration.[68] Cement substitution by limestone accelerates cement hydration and increases cumulative heat if the substitution ratio is less than 10 percent.[69] Moreover, a larger specific surface area of the materials results in a short induction period and a higher rate of acceleration.[70] Therefore, seven

features including the percent content of the materials, their specific surface areas in kg/m^2, and the fly ash CaO content were added.

One final feature; a rate factor, is used to depict the temperature sensitivity of the hydration reaction,[71] which is the Arrhenius calculation for every test entry normalized with respect to the Arrhenius calculation at a reference temperature, as follows:

$$Rate\ factor = \frac{\exp\left(-\frac{E_a}{R.T}\right)}{\exp\left(-\frac{E_a}{R.T_{ref}}\right)} \quad (35)$$

where, E_a is the apparent activation energy of the paste in J/mol, R is the gas constant and equals 8.314 J/mol.K, T is the temperature in Kelvin, and T_{ref} is the reference temperature in Kelvin equivalent to 23°C.[72] Equation 35 requires a calculation of the activation energy, which in this study was either found using the single linear approximation method for the group of data where tests at different isothermal temperatures are available or approximated using regression models when the paste was only tested at a single temperature.[73,74]

The dataset is preprocessed to account for any missing values, which were encountered for the equivalent alkali content of three types of cement and the specific surface area of five SCMs. Since values were missing at random, the missing alkali content was replaced using mean imputation, which is a simple technique that assigns to each missing value the average of all available values for a specific feature.[75] For the missing surface area of SCMs, they were assigned the mean of the surface areas of other similar SCMs. The total count of the possible input features is 16. The statistical distribution of features is

summarized in Table 12, where cumulative heat is the output and the remaining are the 16 input features.

Table 12. Summary of statistical distribution of the input and output variables in the entire dataset.

Variable	Unit	Mean	Std	Min	Max
Cumulative heat	J/g	164.25	88.00	0.00	391.08
Time	Hour	34.28	20.53	0.00	72.00
w/s	Unitless	0.43	0.03	0.35	0.55
Temperature	°C	29.15	16.83	5.00	60.00
Blaine	m^2/kg	408.9	54.45	303.00	606.00
C_3S	%	60.63	4.58	49.00	66.54
C_3A	%	6.59	2.51	0.00	9.60
SO_3	%	2.96	0.42	2.38	4.19
Na_2O_{eq}	%	0.59	0.13	0.25	0.85
FA	%	19.07	15.72	0.00	45.00
FA_CaO	%	9.61	10.52	0.00	28.91
FA SSA	m^2/kg	287.59	241.42	0.00	627.00
Slag	%	10.27	20.89	0.00	70.00
Slag SSA	m^2/kg	124.34	238.08	0.00	587.10
Limestone	%	1.35	5.20	0.00	30.00
LS SSA	m^2/kg	36.27	153.30	0.00	917.70
Rate factor	Unitless	1.93	1.82	0.28	8.70

Gaussian Process Regression

GPR is a supervised, nonparametric, probabilistic algorithm that defines a distribution over functions given a certain data. Some of the advantages of GPR include the generalizability of the model for datasets that are not large and the uncertainty estimates it provides for its predictions. The approach is based on defining a prior over functions and translating it into a posterior over functions after observations are introduced into the training process. The fact that the performed predictions are probabilistic is advantageous since GPR is able to compute a confidence interval for the response. The approach is also "kernel-based," which enables it to handle nonlinear data, as is the case with the heat of hydration histories, with great efficiency.

For a training dataset $D = \{x_i, y_i\}, i = 1, \dots, n$, it can be defined that $x \in R^{dxn}$ is the input belonging to a d-dimensional vector space R^{dxn}, and $y \in R^n$ is the output belonging to a one-dimensional vector space R^n; n is the number of data points. Using GPR, the output y can be calculated as:

$$y = f(x) + \varepsilon \tag{36}$$

The error ε follows a normal distribution with a mean value of zero and a variance of σ^2, such that $\varepsilon \sim N(0, \sigma_n^2) \in R^n$. The distribution of y is assumed to be jointly Gaussian in GPR, and has a mean vector $\mu(x)$ and a covariance matrix $\sum(x)$. The covariance matrix is a function of a kernel (κ) that determines the similarity between adjacent observations and the information they provide about each other. It is expected that training observations with similar input vectors will have a similar response. Likewise, similar testing and observed training samples will have similar responses. The covariance matrix takes the following form: $\Sigma_{ij} = \kappa(x_i, x_j)$.

A suitable kernel function needs to be selected to perform the training process. The choice of kernel decides the hyperparameters that one needs to optimize, which is performed using a Bayesian approach, i.e., maximizing the marginal likelihood. A sample kernel is the Matérn 5/2 kernel and is given by:

$$\kappa(x, x') = \sigma_f^2 \left(1 + \sqrt{5}r + \frac{5}{3}r^2\right) \exp\left(-5\sqrt{r}\right)$$

$$r = \frac{\|x - x'\|_2}{l} \tag{37}$$

The hyperparameters in the above equation are σ_f^2, which controls the vertical variation, and the length scale l, which specifies the width of the kernel and implies variation along feature dimensions in the modeled function.[76] Terms x and x' are points in the dataset. It is possible to specify a different length scale for different feature dimensions to determine their relevance by using a product of kernels over the dimensions. For example, the product of Matérn 5/2 kernels is known as Matérn 5/2 ARD, where ARD is the automatic relevance determination.[77] Using this approach, a larger length scale denotes a smaller variation along that dimension and, therefore, a less relevant feature. The hyperparameters and model selection can be further optimized using k-fold cross-validation.[78]

Evaluation of Model Fit

The performance of the model on the testing dataset was quantitatively described using three different statistical measures to allow for a more comprehensive evaluation. The calculations are the coefficient of determination (R^2), the root mean square error (RMSE), and the mean absolute error (MAE). The measures are calculated by comparing predictions (y') and actual measurements (y) through the shown in equation 38 to equation 40, where $\bar{y}$ is the average of the actual measurements in the testing set, and n is the number of observations:

$$R^2 = 1 - \frac{\sum_i (y_i - y'_i)^2}{\sum_i (y_i - \bar{y}_i)^2} \tag{38}$$

$$RMSE = \sqrt{\frac{1}{n}\sum_i |y_i - y'_i|^2} \tag{39}$$

$$MAE = \frac{1}{n}\sum_i |y_i - y'_i| \quad (40)$$

GPR Model

The collected data were randomly divided into training and testing sets with an 80/20 split, where each isothermal calorimetry test was treated as an individual entry. Due to a large number of data, the fit and prediction processes were performed using the subset of dataset (SoD) approximation, where the GPR model is applied to a subset of the entire dataset of size $mm < nn$ to reduce computational complexity.[79] Matérn 5/2 ARD was selected as a suitable kernel function, where separate length scales are used as predictors. k-fold cross-validation with the number of folds taken as 10 was performed during model training to optimize the hyperparameters and avoid overfitting. The model with the least loss value, taken as the mean square error, was adopted for the heat of hydration predictions.

It is also important to understand the stability of the model and how it would be affected by changes in the training and testing datasets. Resampling using the bootstrap method was performed to further assess and validate the performance and robustness of the model.[80] The bootstrap method involves dividing the data into training and testing datasets at random with replacement at a fixed split ratio, and the process is repeated for a determined number of iterations. The performance of the model is evaluated at each iteration. Here, 250 iterations were performed. The performance measures were calculated at every iteration, and their statistical distributions were obtained at the end of the analysis.

RESULTS AND DISCUSSION

GPR was used to predict the cumulative heat of hydration of different cementitious pastes at different isothermal temperatures. A dataset was compiled by performing isothermal calorimetry tests to obtain heat of hydration histories, in addition to histories collected from the literature. The GPR model was trained on a randomly selected testing dataset, and the robustness of the model was evaluated using bootstrapping. The applicability of the model to real-life structural elements was validated by upscaling the predicted heat of hydration curves to find the internal temperatures of two mid-scale experiments. Finally, the use of the uncertainty estimates which the model provides as part of the decision-making process was demonstrated.

Prediction of the Heat of Hydration

The GPR model was trained using the training dataset, and the prediction accuracy was evaluated using the testing dataset. The heat of hydration was predicted over a period of 72 hours, although shorter time periods were also considered based on the experiment details. The hyperparameters of the model were automatically optimized during training with the use of automatic relevance determination. In order to minimize bias in the model and to ensure that the hypermeters were carefully optimized, 10-fold cross-validation was conducted, and the model with the least MSE loss was adopted. Figure 38 illustrates heat of hydration prediction fits and accompanying RMSE for a representative group of cementitious mixes. The predicted heat of hydration matches very well with the observed heat of hydration for all four mixes. All predictions fall within the 95 percent confidence interval limit. The confidence interval is narrowest for the first mix, which was OPC and

cured at 23°C, indicating that the certainty of prediction is higher for this mix. Performance measures for both the testing and training sets are summarized in Table 13.

It can be observed that some of the predictions in Figure 38 are subject to changes in the slope with time, which is not a true attribute of the heat of hydration curves. The GPR algorithm is nonparametric, and therefore, some flexibility in predictions is anticipated. The predictions will be used to find the internal temperatures of mass concrete elements, and the extent to which prediction errors influence the final results will be explored in the following section.

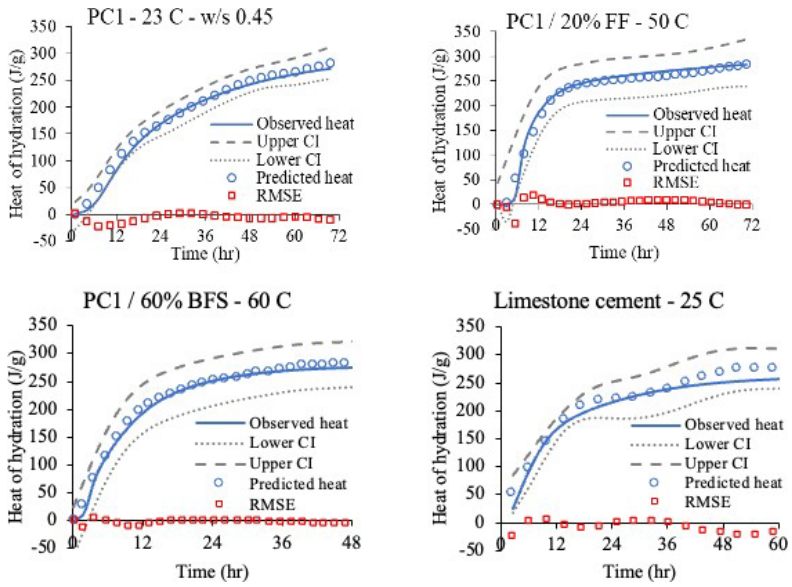

Figure 38. Graphs. Representative examples of the heat of hydration prediction using GPR.

Table 13. Evaluation measures of GPR fit.

Criteria	R^2	RMSE (J/g)	MAE (J/g)
Training	0.99	7.78	3.88
Testing	0.97	13.92	9.05

Table 13 shows that the RMSE error for the training dataset is 7.78 in comparison with 13.92 for the testing dataset. The R^2 of the testing set is 97 percent.

Evaluating Model Stability Using Bootstrapping

The bootstrap method was used to evaluate the stability of the model by resampling the dataset. For the 250 iterations performed, the training and testing datasets were selected at random at an 80/20 split ratio. The statistical distributions of the evaluation metrics R^2, RMSE, and MAE from all iterations are shown in Table 14 for the testing dataset, since its results are more significant to consider when evaluating a model's performance. The average performance criteria values are 0.932, 22.64, and 12.25 for R^2, RMSE, and MAE, respectively. The average values demonstrate that the model is able to predict heat of hydration time histories with good accuracy.

Table 14. Evaluation of model fit after bootstrapping.

Criteria	R^2	RMSE (J/g)	MAE (J/g)
Mean	0.932	22.64	12.25
Standard deviation	0.026	4.69	1.52
Maximum	0.981	34.39	18.92
Minimum	0.848	12.19	8.37

Validation Practice: Adiabatic Temperature-rise in Mass Concrete

This section demonstrates how the developed GPR predictions can be used to find the adiabatic temperature rise in massive concrete structures. Here, the GPR model was used to find the heat of hydration curves required for thermal modeling of two mass concrete mid-scale experiments (i.e., MSE1 and MSE2) constructed using instrumented concretes, presented in Task 3 in Chapter 4. The relevant materials characteristics for the GPR model

are shown in Table 15. Refer to Task 3 for more detailed information about the experiments and monitoring program.

Table 15. Chemical and physical characteristics of the materials of the mid-scale experiment.

	OPC	Class F Fly Ash
Oxide Analysis (mass %)		
MgO	1.70	–
SO_3	3.30	–
Na_2O_{eq}	0.48	–
CaO	–	6.99
Phase Composition (mass %)		
C_3S	59	–
C_2S	12	–
C_3A	7	–
C_4AF	10	–
Fineness (m^2/kg)		
SSA	–	338.9
Blaine	391	–

Isothermal calorimetry tests were conducted for both mixture designs at 23, 30, 40, 50, and 60°C curing temperatures to serve as a comparison to the GPR model predictions. For the machine learning model, two additional data points were created that contain information on the chemical and physical characteristics of the materials in MSE1 and MSE2. The database was collected from isothermal calorimetry tests, and the literature was used for training the model. The model selection was optimized using 10-fold cross-validation, and predictions were performed using the optimized GPR model to find the corresponding cumulative heat of hydration for both cementitious pastes at different isothermal temperatures. Figure 39 shows how the GPR model predictions compare to observed data using isothermal calorimetry. The performance of the model is also summarized in Table 16.

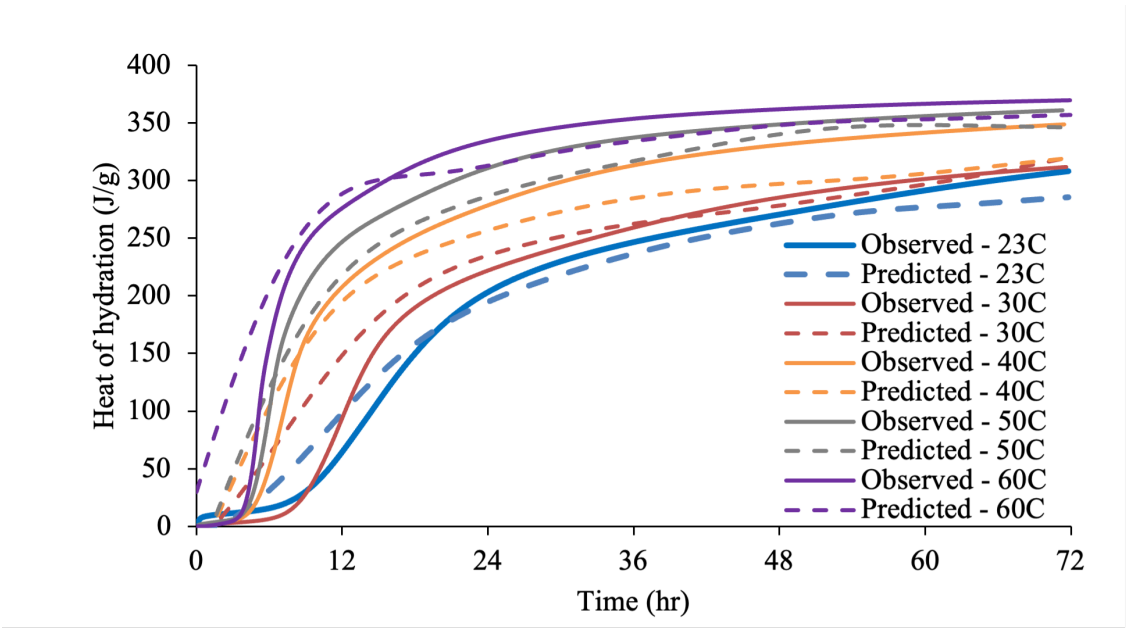

A. MSE1 (top)

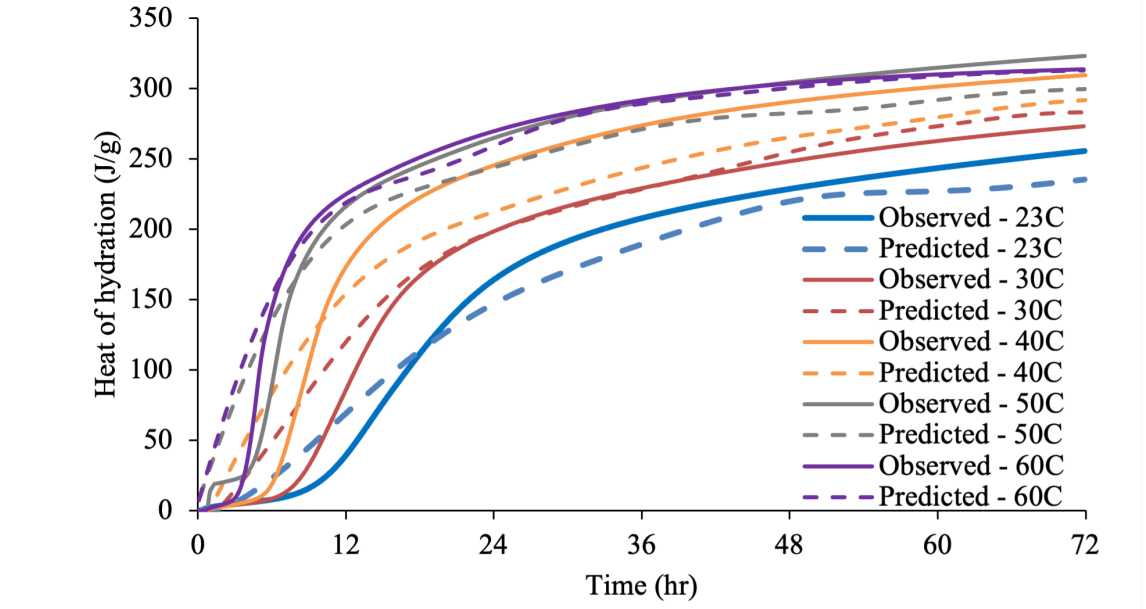

B. MSE2 (bottom)

Figure 39. Graphs. Heat of hydration curves at different temperatures using isothermal calorimetry (measured) vs. GPR model (predicted) for cementitious pastes used in MSE1 (top) and MSE2 (bottom) concretes.

Table 16. Evaluation measures of GPR fit for mid-scale experiments.

Criteria	RMSE	R^2
Training set	12.0	0.98
MSE1	29.9	0.92
MSE2	21.2	0.95

The results show that the model accurately predicts the magnitude of the heat of hydration, whereas it is underperforming when it comes to predicting the early rate of heat release. The mixture designs of both prisms included quantities of ASTM C494 high-range water-reducing admixture (PCHRWR) and ASTM C494 Type B&D low-range water-reducing/retarding admixture (WRRET), which are expected to increase the induction period and the rate of heat release.[81] Since the GPR model does not include features on admixtures, their effect on heat of hydration development was not considered, which is causing the deviation at times earlier than 12 hours.

To predict the internal temperature rise of the concrete prisms, the heat of hydration curves predicted at the various temperatures using GPR was used to find the adiabatic temperature rise of the mixture designs and the corresponding in situ heat of hydration of concrete. The procedure was explained in Task 3 in Chapter 4. The concrete's heat of hydration was then used in the finite element software b4cast to find internal temperatures at all sensor locations. Figure 40 shows the internal temperature histories found using results from the machine learning model and compares it with measured temperatures. The comparison is conducted for sensors T4 and TS2 for MSE1 and MSE2, respectively. Sensor locations are illustrated in Task 3 in Figure 4 and Figure 5.

Figure 39 shows that the predicted heat of hydration curves are able to simulate the internal temperatures of the mid-scale experiment with good accuracy. For MSE1, results tend to be on the conservative side in comparison to the sensor data with a 4.7 percent error in the maximum temperature prediction. In contrast, the maximum temperature for MSE2 is underpredicted, with an error of 5.3 percent. The shape of the temperature rise is well-depicted for both experiments, with some deviation in the early rate of heat release due to the uncaptured effect of admixtures.

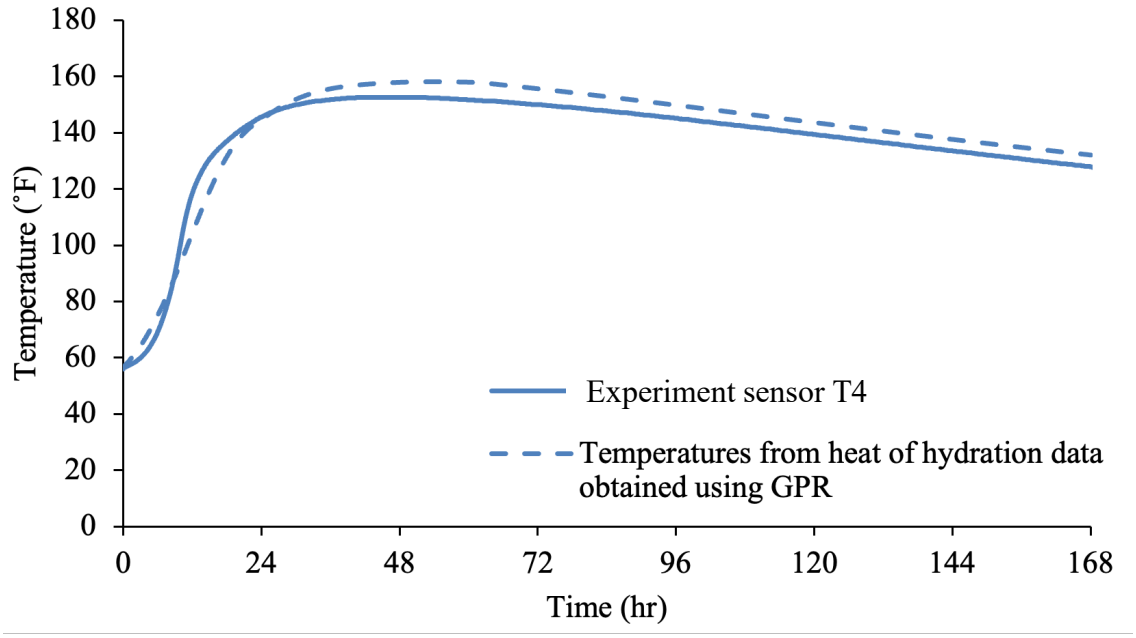

A. MSE1 (top)

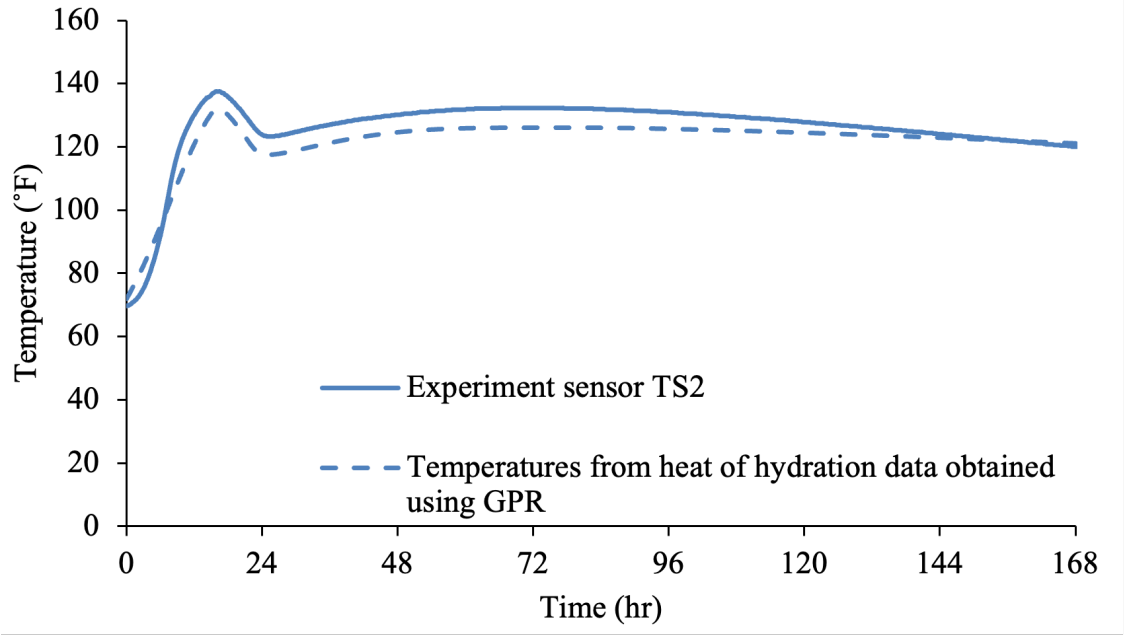

B. MSE2 (bottom)

Figure 40. Graphs. Measured vs. predicted temperature histories of MSE1 (top) and MSE2 (bottom).

CONCLUSION

The heat of hydration of cementitious mixes is necessary to determine many of concrete's mechanical and thermal properties. In mass concrete, the heat of hydration curves at different temperatures are required to find the adiabatic temperature rise of a specific concrete. There is a need in the literature for unified models that are able to capture the heat of hydration of more complex systems, which include supplementary cementitious materials and fillers. For this reason, artificial intelligence machine learning offers a technique that enables the prediction of the heat of hydration by training on information related to the chemical and physical characteristics of the cementitious materials used, curing temperatures, and mix designs. Here, Gaussian process regression was utilized to model and predict heat of hydration for 407 OPC and blended cementitious systems.

The GPR model was used to predict the heat of hydration histories up to 72 hours at different isothermal temperatures. The results have been demonstrated for cementitious mixes containing fly ash, blast furnace slag, and limestone at different replacement ratios and different characteristics. During training, model selection was optimized using 10-fold cross-validation, and model stability was identified using the bootstrap resampling method. The results have proven the ability of the GPR model to perform the predictions with good accuracy. The average R^2 from all the bootstrapping iterations is around 93 percent. The model was also used to predict the heat of hydration curves for a cement belonging to two mid-scale mass concrete experiments, which were subsequently used in finite element modeling to simulate internal concrete temperatures. The ability to use the predictions of the machine learning model and upscale them for application in real-life engineering and decision-making systems has been proven. The model can be expanded to include more

features related to other types of supplementary cementitious materials and possibly admixtures.

CHAPTER 6. ECONOMIC ANALYSIS OF COOLING METHODS (TASK 5)

INTRODUCTION

This chapter focuses on a comprehensive economic analysis of thermal control methods. The research team investigated costs for the thermal control methods through a case study (described in Chapter 2) and pieces of literature. The cost information was then used to generate cost nomograms for the precooling and postcooling methods. The parameters in the cost nomograms were determined from the temperature nomograms (described in Chapter 3). The economic analyses of the cooling methods were applied to the real-world case studies, and the results were compared to alternative designs and thermal management methods, as shown in Figure 41.

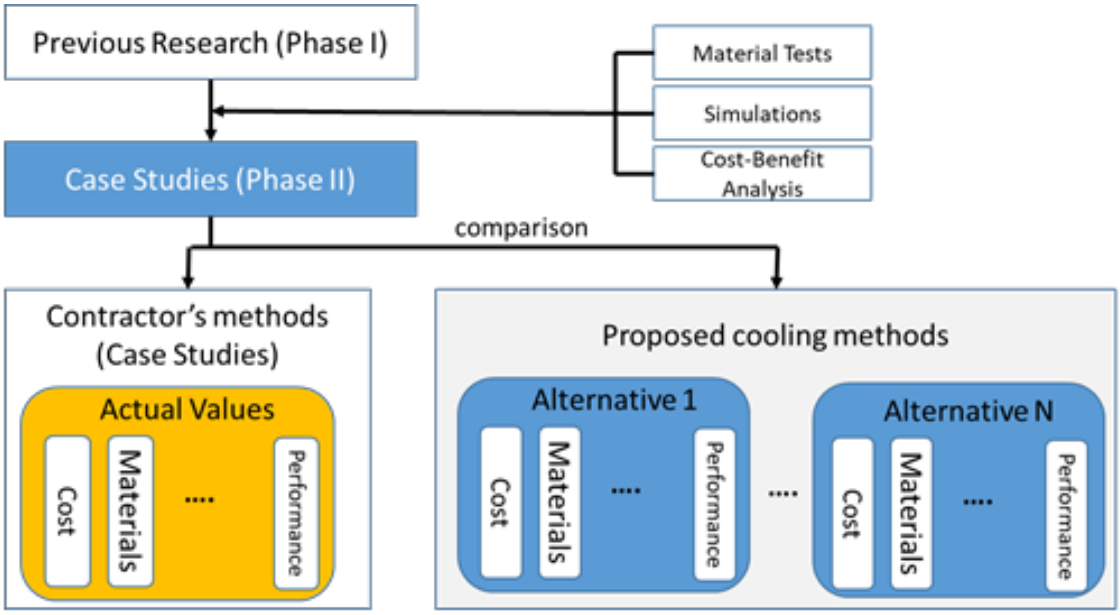

Figure 41. Illustration. Economic analysis on thermal control plans for mass concrete construction.

METHODOLOGY

Precooling Cost Nomogram

Since there is no standardized formula to determine the price of the precooling methods, we generated a cost estimating equation based on references. In 1997, Malisch demonstrated the typical operating prices for concrete precooling as below:[82]

- Chilling mixing water: 4¢ to 12¢ for a 1°F temperature reduction in a cubic yard of concrete.
- LN cooling: 30¢ to 55¢ for a 1°F temperature reduction in a cubic yard of concrete.

The rate of increase in the average cost of electricity per kilowatt in the United States from 1997 to 2020 is about 1.43, according to data published on January 12, 2022, by the U.S. Labor Department's Bureau of Labor Statistics (BLS).[83] In consideration of the increase of average electricity price, the average operating costs for concrete precooling using chilled water and LN are 11¢ and 61¢. Moreover, Malisch also described that if ice replaces only half of the mixing water of one cubic yard of concrete, concrete can be cooled by 12°F (6.6°C) to 20°F (11.1°C).[82] Assuming the water-cement ratio is 0.5, the amount of ice used to lower the concrete temperature by 20 degrees is about 280 pounds. Therefore, the ice-cooling cost for a 1°F temperature reduction in a cubic yard of concrete is about 22¢ if assuming the energy price to generate a pound of ice is about 1.6¢.[84]

Based on the references, we built a closed-form equation to generate a cost nomogram for precooling methods as below:

$$C_{pre,*} = \sigma_* \times \Delta T_* \times cu.\,yd._{concrete} \quad (41)$$

where, $C_{pre,*}$ is a cost for each precooling method, ΔT_* is the temperature reduction, and σ_* is a cost factor for 1°F temperature reduction in a cubic yard of concrete. In this study, the default values of the cost factors are 0.11, 0.22, and 0.66 ($/yd^3) for chilled water, ice, and LN, respectively. Figure 42 is an example of the cost nomogram when using ice and LN to lower the temperature of a 150 cubic yard of concrete by 20°F (16°C).

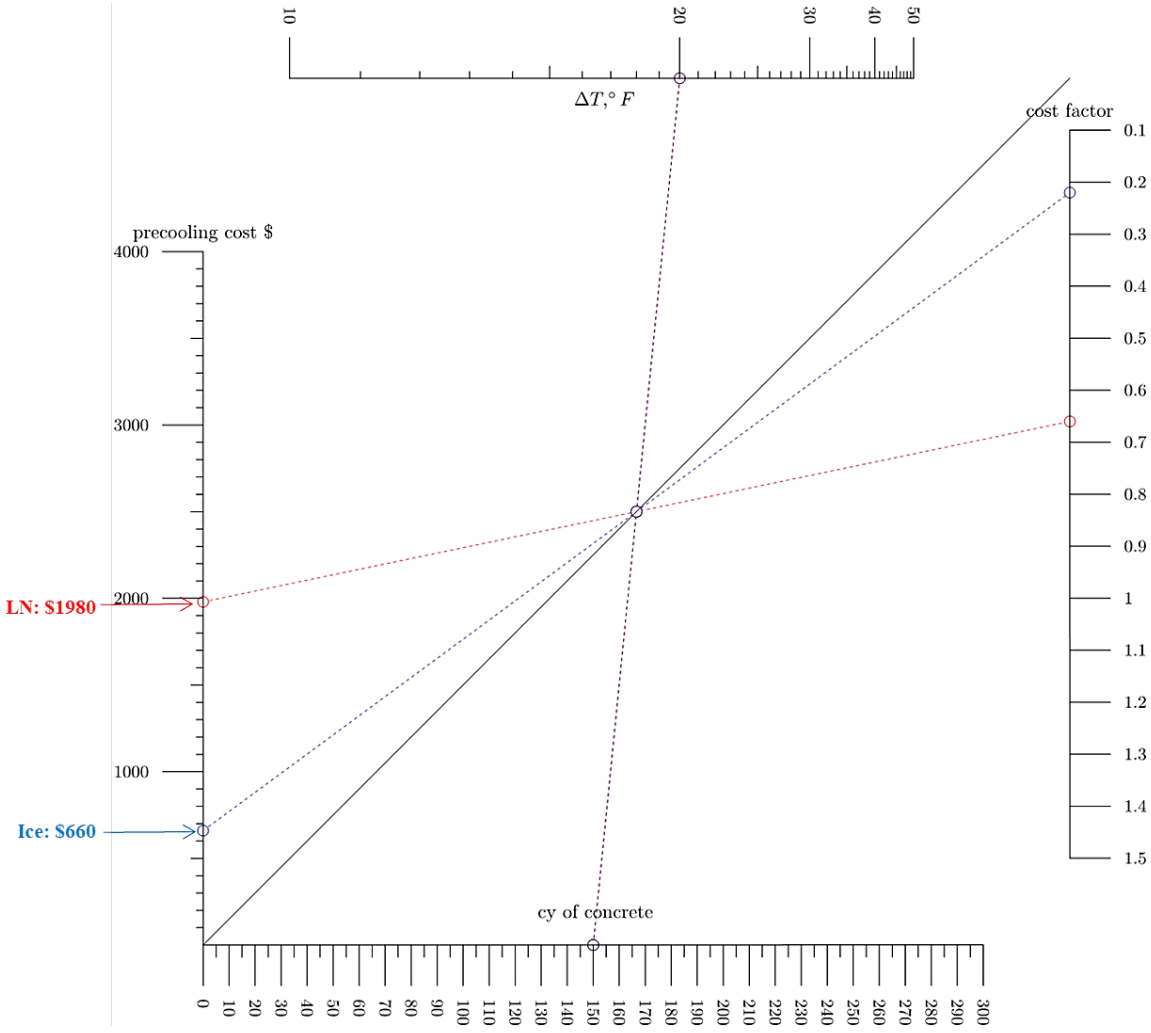

Figure 42. Graph. Cost nomogram for precooling methods.

Since the operating cost can vary depending on the location, the nomogram was designed to change the cost factors. Although this study only considers the operating cost under the presumption that all the facilities for the precooling methods are built, the cooling cost can vary greatly depending on the presence or absence of the facility. For example, the cost factor for ice-cooling can soar up to about $2 if ice makers are not equipped. The total cost of precooling methods is calculated by:

$$C_{pre,total} = C_{pre,w} + C_{pre,ice} + C_{pre,LN} \tag{42}$$

Precooling Cost Nomogram

The postcooling cost nomogram calculates the costs for chiller rental, water tank purchase, manifold fabrication, and piping based on the pipe spacing selected in the postcooling temperature nomogram. In the postcooling system, water is circulated through pipes routed through the hydrating concrete to prevent excessive temperatures. A chiller is often needed to cool the water before it is pumped through the cooling pipes. Therefore, determining the size of the chiller is required to estimate the cost for postcooling methods. The size of the chiller can be determined by the British thermal unit (BTU), which is a measure of the heat content of energy sources. If assuming a safety factor, $\rho\rho$=1.2, chiller tonnage calculation formula is:

$$S_{(ch,ton/hr)} = \mathrm{BTU}/hr \div 10{,}000 \tag{43}$$

and the BTU/*hr* can be calculated by:

$$\mathrm{BTU}/hr = \mathrm{GPM}_{(total)} \times \Delta T_w \times 500 \quad (44)$$

where, $\mathrm{GPM}_{(total)}$ is the total water flow rate (gal/min), and $\Delta\partial\partial_{ww}$ is the temperature difference between inlet water and chilled water in degrees Fahrenheit. A rule of thumb for ΔT_w is that if the flow rate of the water must be sufficiently high, the water does not heat by more than 2 to 3°F as it flows through the cooling pipes. Additionally, our 1,650 simulations in different diameters and lengths of pipe, water flow rates, concrete temperatures, and inlet water temperatures showed that the temperature rise of the water was less than 2°F in most cases when using maximum flow rate, as shown in Figure 43.

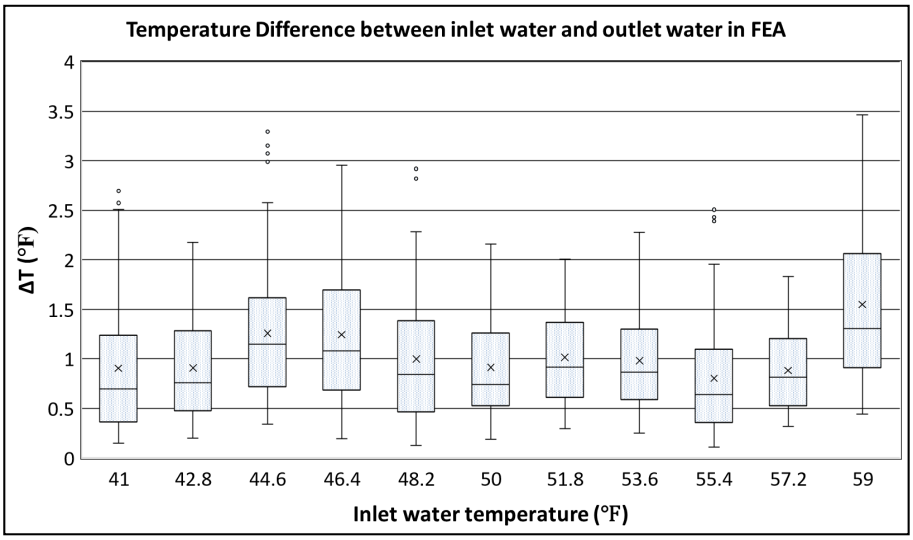

Figure 43. Graph. The water temperature rises during passing through the cooling system.

In fact, most mass concrete construction sites require the maximum GPM to circulate the chilled water from the tank on the ground to the highest portion of the concrete placement/cooling pipe system and back to the tank. In this study, therefore, the maximum

temperature difference was fixed at 2°F. Table 17 shows the required flow rate (gpm) of one PEX tube in different tubing sizes.[85]

Table 17. Required GPM of PEX tubes in different tubing sizes.

Tubing Size (in.)	Minimum Flow Rate (gpm)	Maximum Flow Rate (gpm)
⅜	0.6	1.3
½	1.2	2.3
⅝	1.7	3.3
¾	2.3	4.6
1	3.8	7.5

In this way, the chiller size can be expressed as a function of the number of PEX tubes. The number of PEX tubes can be calculated as a surface area over a square of pipe spacing ($\frac{A}{d^2}$).

$$S_{(ch,ton)} = 0.10\left(\frac{A}{d^2} \times \mathrm{GPM}_{(PEX)}\right) \quad (45)$$

Similarly, a water tank to supply chilled water continuously is required for the postcooling system. The required size of the water tank $S_{(t,ton)}$ is also estimated with total GPM. If the safety factor is 1.2, the water tank tonnage calculation formula is:

$$S_{(t,ton)} = 1.2\left(\mathrm{GPM}_{(total)} \times t_{cir} \times 0.0038\right) \quad (46)$$

where, t_{cir} is the time to circulate the cooling system (assumed as 5 min). The water tank tonnage calculation can be represented with the function of the number of PEX tubes as below:

$$S_{(t,ton)} = 0.0228\left(\frac{A}{d^2} \times \mathrm{GPM}_{(PEX)}\right) \quad (47)$$

Unlike the chiller and water tank, the costs for manifold fabrication and piping only depend on the number of PEX tubes. An equation to estimate the itemized prices is represented as a function of the number of PEX tubes as below:

$$C_{post.*} = \alpha_* \frac{A}{d^2} + \beta_* \quad (48)$$

where, $C_{post.*}$ is the itemized costs for the postcooling system, and α_* is the cost factor for each item, and β_* is the constant value of the linear regression model for the cost of each item. The default cost factors for piping and manifold fabrication were determined by the actual cost information obtained from contractors in Georgia, USA. Based on the equipment tonnage functions and references, the cost factor α and β of each item in Georgia can be calculated as below:

- (Chiller rental) $\alpha_{ch} = 0.10 \cdot \gamma_{ch} \cdot \mathrm{GPM}_{PEX}$ and β_{ch}= 3182
- (Water tank) $\alpha_t = 0.0228 \cdot \gamma_t \cdot \mathrm{GPM}_{PEX}$ and β_{ch} = 306
- (Manifold fabrication) $\alpha_{mf} = 180$ and $\beta_{mf} = 0$
- (Piping) $\alpha_p = 200$ and $\beta_{mf} = 0$

With these cost factors and equations, we generated a postcooling cost nomogram, as shown in Figure 44.

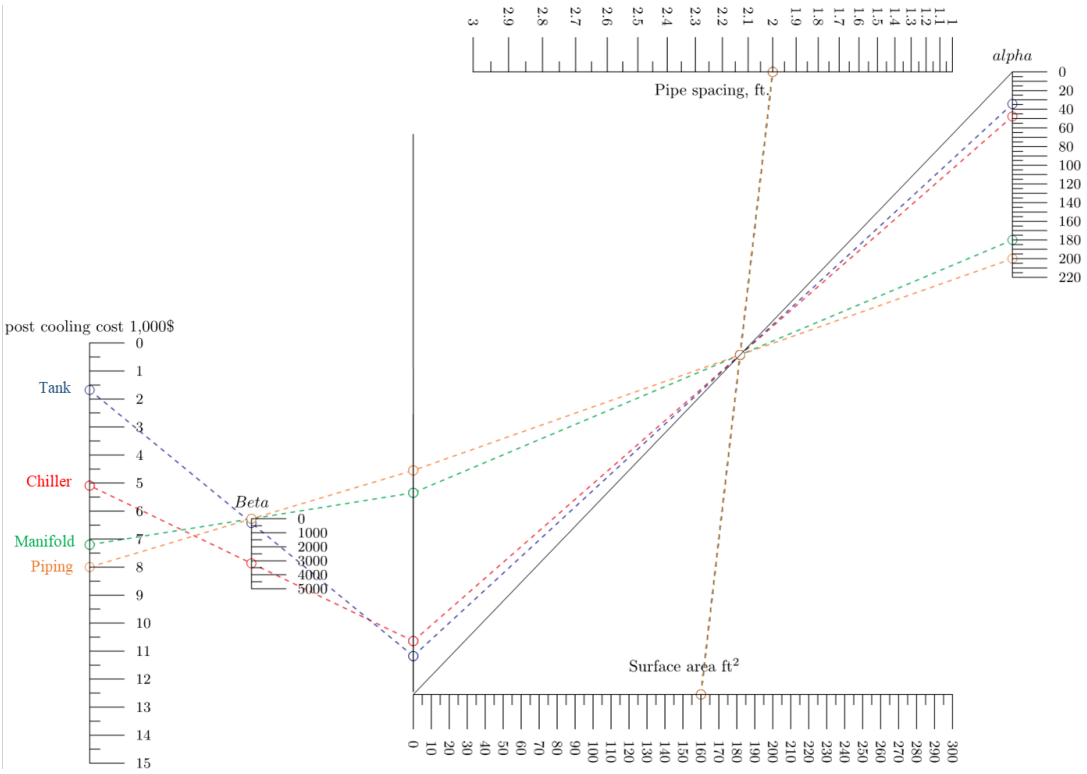

Figure 44. Graph. Example postcooling cost nomogram in the case of 160 ft² of surface area when pipe spacing is 2 ft.

ECONOMIC ANALYSIS OF REAL-WORLD CASE STUDIES

To validate the cost nomograms, we conducted a case study at an active bridge construction project, Norfolk Southern Railway over SR-92, Douglas County, Georgia. The detailed description of the case study is demonstrated in Chapter 2. The contractors employed active thermal control plans, including precooling and pipe postcooling methods. LN was used for the precooling to lower the placement temperature to 70°F. In addition, they also installed PEX pipes into the abutment to operate postcooling and employed blanket insulation to make the temperature difference less than 35°F.

To estimate the cost for precooling methods used in the SR-92 project, we generated a precooling cost nomogram, as shown in Figure 45. In the SR-92 bridge abutment

construction, the temperature of the fresh concrete was dropped from 85°F to 70°F using ice batch and LN. As shown in Figure 45, the total cost for the temperature reduction in the SR-92 case is about $1,200 on the assumption that the temperatures lowered through LN and ICE are equal to 7.5 degrees each. Since this cost nomogram only considers the operating price, the actual retail price paid by the contractors can be different.

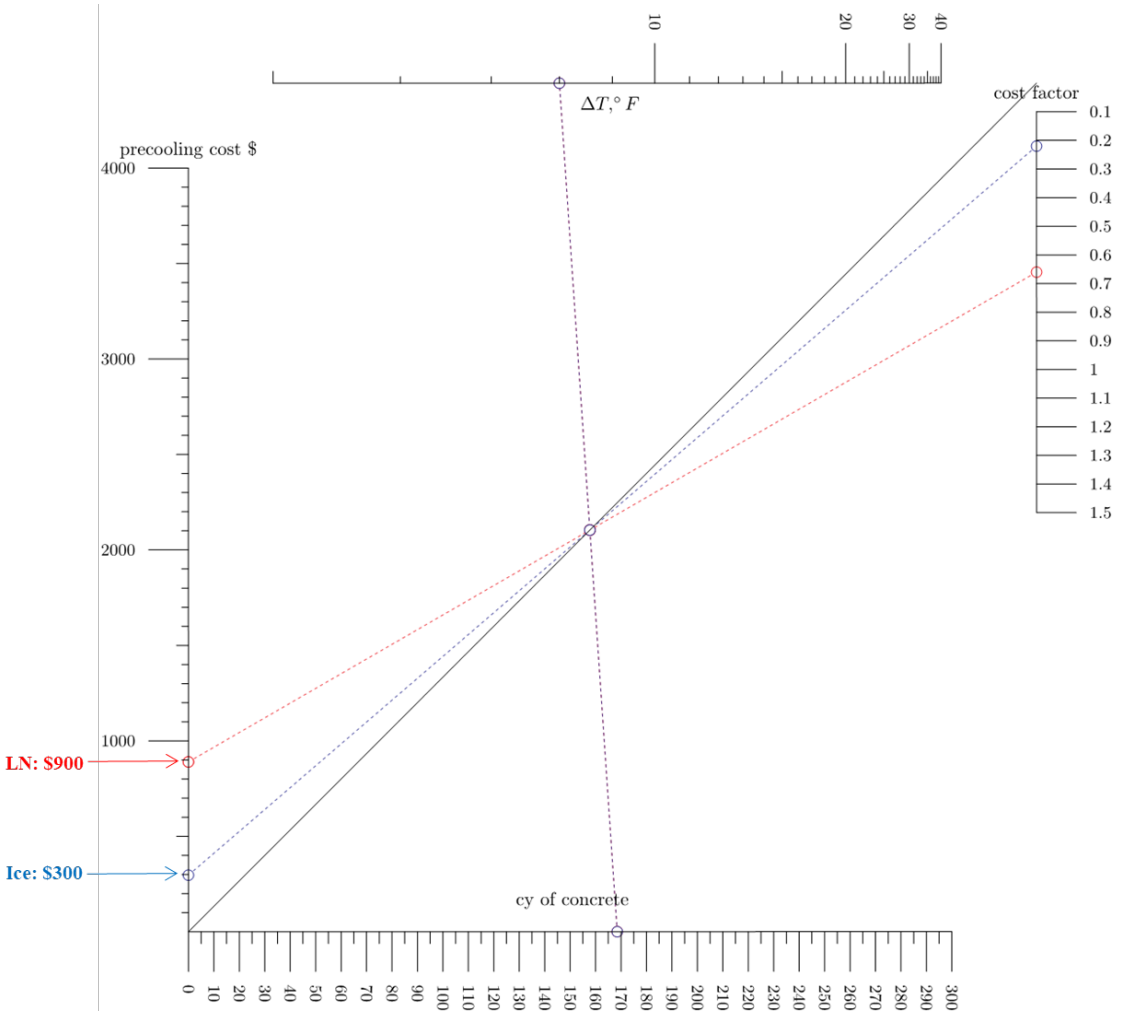

Figure 45. Graph. The cost nomogram for precooling methods in the SR-92 case.

The cost for postcooling methods used in the case study is calculated by the postcooling cost nomogram. Figure 46 describes the cost of postcooling methods. In this case study,

the concrete placement at the abutment was cooled by chilled water pipes. The surface area of the abutment was about 123 ft^2, and the length of the pipe spacing was 1.5 ft. The cost parameters are calculated from actual prices of chiller rental for a month, water tank, manifold fabrication, and piping in Georgia. The itemized costs calculated from the postcooling cost nomogram are described in this nomogram with color codes. We identified that if the pipe spacing is increased to 2 ft, the cost was reduced to almost one quarter.

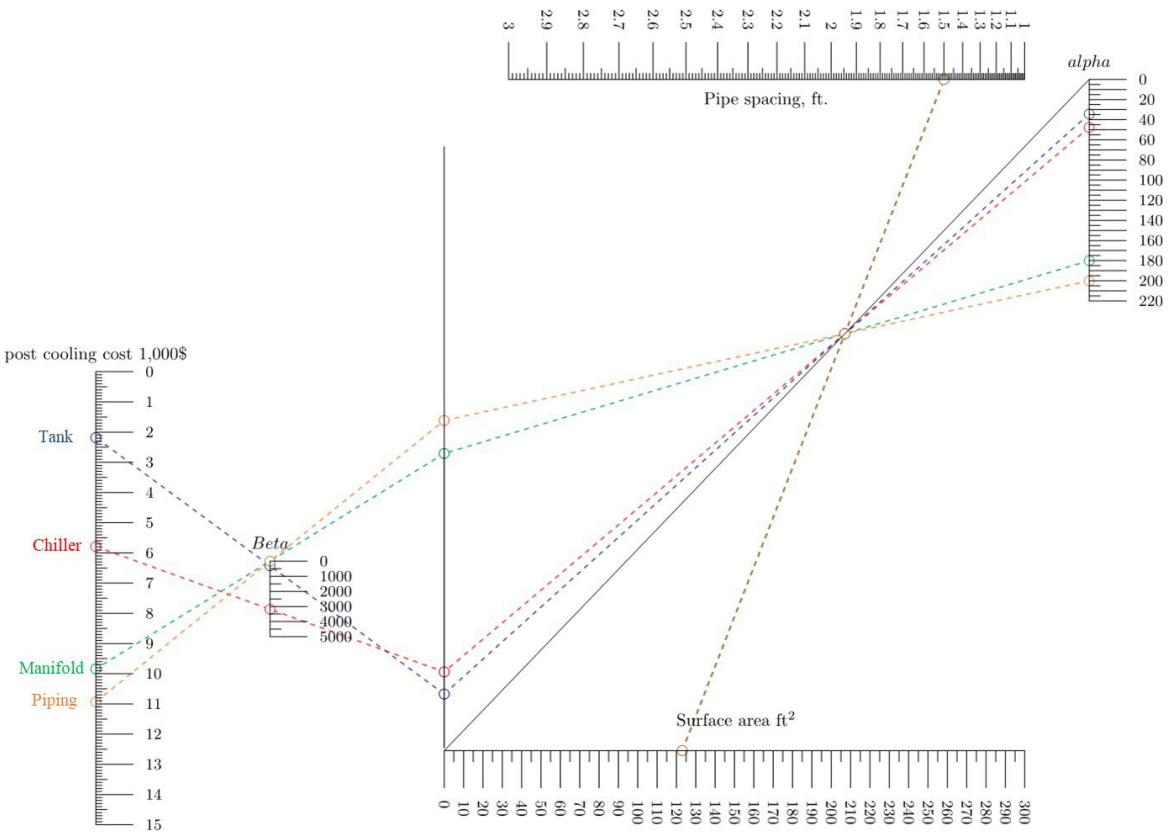

Figure 46. Graph. Cost nomogram for postcooling in case of SR-92.

Our temperature nomograms suggested several alternatives that make the maximum temperature satisfy the temperature limits, and the cost nomograms estimated the total cost of the selected thermal control methods. Table 18 shows the comparison of the total cost

of the different cooling scenarios that can be chosen in the SR-92 bridge construction project. Note that the actual cost paid by contractors is unknown. The estimated costs are calculated by several equations or references demonstrated in this chapter. Although our framework suggested several alternatives, the contractors may make different choices, considering thermal control duration, constructability, feasibility, or safety.

Table 18. Comparison of the total cost of different cooling scenarios.

	Maximum Temperature	Estimated Cost	Details
Precooling only	155°F (68°C)	$3,000	Ice + LN cooling
Precooling (15°F) + Postcooling	148°F (64°C)	$11,100	Ice + LN cooling Pipe cooling (3-ft spacing)
Actual use in SR-92	127.5°F (53°C)	$20,095	Ice + LN cooling Pipe cooling (2-ft spacing)

CHAPTER 7. DEVELOPMENT OF THE BEST PRACTICE GUIDELINE AND TOOL (TASK 6)

INTRODUCTION

In this chapter, we include and integrate outcomes from Tasks 1 to 5 to provide the best practices or tools for: (1) mix design selection, and (2) active thermal control plan selection. The best practices and tools for mix-design selection are developed with isothermal calorimetry demonstrated in Chapter 4. Ways of managing mass concrete with nomograms are also presented in this chapter. The overall process of mass concrete thermal control selection is described in Figure 47.

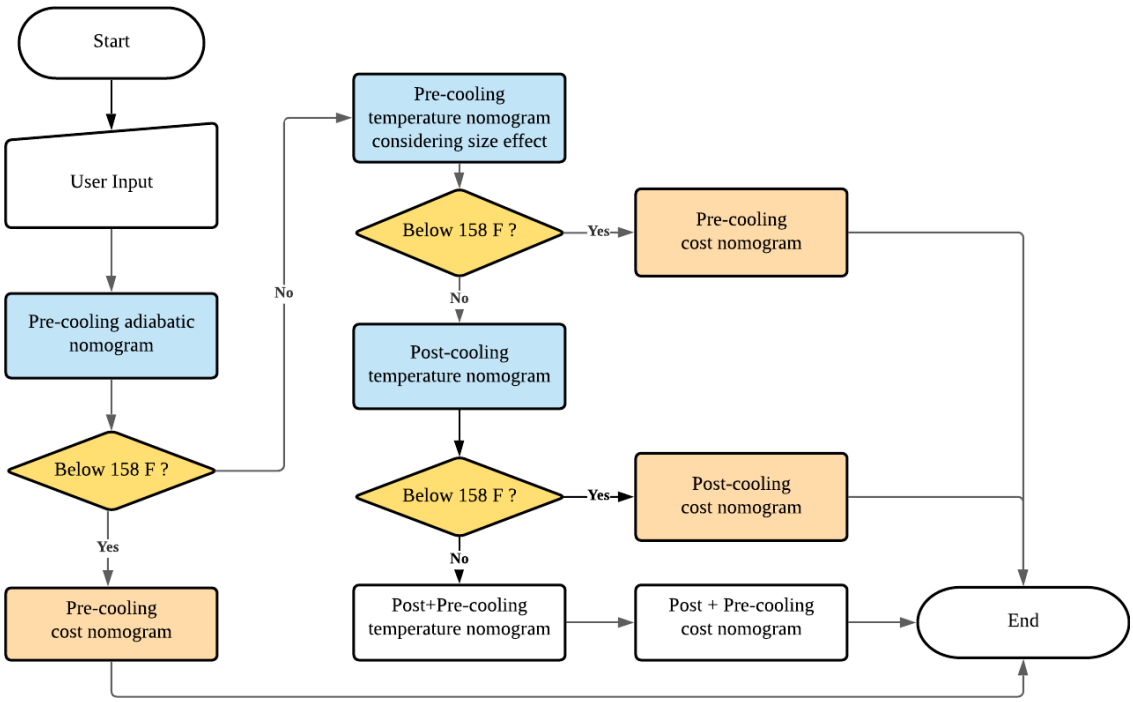

Figure 47. Illustration. Overall process of thermal control method selection.

BEST PRACTICES AND TOOLS FOR MIX-DESIGN SELECTION

It has been demonstrated in Task 3 (see Chapter 4) that isothermal calorimetry can be used to find the adiabatic temperature rise and corresponding rate of heat release for concrete with any materials characteristics and initial placement temperatures. The calorimetry needs to be performed at multiple test temperatures to facilitate extracting thermal properties under adiabatic conditions. The methodology intrinsically considers the chemical and physical characteristics of the mix design, necessarily considers the effect of placement and curing temperatures on the rate of heat release, and does not require information on the thermal properties of the calorimeter. Moreover, the calorimeter's ability to test more than one specimen at the same time enables the optimization of mixture selection for mass concrete. Here, the validity of the proposed methodology is confirmed through the application on two real structures of varying cooling measures and mix designs, and the method is proposed as a best practice for mass concrete thermal modeling.

SR-92 Project

Real-time monitoring of thermal control management practices and temperature rise of two structural elements has been conducted as described in Chapter 2. The selected project for this purpose constitutes the widening and relocation of SR-92 in the city of Douglasville, Georgia, USA. The monitored structural elements include an abutment wall and its foundation. ASTM C150 Type I/II cement was used, whose properties are presented in Table 19. The concrete mixture designs of both structures are shown in Table 20.

Table 19. Chemical composition of Type I/II cement mixes used in SR-92 structures.

Oxide Analysis (%)	Abutment Wall (%)	Footing (%)
SiO_2	20.6	20.5
Al_2O_3	4.78	4.63
Fe_2O_3	2.82	2.81
CaO	64.18	64.0
MgO	1.86	2.27
SO_3	2.79	2.80
Na_2O_{eq}	0.56	0.56
Phase Composition (%)		
C_3S	60.1	60.6
C_2S	13.3	12.8
C_3A	7.8	7.50
C_4AF	8.5	8.50
Blaine fineness (m^2/kg)		
	411	414

Table 20. Mixture design of SR-92 structural elements.

Material	Abutment Wall	Footing	Unit
Cement	670	670	lb/yd^3
Fine aggregate	1103	1103	lb/yd^3
Coarse aggregate	1772	1772	lb/yd^3
Water	37	37	lb/yd^3
AEA	2.75	4.5	oz/cwt
LRWR	6	3.75	oz/cwt
PCHRWR	1	1	oz/cwt

AEA: Air entraining admixture
LRWR: Low-range water reducer
PCHRWR: Polycarboxylate-based high-range water reducer

Footing

Real-life monitoring of the abutment wall's footing was undertaken. The footing has a length of 18.18 m (60 ft) with a construction joint placed at 11.27 m (37 ft), a width of 7.47 m (24 ft 6 inch), and a thickness of 1.37 m (4.5 ft). Therefore, it is not considered massive in the state of Georgia; refer to Figure 51 for a cross section. The cement chemical properties and concrete mix design of the footing are shown in Table 19 and Table 20, respectively. The footing was built on a concrete slab with a varying thickness to fill the

excavated ground, where the thickness was 1.14 m (3 ft 9 inch) in the center and 0.15 m (6 inch) near the sides. The subsurface of the structure consists mainly of granite rocks. Construction took place during August when the average daily ambient temperature was 27.2°C (81°F). The formwork consisted of 19 mm (¾-inch) plywood. No insulation was used during construction, and no cooling measures were adopted.

To find the heat generation curves for the cementitious paste used in the footing, calorimetry tests were conducted for each paste at the following temperatures: 10°C, 23°C, 30°C, 40°C, 50°C and 60°C, using a water/cement ratio of 0.45. All other b4cast analysis parameters for the footing are summarized in Table 21.

Table 21. b4cast thermal analysis input variables for SR-92 footing.

Parameter	Input Value	Parameter	Input Value
Volume		**Environmental Factors**	
Initial temperature	21.3°C (70.3°F)	Ambient temperature	TS11 sensor
Time between batching and pouring	1 hour	Wind speed	3.6 m/s (8 mph)
Material		**Shields**	
Activation energy	37433 J/mol	Plywood thickness	19 mm (¾ in.)
Density	2286 kg/m^3 (3853 lb/yd$^{3)}$	Plywood thermal conductivity	0.12 W/m.K
		Blanket thickness	
Heat generation curve	Found using isothermal calorimetry	Blanket R rating	N/A
		Time of shields removal	N/A During day 4

Internal temperature rise for the center of the footing is shown in Figure 48 where comparisons are made to the field sensor data. Further results for the side and bottom of the footing are illustrated in Figure 49. Finally, temperature differences are compared to field data in Figure 50.

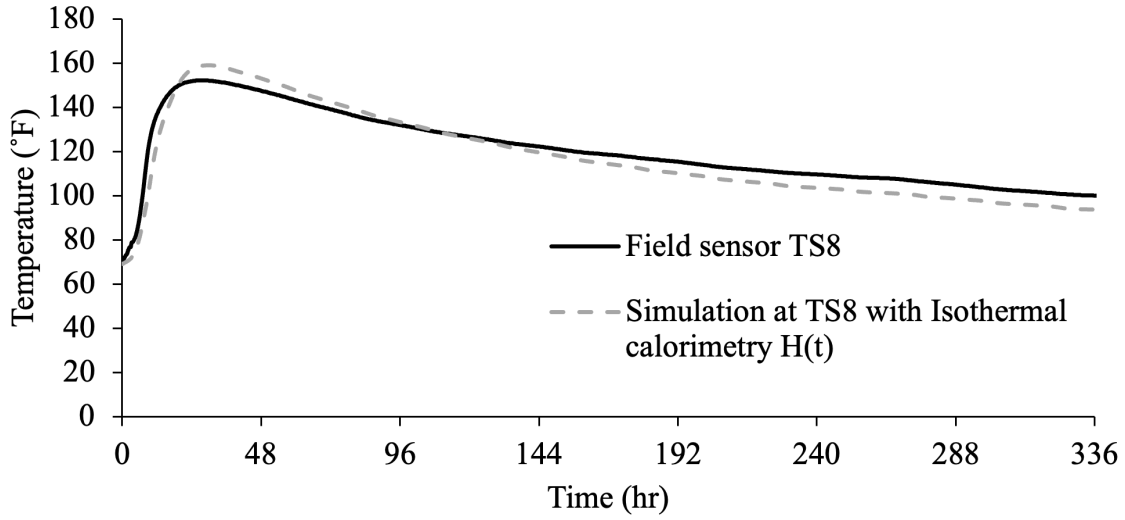

Figure 48. Graph. Comparison between isothermal calorimetry method and measured field internal temperature rise for center of footing (TS8).

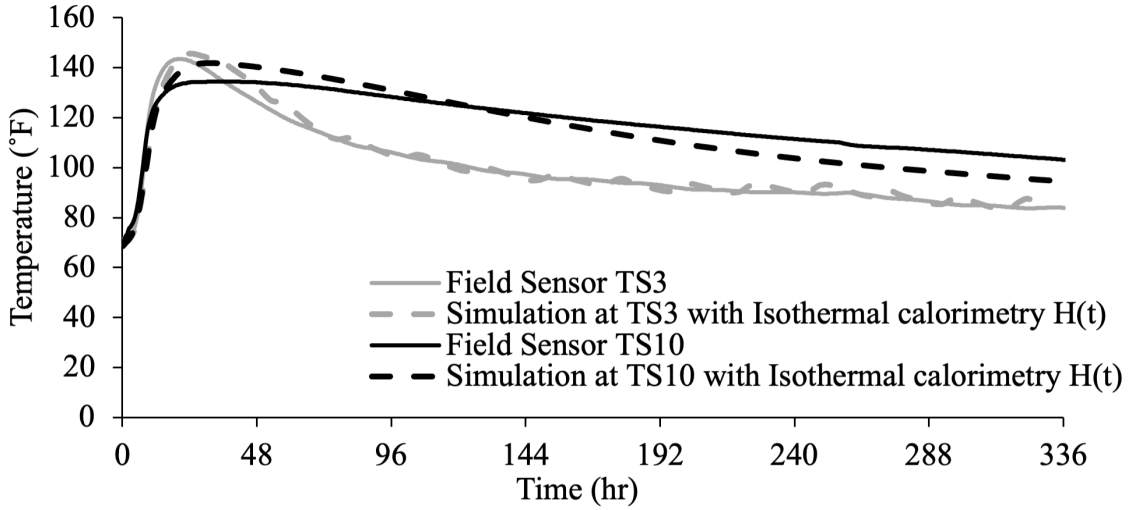

Figure 49. Graph. Comparison between isothermal calorimetry method and measured field internal temperature rise for side (TS3) and bottom (TS10) of footing.

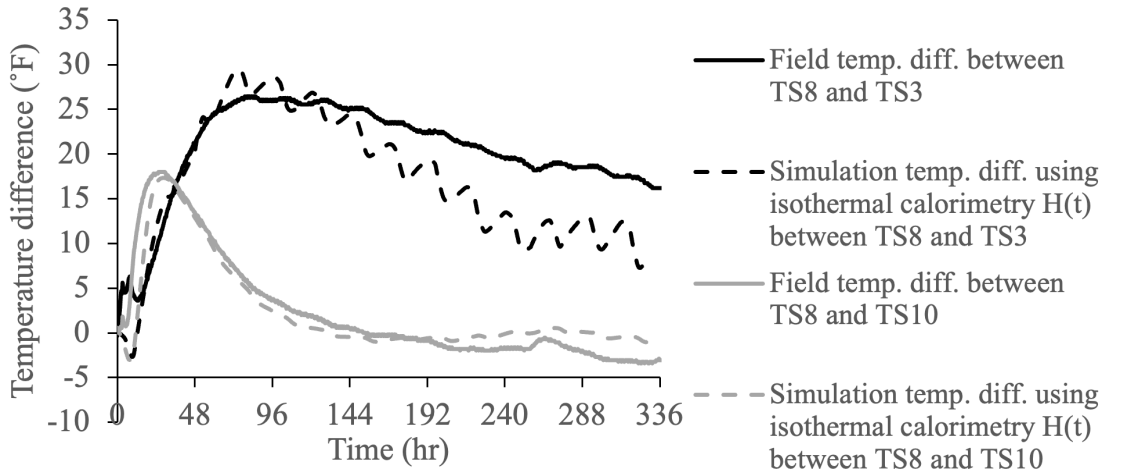

Figure 50. Graph. Comparison between isothermal calorimetry method and measured field temperature difference data of footing.

Table 22 summarizes the results of maximum temperature values, maximum temperature difference, as well as the time of occurrence for both phenomena using the calorimetry conversion method and the exponential method. It also compares results to field data by reporting the percent error.

Table 22. Summary of results for SR-92 footing.

Criterion \ Method	Field Measurements	Isothermal Calorimetry Method	
		Value	Error (%)
Maximum temperature (°F)	152.2	159.1	5.7
Time to maximum temperature (hr)	25.5	30.0	17.6
Maximum temperature difference (°F)	26.5	29.5	11.5
Time to maximum temperature difference (hr)	79.0	75.0	−5.1

As can be observed in Table 22, the isothermal calorimetry method enables the prediction of maximum temperatures, temperature differences, and their time of occurrence with good

accuracy. The presence of some deviations could be attributed to the modeling accuracy of the different field boundary conditions.

Abutment Wall

A cross-section of the abutment wall is displayed in Figure 51. It consists of a 13-span 38.86 m (127.5-ft) long steel girder bridge constructed on two concrete abutments. The abutments of the newly constructed bridge have a length of 18.18 m (60 ft) with a construction joint placed at 11.27 m (37 ft), a height of 6.23 m (20 ft), and a thickness of 1.83 m (6 ft), and are therefore qualified as mass concrete in the state of Georgia [68]. The wall was constructed during the month of September, with an average daily ambient temperature of 27.2°C (81°F). Wood was selected as the formwork material, where 19 mm (¾-inch) plywood was used and supported by steel members. The top of the wall was insulated using 6.35 mm (¼-inch) thick thermal blankets with an R-value rating of 1.08 ft^2°F·h/BTU. A layer of sand that is 50 to 75 mm (2 to 3 inch) in thickness was additionally placed on top the morning following the pour. Three of the side surfaces were also insulated using thermal blankets, whereas the fourth side is situated very close to a granite wall, as shown in Figure 51.

Two cooling measures were adopted for the construction of the abutment wall. The concrete was precooled during batching using liquid nitrogen until an initial placement temperature of 21.0°C (69.8°F) was reached. An embedded cooling pipe system was also installed as a postcooling measure. A closed-circuit system with a 100-ton air-cooled scroll rental chiller was used. The layout grid of the cooling pipes was 61 cm × 30.5 cm (2 ft × 1 ft), the greater spacing being along the length of the wall. Pipes of ¾-inch PEX were

used, which have an outside diameter of 22.225 mm (0.875 inch) and an inner diameter of 17.297 mm (0.681 inch). The cooling water temperature was kept at 7°C (45°F), and the water flow rate was 5 gpm. At this rate, the cooling water temperature at the chiller inlet and outlet did not change significantly. The cooling system started running before the concrete was poured, and it was stopped during the fourth day of construction. The removal of insulation and formwork also took place on the same day. All analysis parameters are summarized in Table 23.

Figure 51. Photo. SR-92 abutment wall and footing.

Table 23. b4cast thermal analysis input variables for SR-92 abutment wall.

Parameter	Input Value	Parameter	Input Value
Volume		**Cooling system**	
Initial temperature	21.0°C (69.8°F)	Pipe layout grid	30×60 cm (1×2 ft)
Time between batching and pouring	1 hour		Closed
		Cooling circuit	¾-in. PEX
		Cooling pipe designation	
Material		Cooling start time	0 hours
Activation energy	37589 J/mol	Cooling end time	95 hours
Density	2286 kg/m^3 (3853 lb/yd^3)	Cooling water temperature	7°C (45°F)
		Water flow rate	
Heat generation curve	Using isothermal calorimetry	Chiller capacity	1.5 m^3/h (7 gpm) 945000 kJ/h
Environmental factors		**Shields**	
Ambient temp.	TS16 sensor	Plywood thickness	19 mm (¾ in.)
Wind speed	3.6 m/s (8 mph)	Plywood thermal conductivity	0.12 W/m.K
		Blanket thickness	6.35 mm (¼ in.)
		Blanket R rating	6.13 m^2-K/W (1.08 ft^2·°F·h/BTU)
		Time of shields removal	During day 4

The abutment wall cement was tested using the isothermal calorimetry method, and the heat of hydration of concrete was calculated to supplement the finite element model. The obtained internal temperature rise for the center of the wall is shown in Figure 52, where comparisons are made to the field sensor data. The maximum temperature for the abutment wall is underpredicted by a 4.7 percent error, which is shown in Table 24. Since the abutment wall is cooled using an embedded cooling pipe system, the number of variables which could contribute toward this deviation are many. Most importantly, it has been noticed that the spacing between the cooling pipes during construction was not kept uniform throughout the length of the wall; an uncertainty which would affect the modeling results if present. The model is able to capture the rate of temperature development and the time at which the maximum temperature occurs with good accuracy, as shown in Table 24.

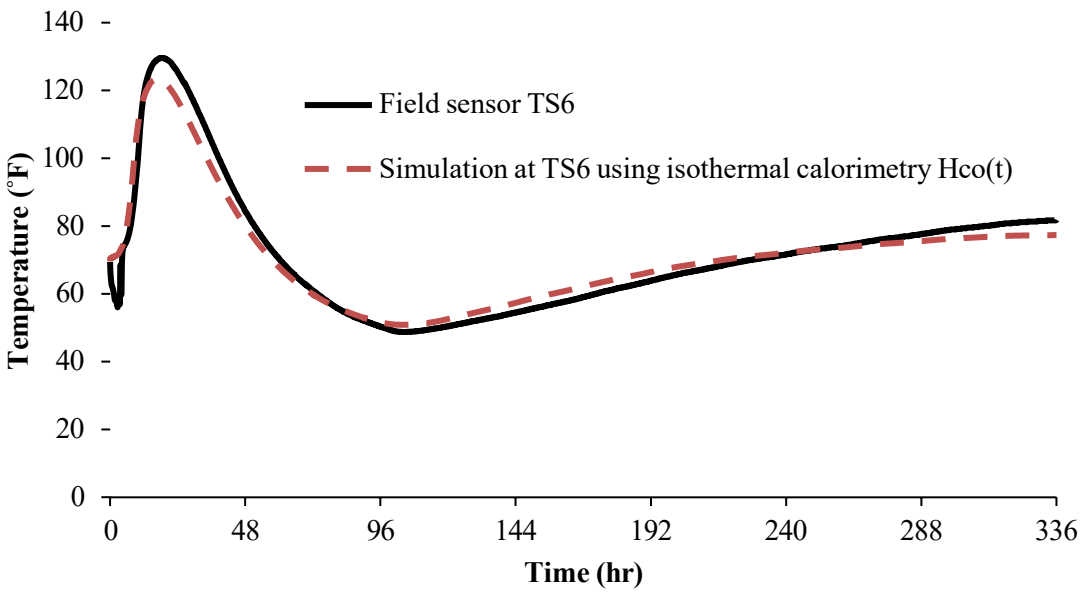

Figure 52. Graph. Comparison between isothermal calorimetry method and measured field internal temperature rise for center of abutment wall.

Table 24. Summary of results for SR-92 abutment wall.

Criterion \ Method	Field Measurements	Isothermal Calorimetry Method	
		Value	Error (%)
Maximum temperature °F	129.6	123.44	−4.7
Time to maximum temperature (hr)	17.75	17	−4.2

To conclude, it has been demonstrated that the isothermal calorimetry method is capable of accurately supplementing mass concrete simulations with in situ heat of hydration curves, necessary for the prediction of internal temperatures. It is proposed that the methodology is adopted for mass concrete projects by performing the isothermal calorimetry test at various temperatures for a given cementitious paste, including SCMs and admixtures. Based on our findings, it has also been demonstrated that the methodology

can give more accurate predictions when high-shear mixing is performed for the pastes to imitate the mixing action of concrete.

Standardized Mass Concrete Mixes

As mentioned previously, two types of cooling measures had to be implemented during the construction of SR-92 to control the temperature rise: (1) precooling using liquid nitrogen, and (2) postcooling using the cooling pipe system. In this section, the maximum internal temperatures and temperature differences are found for the SR-92 wall using several mixture designs previously proposed in Phase I of this project, in order to validate the efficiency of the mixes. A summary of the mixtures designs is shown in an ASTM C150 Type I/II OPC different than the one used in SR-92. 'FA' and 'BFS' refer to ASTM C618 Class F fly ash and ASTM C989 Grade 100 blast furnace slag, respectively, and 'Coarse cement' is a lower fineness ASTM C150 Type II (MH) cement. Finally, PCWR is a polycarboxylate superplasticizer. The chemical and physical properties of the cementitious materials are summarized in Table 26. In the table, 'Baseline' refers to an ASTM C150 Type I/II OPC different than the one used in SR-92.

Table 25. Proposed mass concrete mixture designs.

		Baseline	45% FA	25% FA	25% FA + 20% BFS	Coarse Cement
Cementitious Material (lb/yd^3)	**Cement**	696.6	379.8	521.3	410.4	525.6
	Slag	–	–	–	165.6	–
	FA (Type F)	–	315	173.8	124.2	–
	Total binder	696.6	364.8	695.0	700.2	700.2
	Water	340.2	342	327.3	342	309.6
	w/b	0.488	0.492	0.471	0.488	0.442
Aggregate (lb/yd^3)	**#67**	1684.8	1684.8	1701.0	1684.8	1701.0
	Natural sand	1254.6	1213.2	1226.0	1180.8	1267.2
	Coarse/fine ratio	1.34	1.39	1.39	1.43	1.34
Admixtures (lb/yd^3)	**PCWR**	13.932	13.896	20.850	14.004	14.004

Table 26. Chemical and physical properties of cements and SCMs.

	SR-92 Cement	Baseline	Coarse Cement	F Fly Ssh	BFS
Oxide Analysis (%)					
SiO_2	20.6	20.20	21.70	48.49	37.80
Al_2O_3	4.78	4.70	2.90	20.43	7.91
Fe_2O_3	2.82	3.30	4.50	15.91	0.72
CaO	64.18	62.90	64.10	6.99	42.69
MgO	1.86	3.00	3.10	1.12	11.44
SO3	2.79	3.40	2.90	2.21	0.79
Na_2O_{eq}	0.56	0.35	0.25	2.42	0.51
Phase Composition (%)					
C_3S	60.1	49	62	–	–
C_2S	13.3	20	16	–	–
C_3A	7.8	7	0	–	–
C_4AF	8.5	10	14	–	–
Blaine Fineness (m^2/kg)					
	411	411	303	–	–

The goal is to model the SR-92 abutment wall without the postcooling system using the different mix designs while keeping all other variables the same, including an initial placement temperature of 69.8°F. All cementitious pastes were tested at different temperatures using isothermal calorimetry to obtain the heat of hydration of concrete and subsequently simulate the internal temperatures and temperature differences. The results are shown in Figure 53 and Figure 54, respectively. Out of the four proposed mix designs (25% FA, 45% FA, 25% FA & 20% BFS, and coarse cement), all satisfy the maximum temperature limit, where the one containing 45 percent Class F fly ash and the one using the coarser cement are achieving lower temperatures. The 45% FA and the coarse cement mixes are also satisfying the maximum temperature difference limit up until 7 days, which is the time of insulation removal. After 7 days, the temperature difference for both mixtures crosses the threshold by a significantly smaller margin compared to other mixture designs. It can also be observed that the SR-92 cement gives the highest values for both temperature criteria.

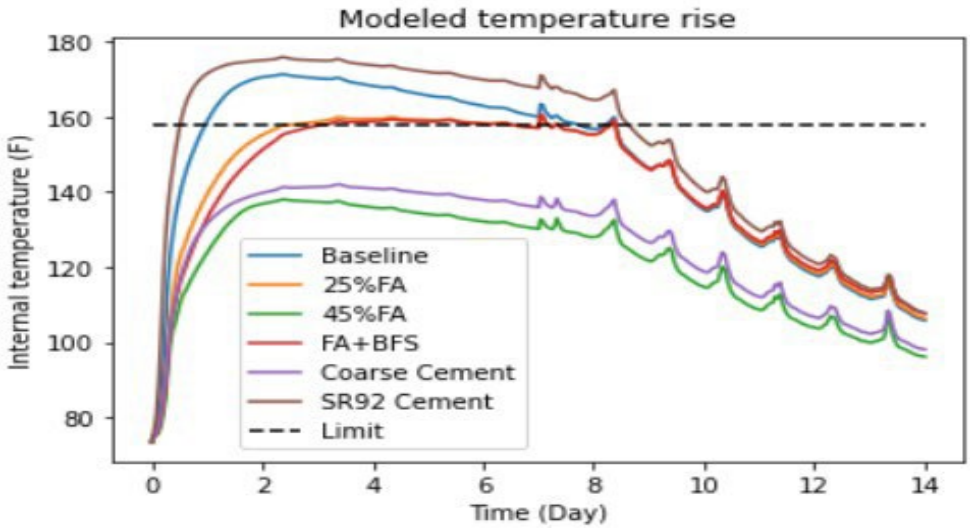

Figure 53. Graph. Maximum temperatures for the proposed mass concrete mixture designs and assuming no postcooling.

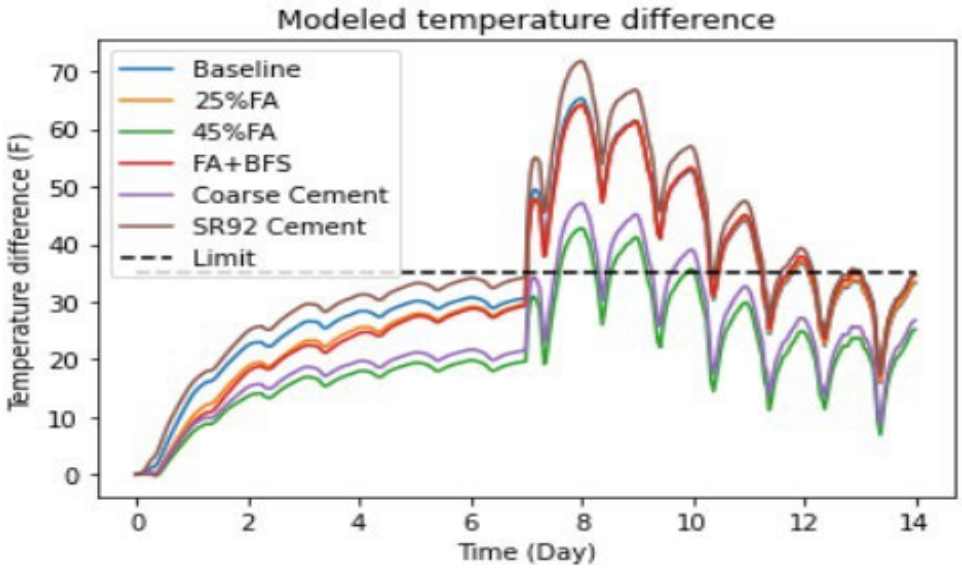

Figure 54. Graph. Maximum temperature difference for the proposed mass concrete mixture designs and assuming no postcooling.

The maximum temperature and temperature difference could be further reduced by reducing the initial placement temperature, if applicable, which is illustrated in Figure 55 and Figure 56 for an initial placement temperature of 59°F.

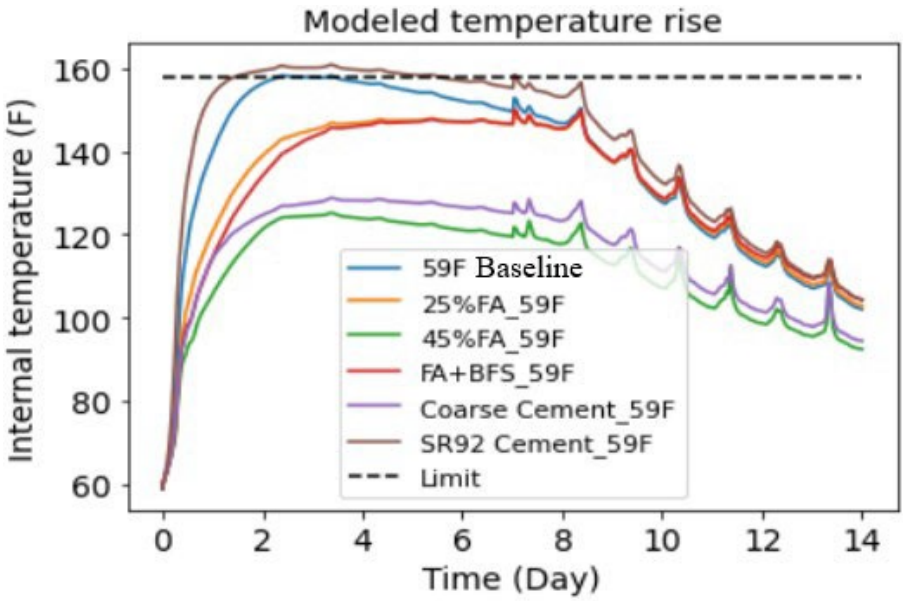

Figure 55. Graph. Maximum temperature difference for the proposed mass concrete mixture designs with 59°C placement temperature and assuming no postcooling.

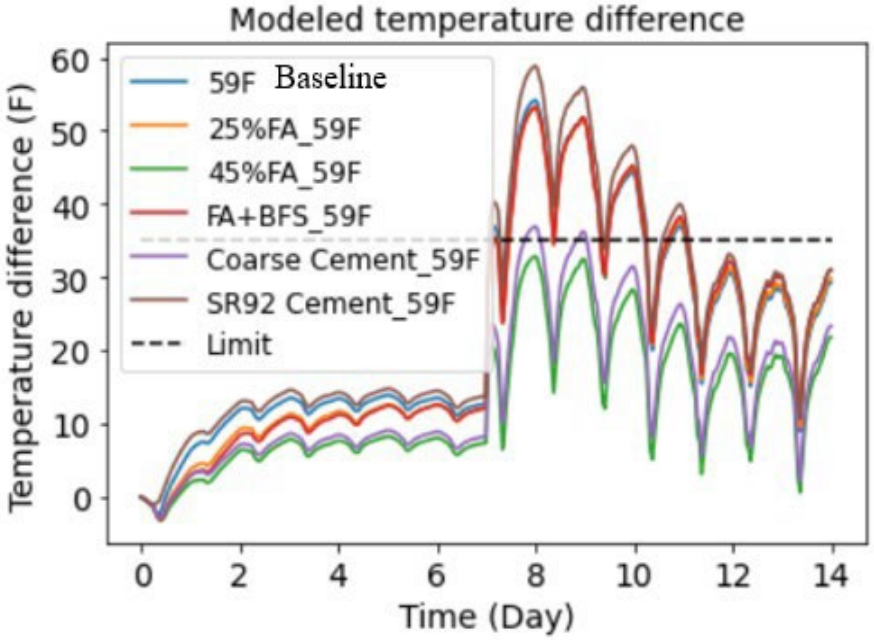

Figure 56. Graph. Maximum temperature difference for the proposed mass concrete mixture designs with 59°C placement temperature and assuming no postcooling.

In order to complete the assessment of the proposed mixture designs, it is important to consider the development of compressive strength and how it compares with the standard compressive strength of concrete class AA1 used in SR-92, which is 4500 psi at 28 days. It can be seen from Table 27 that all mixes, except the 45 percent fly ash, satisfy the strength requirement at 28 days and that the 45 percent fly ash mix catches up at 56 days.

Table 27. Compressive strength development of proposed mixture designs in psi.

Curing Day	SR-92 Cement	Baseline	45% FA	25% FA	FA + BFS	Coarse Cement
7	4496	5802	1885	3771	2901	5221
14	4641	6382	2611	4351	4496	6092
28	5511	7687	3771	4931	6092	6672
56	–	8122	4351	–	7252	7542

It is concluded that the proposed mixture designs can be used for the SR-92 abutment wall without the use of postcooling. The maximum temperature threshold is satisfied for all four mixes, and the maximum temperature difference can be satisfied if the initial placement temperature is further reduced. The compressive strength requirement is also met for all mixes by 56 days. It is important to consider that the thresholds for both temperature criteria are prescriptive and can be conservative. It has been shown in previous research that the maximum temperature threshold can be higher for mixes containing SCMs. A less conservative performance-based temperature difference limit that relies on the specifics of a specific project can also be investigated. Both of these considerations would allow more flexibility when optimizing the selection of mixture designs for mass concrete, while allowing for a less stringent thermal control plan.

MANAGING MASS CONCRETE WITH NOMOGRAMS

We may use the regression equation from Chapter 3 to explore the geometries at which mass concrete provisions may be required. The regression equation for non-postcooled concrete, equation 49, with the exponents as found by the regression from simulations using AA+ baseline concrete from Phase I, is:

$$T_{max,c} = C_1 \cdot T_{i,c}^{0.22} \cdot qA^{-0.66} \cdot V^{0.54} \cdot T_{\infty}^{0.07} \tag{49}$$

where, C_1 = 81.5 (in a complex set of SI units) and ΔT_a = 64°C = 115°F. This equation was regressed on simulation data that were in SI units (meters, kilograms, degrees Celsius), so $T_{max,c}$ is in degrees Celsius, but results here are presented in USCS units.

Although the simulation data underlying this surrogate model employed the AA+ baseline concrete, we might provisionally adapt this equation to the SR92 concrete used for the abutment wall, in which case C_1 = 67.2 (in a complex set of SI units) and ΔT_a = 52°C = 94°F.

Based on the dimensional analysis that underlies equation 49, which postulates that $\partial\partial_{ccaaee,c}$ is a function partially of $VV^2/qqMM^3$ (with, as it turns out in this case, an exponent applied to this quotient), we may use equation 49 to state that, approximately:

$$T_{max,c} \sim \sqrt{\frac{V}{qA^{1.24}}} \tag{50}$$

all else (initial and ambient temperatures) being equal. Considering a variety of cuboidal shapes under a prototypical summer condition of $T_{i,c}$ = 80°F for an initial temperature and T_{∞} = 85°F for an average, conservative, ambient temperature, Figure 57 shows that volume

to area ratios V/qA of between 1.2-1.4 ft. approach or exceed a maximum threshold temperature of 165°F. Figure 58 depicts this surrogate model under cooler conditions: $T_{i,c}$ = 70°F and T_{∞} = 70°F. Both figures show some outliers that do not fit with an expected asymptotic approach to a maximum temperature, e.g. the larger V/qA ratios above 1.9; these are for shapes with higher aspect ratios (thick walls or slabs) than the more compact shapes on which the surrogate model was regressed and suggested caution in using this surrogate model and the nomograms for high-aspect-ratio shapes.

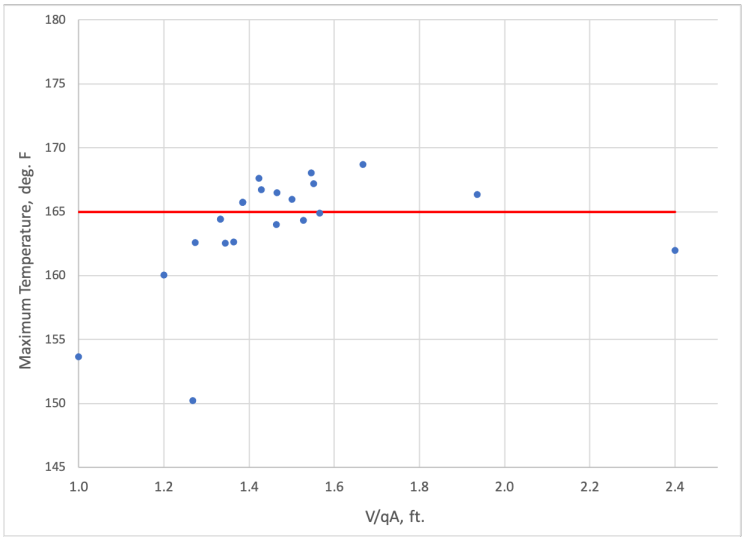

Figure 57. Graph. Maximum temperature vs. volume to heat transfer ratio using the surrogate model, SR-92 abutment wall at $T_{ii,c}$ = 80°F and T_{∞} = 85°F.

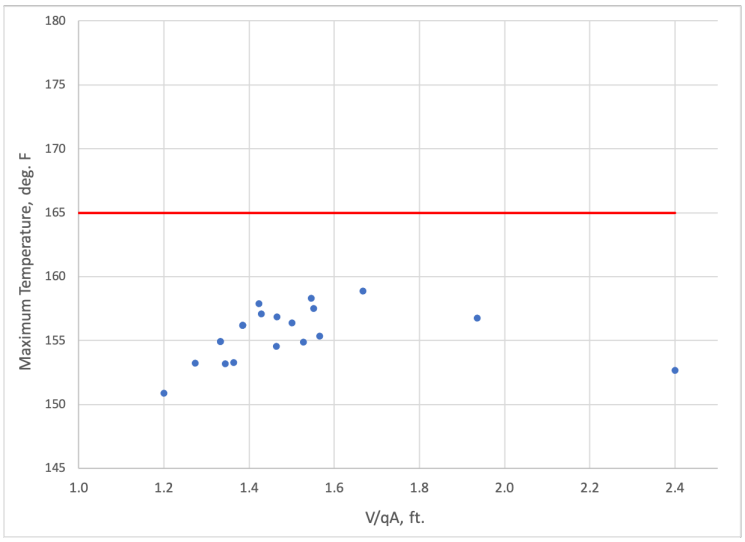

Figure 58. Graph. Maximum temperature vs. volume to heat transfer ratio using the surrogate model, SR-92 abutment wall at $T_{ii,c}$ = 70°F and T_{∞} = 70°F.

Example Creation of an Initial Thermal Control Plan Using Nomograms

As a brief example of using the nomograms to develop an initial thermal control plan (or to explore the possible plans available), consider the following:

- Cuboid 6 ft wide × 8 ft deep × 10 ft high.
    - qA = 328 ft^2, V = 17.8 yd^3, V/qA = 1.5 ft.
- To be poured in June, with an average outdoor temperature assumed conservatively to be 85°F.
- Concrete mix: SR-92 mix, with admixtures, as used for the wall:
    - Adiabatic temperature rise of 94°F
    - Given June conditions, say that at mixing, cement is at 120°F, the water is at 73°F, and the aggregates are at 80°F.

We first use the case 1 nomogram, adapted to this concrete, to determine the fresh concrete temperature and maximum theoretical temperature (see Figure 59).

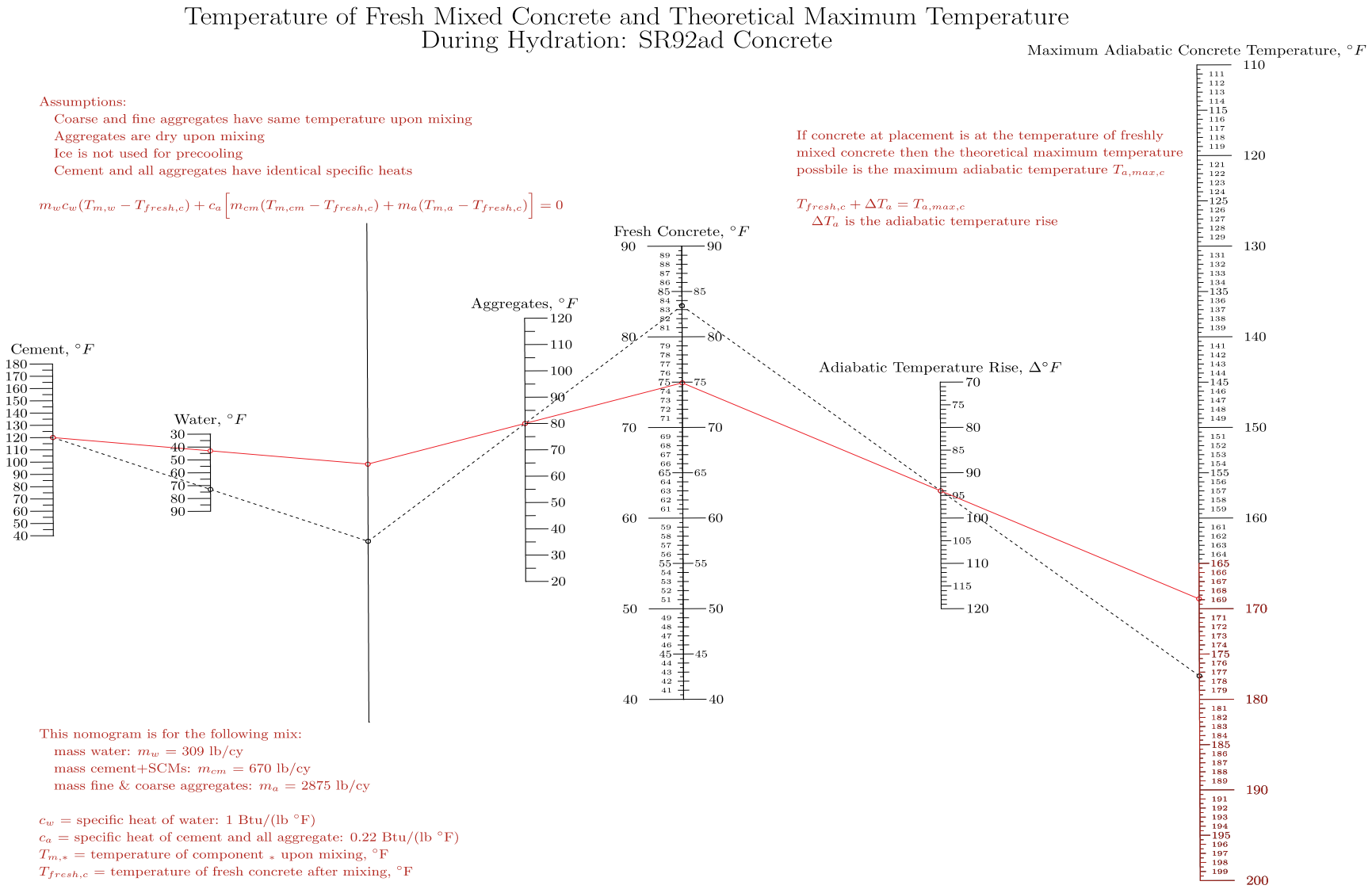

Figure 59. Illustration. Temperature of fresh concrete and maximum theoretically possible temperatures.

Here, the black dashed isopleth shows the fresh concrete is expected to be about 83.5°F and the maximum theoretical temperature to be about 178°F. The red isopleth depicts the change if the water were to be chilled to 43°F: fresh concrete temperature is now 75°F and maximum theoretical concrete temperature is 169°F (the fresh temperature of 75°F could, of course, be achieved in many other ways, including the use of liquid nitrogen at the truck). One could continue to investigate further precooling until the maximum theoretically possible temperature is well below the threshold temperature, here 165°F; however, for this example, we stop and consider the degree to which the 3D shape of this cuboid reduces this maximum temperature.

PROVISIONAL Maximum concrete temperature: V/qA > 1 ft.

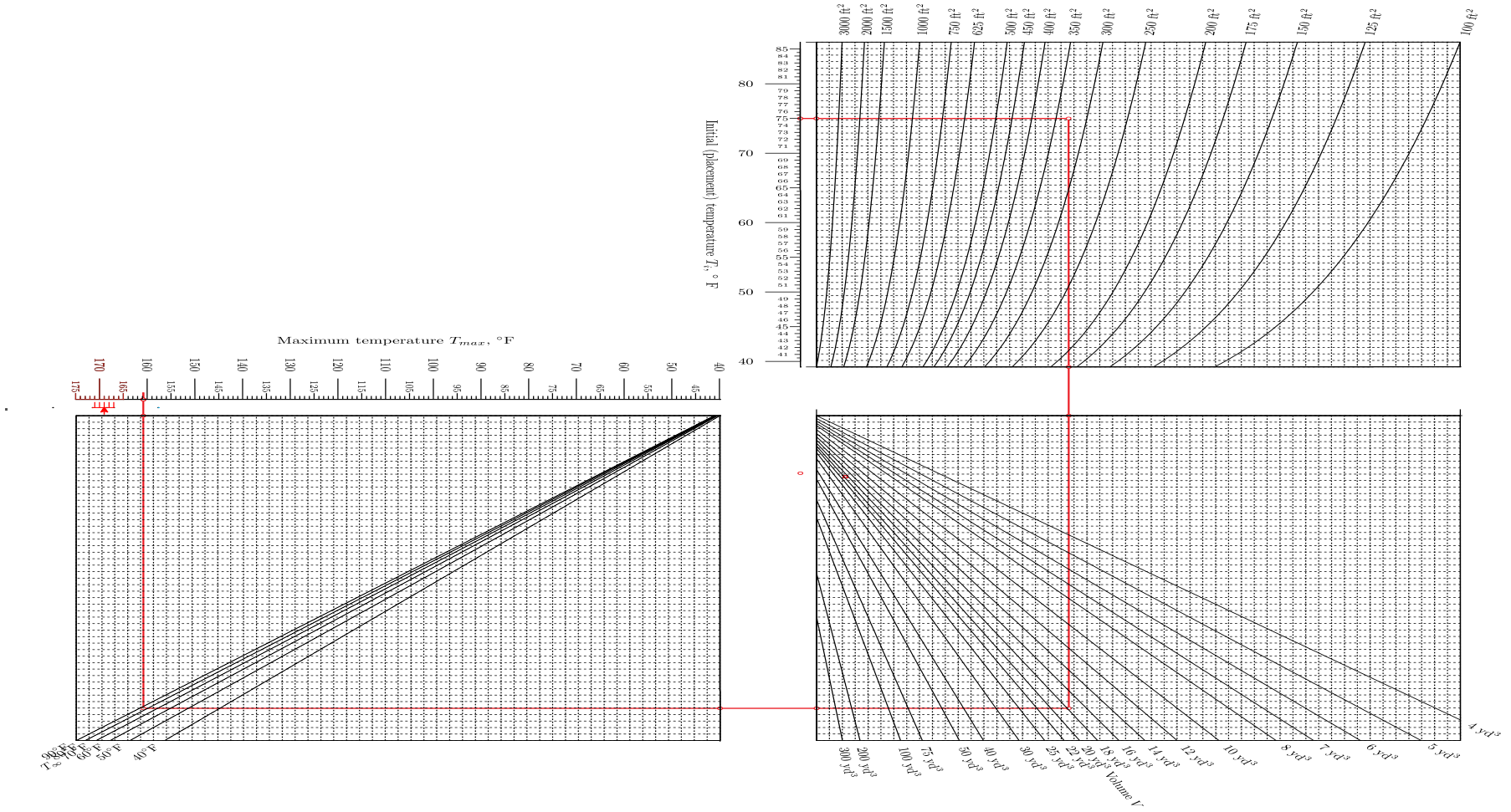

Figure 60. Illustration. Expected maximum temperature, accounting for shape.

Figure 60 shows an expected maximum temperature of 161°F, 8°F cooler than the adiabatic case (the arrow associated with the quartile plot below the maximum temperature axis has been positioned to depict the adiabatic temperature in this figure). While this is below the threshold of 165°F, given the errors associated with this nomogram, it is prudent to consider postcooling options.

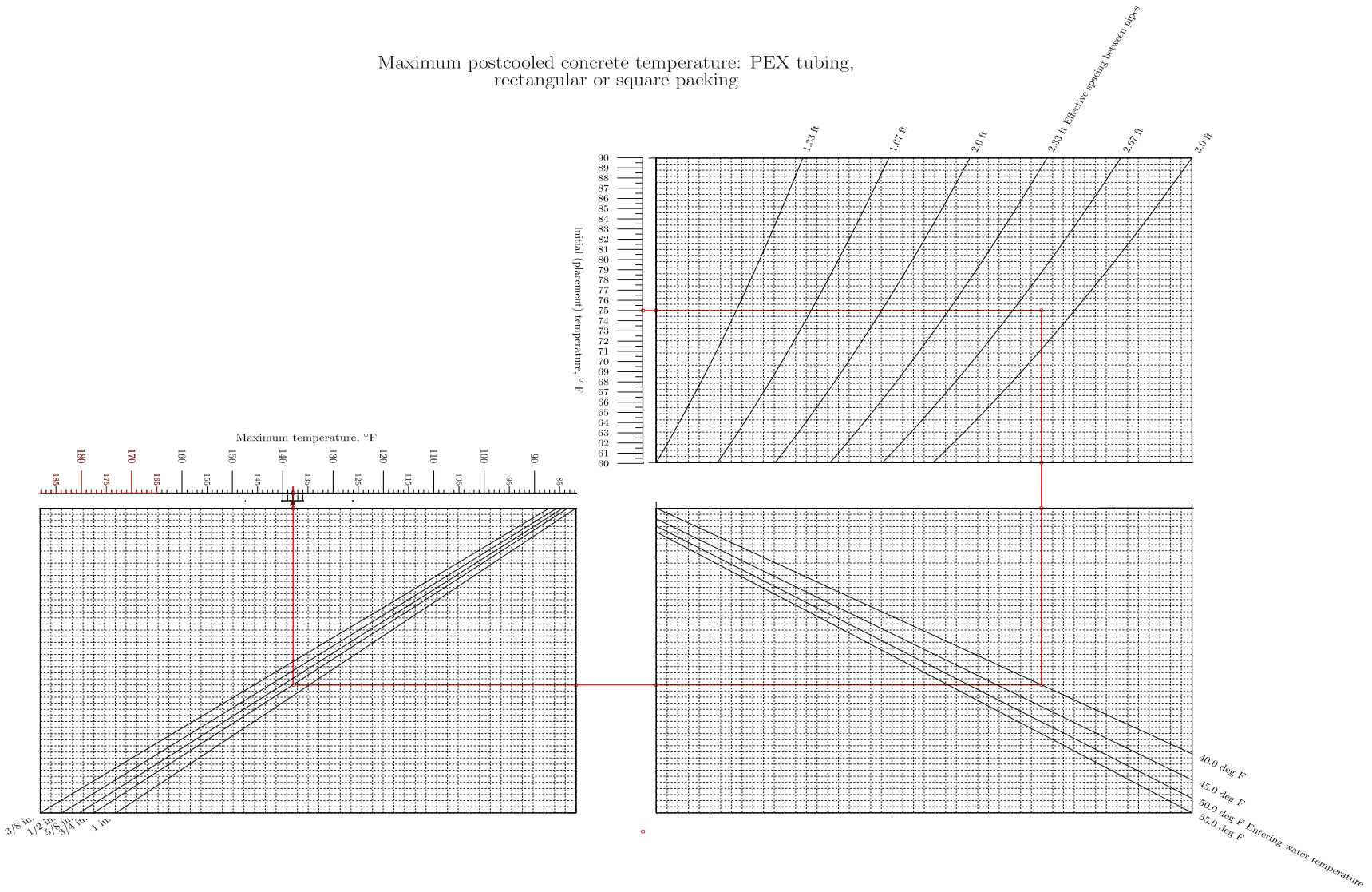

Figure 61. Illustration. Square pipe packing, some precooling.

Figure 61 gives an example for rectangular packing of ¾-inch PEX pipes circulating 40°F water. Here the pipe to pipe spacing is 2 ft in nondiagonal directions. Using an effective spacing of half the diagonal distance between pipes in this nomogram gives an estimated maximum temperature of 138°F when the initial temperature of the concrete is 75°F. Here, the quartile plot is centered on the isopleth at the maximum temperature axis; the minimum and maximum error dots are well away from the 165°F threshold, which gives some confidence to this setup at this initial stage.

This low temperature suggests that precooling may not be necessary for this situation. Figure 62 shows a nomogram with the same cooling arrangement as Figure 61 but with an initial temperature of 85°F—slightly more than the original freshly mixed temperature of 83.5°F. Maximum estimated temperature is 149°F, and the maximum error dot of the quartile plot is still less than 165°F, indicating this initial temperature and cooling system concept is a good candidate for further analysis.

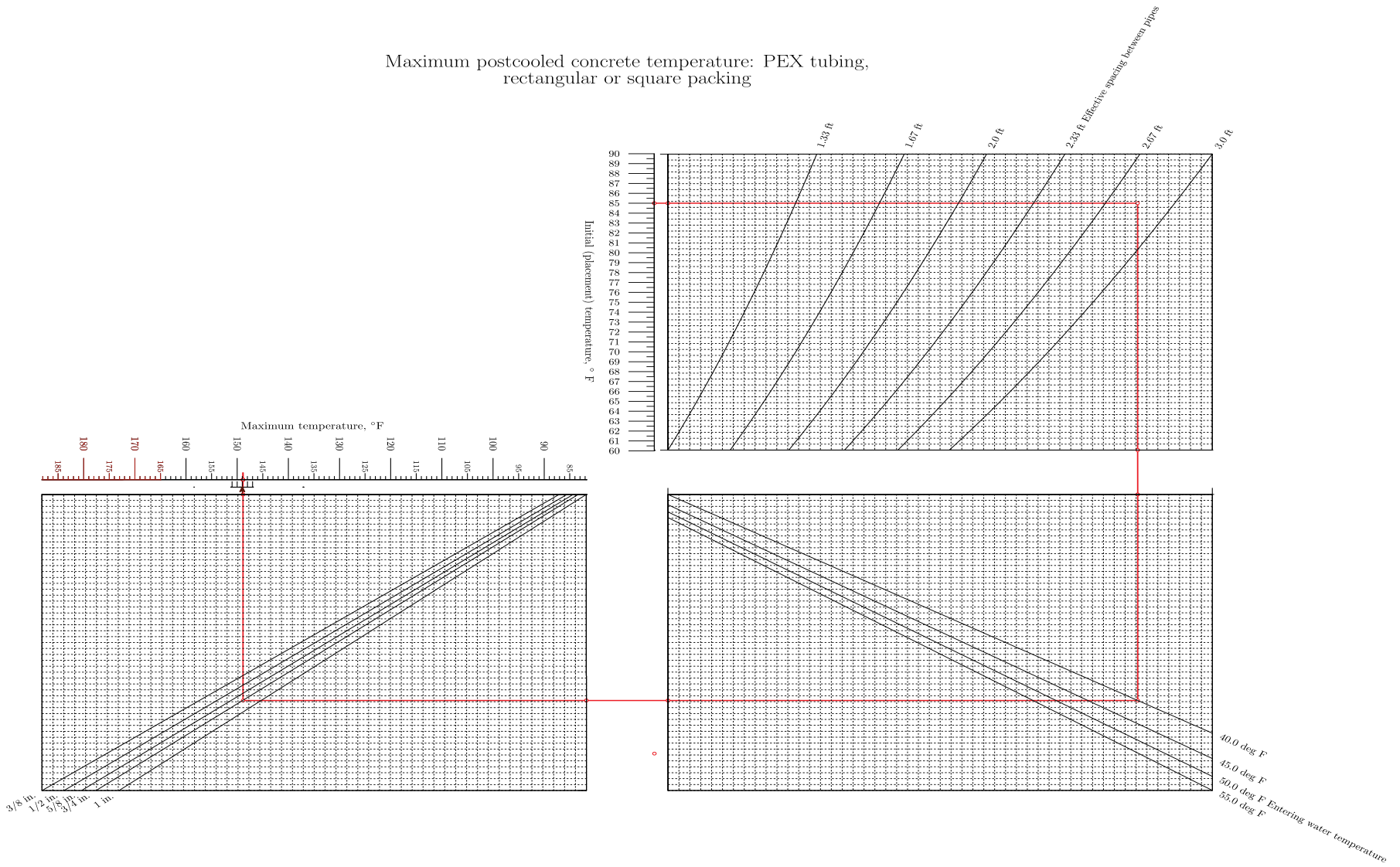

Figure 62. Illustration. Square pipe packing, no precooling.

This is not the only way the nomograms can be used; as mentioned in Chapter 3; one may read the nomogram “backward,” starting with a desired maximum temperature and reading the cooling system parameters back to the initial temperature, in which case one may determine the maximum initial temperature that must not be exceeded.

CHAPTER 8. CONCLUSION

This research was conducted as a series of six tasks. In Task 1, the research team conducted a real-world case study to identify the thermal behavior of the non-mass concrete structure and the mass concrete structure. The temperature data collected from the case study were used as a reference for the temperature nomogram development and validation. In addition, the research team also obtained cost information on the thermal control methods applied to the SR-92 bridge construction projects. The cost data were used to generate the cost nomogram.

Based on the thermal behavior measured from the case study, in Task 2, the research team developed simple temperature-prediction tools using nomograms to support appropriate thermal control method selection. A series of nomograms to aid in planning mass concrete projects have been developed based on first principles and on a suite of simulations. The major objective of these nomograms is to help users identify and eliminate doubtful parameter space and aid in rapidly finding candidate thermal management plans to be verified with more detailed—but fewer—analyses.

In addition, isothermal calorimetry tests were conducted at different temperatures to obtain the rate of heat release of cement in Task 3. The methodology intrinsically considers the chemical and physical characteristics of the mix design, necessarily considers the effect of placement and curing temperatures on the rate of heat release, and does not require information on the thermal properties of the calorimeter. The proposed methodology was validated through two mid-scale concrete experiments previously performed in Phase 1

research, and findings demonstrate that it was successful in predicting internal temperatures for both the uncooled and actively cooled mid-scale experiments.

In Task 4, the research team proposed an alternative modeling approach for the heat of hydration of mass concrete structures using machine learning. The Gaussian process regression model was used to predict the heat of hydration histories up to 72 hours at different isothermal temperatures. The ability of the GPR model to predict thermal behavior with reasonable accuracy was validated with 92 percent of the average R^2. The model was then used to predict the heat of hydration curves for a cement belonging to two mid-scale mass concrete experiments. The ability to use the predictions of the machine learning model and upscale them for application in real-life engineering and decision-making systems has been proven. The model can be expanded to include more features related to other types of supplementary cementitious materials and possibly admixtures.

The research team also conducted a comprehensive economic analysis of thermal control methods based on the cost information collected from a case study and literature review in Task 5. A cost nomogram was developed to estimate the cost for thermal control methods, including precooling and postcooling methods. The cost nomograms simply generated the total cost to cool the concrete with several methods. The economic analyses of the cooling methods were performed based on real-world case studies, and the results were compared to alternative designs and thermal management methods. Although the cost nomogram may not estimate the exact cost because it varies depending on the location and manufacturer, we expect the cost nomogram can be used for resources to select a cost-effective thermal control plan.

In Task 6, the research team included and integrated outcomes from Tasks 1 to 5 to provide the best practices or tools for: (1) mix design selection, and (2) active thermal control plan selection. The best practices and tools for mix-design selection were developed with isothermal calorimetry demonstrated in Chapter 4. The ways of using nomograms with thermal parameters are described. The research team also presented ways of managing mass concrete construction with nomograms in this task.

In summary, the research team presented a simple decision-making guideline for thermal control methods using nomograms in mass concrete construction. The nomograms include temperature nomograms and cost nomograms for both precooling and postcooling scenarios. The temperature nomograms were created based on isothermal calorimetry tests and regression models using numerous simulation data, and the cost nomograms used closed-form equations to calculate the total cost. To validate the proposed methods, this study conducted a case study with an actual bridge construction project.

Although the developed decision-making guideline can provide cost-effective alternatives for mass concrete thermal control in given conditions, several limitations are also found in the proposed nomograms. First, the temperature nomograms developed in this study work well under ordinary Portland cement concrete. Since the hydration heat differs depending on the amount of cementitious material, the temperature prediction model must be modified if the SCM is added. Furthermore, the current version of nomograms cannot predict the temperature difference, which is also a significant factor to be managed in mass concrete construction. Therefore, in a future study, we will develop an extended nomogram that can calculate both maximum temperature and temperature difference, and consider different mix designs.

ACKNOWLEDGMENTS

The research reported herein was sponsored by the Georgia Department of Transportation (GDOT) through Research Project Number 19-04. The research team acknowledges and appreciates the help of the Georgia Department of Transportation personnel who participated and supported this project, especially Mr. Marc Mastronardi, Director of Construction; Mr. John Hancock, Administrator of Construction; Mr. Beau Quarles, Assistant State Construction Administrator; and Mr. Sunil Thapa, Research Implementation Manager. In addition, special thanks to Mr. Joseph Visockis of CW Matthews, who provided the research team with important information on the SR 92 project and supported the team's data collection from the construction site.

REFERENCES

1. American Concrete Institute (ACI) (2005). *ACI 207.1R-05, Guide to Mass Concrete*, Farmington Hills, MI, pp. 1–30.

2. Cho, Y.K., Gentry, R., Brown, J., Kahn, L.F., and Park, J. (2019). *Investigation and Guidelines for Mass Concrete Construction Management*, FHWA-GA-19-1625, Georgia. Department of Transportation, Available online: https://rosap.ntl.bts.gov/view/dot/-40282.

3. Al-Manaseer, A. and Elias, N. (2008). *Placement of Mass Concrete for Cast-in-place Concrete Piling: The Effects of Heat of Hydration of Mass Concrete for Cast-in-place Piles*. California Department of Transportation, Division of Research and Innovation, Sacramento.

4. Florida Department of Trasportation (FDOT) (2015). "Specifications for Limerock Base and Stabilized Base Materials (Section 911)." In *Road and Bridge Construction Manual*, Tallahassee. Available online: http://www.dot.state.fl.us/statematerialsoffice/administration/resources/library/materialsbulletins/expired/2010/mb06-10.pdf.

5. American Concrete Institute (ACI) (2020). *Cooling and Insulating Systems for Mass Concrete*. ACI PRC-207.4R-20, Farmington Hills, MI.

6. Evesham, H.A. (1982). *The History and Development of Nomography*, Docent Press, LLC, Boston, MA.

7. Hankins, T.L. (1999). "Blood, Dirt, and Nomograms: A Particular History of Graphs." *Isis*, *90*(1), pp. 50–80.

8. Brodetsky, S. (1920). *A First Course in Nomography*. G. Bell and Sons, Ltd.

9. Balachandran, V.P., Gonen, M., Smith, J.J., and DeMatteo, R.P. (2015). "Nomograms in Oncology: More than Meets the Eye." *The Lancet Oncology*, *16*(4), pp. e173–e180.

10. American Concrete Institute (ACI) (2007). *Report on Thermal and Volume Change Effects on Cracking of Mass Concrete*. ACI PRC-207.2R-07, Farmington Hills, MI.

11. Kosmatka, S.H. (1992). *Design and Control of Concrete Mixtures*. 13th Edition, Portland Cement Association, Skokie, IL.

12. Silva, W.R. and Smilauer, V. (2015). "Nomogram for Maximum Temperature of Mass Concrete." *Concrete International*, *37*(5).

13. Nguyen, T.C., Nguyen, V.Q., Aniskin, N., Phung, B.T., and Hoang, Q.L. (2021). "Building a Nomogram to Predict Maximum Temperature in Mass Concrete at an Early Age." *E3S Web Conference*, 263.

14. Roschier, L. and Boulet, D. (2020). *PyNomo*. (website) https://github.com/lefakkomies/-pynomo.

15. Incropera, F.P. and DeWitt, D.P. (1990). *Introduction to Heat Transfer*, John Wiley and Sons.

16. Lienhard, IV, J.H. and Lienhard, V, J.H. (2020). *A Heat Transfer Textbook*. 5th Edition, Phlogiston Press, Cambridge, MA. http://ahtt.mit.edu.

17. Riding, K.A., Poole, J.L., Folliard, K.J., Juenger, M.C.G., and Schindler, A.K. (2011). "New Model for Estimating Apparent Activation Energy of Cementitious Systems." *ACI Materials Journal*, *108*(5), pp. 550–557.

18. K.A. Riding, J.L. Poole, K.J. Folliard, M., Juenger, C.G., and Schindler, A.K. (2012). "Modeling Hydration of Cementitious Systems." *ACI Materials Journal*, *109*(2), pp. 225–234.

19. Cervera, M., Javier, O., and Tomás, P. (1999). "Thermo-ChemoMechanical Model for Concrete. I: Hydration and Aging." *Journal of Engineering Mechanics*, *125*(9), pp. 1018–1027.

20. Zhou, W., Feng, C., Liu, X., Liu, S., and Zhang, C. (2016). "A Macro–Meso Chemophysical Analysis of Early-age Concrete Based on a Fixed Hydration Model." *Magazine of Concrete Research*, *68*(19), pp. 981–994.

21. Zhou, W., Tian, W., Qi, T., Liu, S., Feng, C., Ma, G., and Chang, X. (2020). "Investigation on Hydration and Mechanical Properties of Mortar Containing Limestone Powder and Fly Ash Based on the Coupled Chemical–Thermal–Mechanical Method." *Materials*, *13*(19), pp. 4387.

22. Logg, A., Kent-Andre, M., and Wells, G. (2012). *Automated Solution of Differential Equations by the Finite Element Method*. Springer, New York.

23. Alnaes, M.S., Blechta, J., Hake, J., Johansson, A., Kehlet, B., Logg, A., Richardson, C., Ring, J., Rognes, M., and Wells, G. (2015). *The FEniCS Project Version 1.5*. Archive of Numerical Software 3. Available online: https://doi.org/10.11588/ANS.2015.100.20553.

24. Buckingham, E. (1914) "On Physically Similar Systems; Illustrations of the Use of Dimensional Equations." *Physical Review*, *4*(4), pp 345–376.

25. Sonin, A. (2004). "A Generalization of the Pi-theorem and Dimensional Analysis." *Proceedings of the National Academy of Sciences of the United States of America*, *101*(23), pp. 8525–6.

26. Seabold, S. and Perktold, J. (2010). "statsmodels: Econometric and Statistical Modeling with Python." In *9th Python in Science Conference*.

27. Myers, T.G., Fowkes, N.D., and Ballim, Y. (2009). "Modeling the Cooling of Concrete by Piped Water." *Journal of Engineering Mechanics*, *135*(12), pp. 1375–1383.

28. Saleh, J.M. (2002). "Heat Transfer In Pipe Flow." In *Fluid Flow Handbook*, 1st Edition, McGraw-Hill Education, New York. Available online: https://www.accessengineeringlibrary.com/content/book/9780071363723/chapter/c.

29. Silcox, G.D., Noble, J.J., Sarofim, A.F., Wankat, P.C., and Knaebel, K.S. (2019). *Heat Transfer by Convection.* In D.W. Green, M.Z. Southard (eds.), *Perry's Chemical Engineers' Handbook*, 9th Edition, McGraw-Hill Education, New York. Available online: https://www.accessengineeringlibrary.com/content/book/9780071834087/toc-chapt.

30. Burns, K.J., Vasil, G.M., Oishi, J.S., Lecoanet, D., and Brown, B.P. (2020). "Dedalus: A Flexible Framework for Numerical Simulations with Spectral Methods." *Physical Review Research*, *2*(2), 023068.

31. Giunta, A., Wojtkiewicz, S., and Eldred, M. (2003). "Overview of Modern Design of Experiments Methods for Computational Simulations." In *41st Aerospace Sciences Meeting and Exhibit*, Aerospace Sciences Meetings, American Institute of Aeronautics and Astronautics.

32. Viana, F.A.C. (2016). "A Tutorial on Latin Hypercube Design of Experiments." *Quality and Reliability Engineering International*, *32*(5), pp. 1975–1985.

33. Geuzaine, C. and Remacle, J.-F. (2009). "Gmsh: A 3-D finite element mesh generator with built-in pre- and post-processing facilities." *International Journal for Numerical Methods in Engineering*, *79*(11), pp. 1309–1331.

34. Cole, K.D. (2010). *Heat Conduction Using Green's Functions*. 2nd Edition, CRC Press, Boca Raton, FL.

35. Haji-Sheikh, A. (2014). *Temperature and Heat Flux Solutions in Two-layer Concentric Hollow Cylinders with Prescribed Surface Conditions and Volumetric Heat Sources*. R3C13B00G11, University of Nebraska-Lincoln. Available at: https://exact.unl.edu.

36. Iooss, B. and Saltelli, A. (2016). "Introduction to Sensitivity Analysis." In Ghanem, R., Higdon, D., and Owhadi, H. (eds.), *Handbook of Uncertainty Quantification*, Springer International Publishing, pp. 1– 20.

37. Herman, J. and Usher, W. (2017). "SALib: An Open-source Python Library for Sensitivity Analysis." *The Journal of Open Source Software*, *2*(9).

38. Escalante-Garcıa, J. and Sharp, J. (1998). “Effect of Temperature on the Hydration of the Main Clinker Phases in Portland Cements: Part II, Blended Cements.” *Cement and Concrete Research*, *28*, pp. 1259–1274.

39. Wadso, L. (2003). *An Experimental Comparison between Isothermal Calorimetry, Semi-adiabatic Calorimetry and Solution Calorimetry for the Study of Cement Hydration (NT TR 522)*. NORDTEST.

40. Xu, Q., Wang, K., Medina, C., and Engquist, B. (2015). “A Mathematical Model to Predict Adiabatic Temperatures from Isothermal Heat Evolutions with Validation for Cementitious Materials.” *International Journal of Heat and Mass Transfer*, *89*, pp. 333–338.

41. Han, D. and Ferron, R.D. (2016). “Influence of High Mixing Intensity on Rheology, Hydration, and Microstructure of Fresh State Cement Paste.” *Cement and Concrete Research*, *84*, pp. 95–106.

42. ASTM International (2017). *ASTM C1679 Standard Practice for Measuring Hydration Kinetics of Hydraulic Cementitious Mixtures Using Isothermal Calorimetry*. ASTM International, West Conshohocken, PA.

43. ASTM International (2019). *ASTM C1738 / C1738M-19, Standard Practice for High-Shear Mixing of Hydraulic Cement Pastes*. ASTM International, West Conshohocken, PA.

44. Van Breugel, K. (1980). *Artificial Cooling of Hardening Concrete*. Report Stevin Laboratory, Concrete Structures 5-80-9.

45. *b4cast – Simulation of Hardening Concrete*. Available online: http://www.b4cast.com/b4cast/b4cast.html, accessed April 1, 2022

46. Ford, E., Kailas, S., Maneparambil, K., and Neithalath, N. (2020). “Machine Learning Approaches to Predict the Micromechanical Properties of Cementitious Hydration Phases from Microstructural Chemical Maps.” *Construction and Building Materials*, *265*, 120647.

47. Ford, E., Maneparambil, K., and Neithalath, N. (2021). “Machine Learning on Microstructural Chemical Maps to Classify Component Phases in Cement Pastes.” *Journal of Soft Computing in Civil Engineering*, *5*, pp. 1–20.

48. Oey, T., Jones, S., Bullard, J.W., and Sant, G. (2020). “Machine Learning Can Predict Setting Behavior and Strength Evolution of Hydrating Cement Systems.” *Journal of the American Ceramic Society*, *103*, pp. 480–490.

49. Sargam, Y., Wang, K., and Cho, I.H. (2021). “Machine Learning Based Prediction Model for Thermal Conductivity of Concrete.” *Journal of Building Engineering*, *34*, 101956.

50. Nilsen, V., Pham, L.T., Hibbard, M., et al. (2019). “Prediction of Concrete Coefficient of Thermal Expansion and Other Properties Using Machine Learning.” *Construction and Building Materials*, *220*, pp. 587–595.

51. Trtnik, G., Kavčič, F., and Turk, G. (2008). “The Use of Artificial Neural Networks in Adiabatic Curves Modeling.” *Automation in Construction*, *18*, pp. 10–15.

52. Evsukoff, A.G., Fairbairn, E.M., Faria, É.F., et al. (2006). “Modeling Adiabatic Temperature Rise During Concrete Hydration: A Data Mining Approach.” *Computers & Structures*, *84*, pp. 2351–2362.

53. Wang, L., Yang, B., Chen, Y., et al. (2012). “Modeling Early-age Hydration Kinetics of Portland Cement Using Flexible Neural Tree.” *Neural Computing and Applications*, *21*, pp. 877–889.

54. Cook, R., Han, T., Childers, A., et al. (2021). “Machine Learning for High-Fidelity Prediction of Cement Hydration Kinetics in Blended Systems.” *Materials & Design*, 109920.

55. Rasmussen, C.E. (2003). “Gaussian Processes in Machine Learning.” In *Summer School on Machine Learning*, Springer, pp. 63–71.

56. ASTM International. *C09 Committee Practice for Measuring Hydration Kinetics of Hydraulic Cementitious Mixtures Using Isothermal Calorimetry*. ASTM International, West Conshohocken, PA.

57. Nadelman, E.I. (2016). *Hydration and Microstructural Development of Portland Limestone Cement-based Materials*. Ph.D. thesis, Georgia Institute of Technology.

58. Cardelino, N.H. (2018). *Design of Self-consolidating Precast Concrete Using Powdered Limestone*. Ph.D. thesis, Georgia Institute of Technology.

59. Dolphyn, B.P. (2016). *Laminar Cracking in Post-tensioned Concrete Nuclear Containment Buildings*. Ph.D. thesis, Georgia Institute of Technology.

60. Poole, J.L., Riding, K.A., Juenger, M.C.G., et al. (2010). “Effects of Supplementary Cementitious Materials on Apparent Activation Energy.” *Journal of ASTM International*, *7*, pp. 1–16.

61. Van Breugel, K. (1998). “Prediction of Temperature Development in Hardening Concrete.” *Prevention of Thermal Cracking in Concrete at Early Ages*, *15*, pp. 51–75.

62. Xu, Q., Wang, K., Medina, C., and Engquist, B. (2015). “A Mathematical Model to Predict Adiabatic Temperatures from Isothermal Heat Evolutions with Validation for Cementitious Materials.” *International Journal of Heat and Mass Transfer*, *89*, pp. 333–338.

63. Bogue, R.H. (1955). *The Chemistry of Portland Cement*. LWW.

64. Huang, L. and Yan, P. (2019). "Effect of Alkali Content in Cement on its Hydration Kinetics and Mechanical Properties." *Construction and Building Materials*, *228*, 116833.

65. Quennoz, A. and Scrivener, K.L. (2013). "Interactions Between Alite and C3A-Gypsum Hydrations in Model Cements." *Cement and Concrete Research*, *44*, pp. 46–54.

66. Langan, B.W., Weng, K., and Ward, M.A. (2002). "Effect of Silica Fume and Fly Ash on Heat of Hydration of Portland Cement." *Cement and Concrete Research*, *32*, pp. 1045–1051.

67. Schindler, A.K. and Folliard, K.J. (2005). "Heat of Hydration Models for Cementitious Materials." *ACI Materials Journal*, *102*, p. 24.

68. Kolani, B., Buffo-Lacarrière, L., Sellier, A., et al. (2012). "Hydration of Slag-blended Cements." *Cement and Concrete Composites*, *34*, pp. 1009–1018.

69. Wang, D., Shi, C., Farzadnia, N., et al. (2018). "A Review on Use of Limestone Powder in Cement-based Materials: Mechanism, Hydration and Microstructures." *Construction and Building Materials*, *181*, pp. 659–672.

70. Costoya Fernández, M.M. (2008). *Effect of Particle Size on the Hydration Kinetics and Microstructural Development of Tricalcium Silicate*. EPFL.

71. Kada-Benameur, H., Wirquin, E., and Duthoit, B. (2000). "Determination of Apparent Activation Energy of Concrete by Isothermal Calorimetry." *Cement and Concrete Research*, *30*, pp. 301–305.

72. Carino, N.J. (1984). "The Maturity Method: Theory and Application." *Cement, Concrete and Aggregates*, *6*, pp. 61–73.

73. Poole, J.L., Riding, K.A., Folliard, K.J., et al. (2007). "Methods for Calculating Activation Energy for Portland Cement." *ACI Materials Journal*, *104*, pp. 303–311.

74. Riding, K.A., Poole, J.L., Folliard, K.J., et al. (2011). "New Model for Estimating Apparent Activation Energy of Cementitious Systems." *ACI Materials Journal*, *108*.

75. Allison, P.D. (2001). *Missing Data*. Sage publications

76. Murphy, K.P. (2012). *Machine Learning: A Probabilistic Perspective*. MIT Press.

77. Duvenaud, D. (2014). *Automatic Model Construction with Gaussian Processes*. Ph.D. thesis, University of Cambridge.

78. *The 'K' in K-fold Cross Validation*. https://arpi.unipi.it/handle/11568/962587, accessed December 6, 2021.

79. Chalupka, K., Williams, C.K.I., and Murray, I. (2013). "A Framework for Evaluating Approximation Methods for Gaussian Process Regression." *Journal of Machine Learning Research*, *14*, pp. 333–350.

80. De Bin, R., Janitza, S., Sauerbrei, W., and Boulesteix, A-L. (2016). "Subsampling Versus Bootstrapping in Resampling-based Model Selection for Multivariable Regression." *Biometrics* *72*, pp. 272–280. Available online: https://doi.org/10.1111/biom.12381.

81. Riding, K.A., Poole, J.L., Folliard, K.J., et al. (2012). "Modeling Hydration of Cementitious Systems." *ACI Materials Journal*, *109*, pp. 225–234.

82. Malisch, W.R. (1997). "Comparing the Options for Cooling Concrete."

83. U.S. Inflation Calculator (2021). Electricity Prices by Year and Adjusted for Inflation. https://www.usinflationcalculator.com/inflation/electricity-prices- adjusted-for-inflation/, accessed January 1, 2022.

84. U.S. Department of Energy (n.d.) Energy Cost Calculator for Commercial Ice Machines. https://www.energy.gov/eere/femp/energy-cost-calculator-commercial-ice-machines#output, accessed January 2, 2022.

85. PexSupply (n.d.). GPM Chart for Copper & PEX Pipe. http://s3.supplyhouse.com/product_category_files/11448-Flow-Rate-Chart.pdf, accessed January 2, 2022.